Simulation of Continuous-Wave Solid-State Laser Resonators using Field Tracing and a Fully Vectorial Fox-Li Algorithm

Dissertation
zur Erlangung des akademischen Grades
doctor rerum naturalium (Dr. rer. nat.)

vorgelegt dem Rat der Physikalisch-Astronomischen Fakultät
der Friedrich-Schiller-Universität Jena

von M. Sc. Daniel Christian Asoubar
geboren am 31. Oktober 1987 in Ochsenfurt

Gutachter

1. Prof. Dr. Frank Wyrowski, Friedrich-Schiller Universität Jena
2. PD Dr. Uwe Detlef Zeitner, Friedrich-Schiller Universität Jena
3. Prof. Dr. Horst Weber, TU Berlin

Tag der Disputation: 21. April 2016

Contents

Chapter 1

Introduction

In recent decades lasers have become the fundamental light source for a lot of applications like laser material processing, communications, metrology, medicine, security and holography [1–3], due to the unique properties of laser beams in terms of high degree of directionality, monochromaticity, coherence and brightness [4]. Nowadays, dependent on the application and the operation wavelength, different laser types are commercially available. Typically these laser types can be classified by the type of the active laser medium used [5]. One common type of active media are doped, bulk, solid-state crystals or glasses. Important applications of solid-state lasers, like laser material processing, require a laser beam with high beam-quality, customized polarization and high power, which can be obtained by the proper choice of active medium, pump and laser resonator setup [6]. Consequently there is a huge number of degrees of freedom for the design of solid-state lasers. For the development of high quality solid-state lasers one has to know the influence of these degrees of freedom on the output performance of the laser. Thus a computer-aided model of the resonator is the basis of a time- and cost-efficient tool for the analysis, tolerancing and optimization of solid-state laser resonators.

However in reality laser resonators are extremely complex multiphysical systems where in practice not all physical quantities are accessible or can be implemented in a efficient and fast resonator model. Consequently a simplified physical model is required which should include the most essential parameters for the resonator performance. For different laser types, different physical effects have varying importance on the laser performance. Thus dependent on the laser type a different physical model might be necessary. In this work a flexible and numerically efficient tool for the analysis of the transversal mode of continuous-wave (cw), solid-state laser resonators oscillating in single-transversal-mode operation is given. It is based on the generalization of the scalar Fox-Li algorithm [7, 8] to a fully vectorial field tracing concept. Therefore we reformulate Fox and Li's scalar integral equation to an eigenvalue problem consisting of a set of operator equations. This allows the flexible combination of different modeling techniques in different subdomains of the resonator. It is shown that, in principle, any modeling technique which can be formulated to operate for electromagnetic fields can be added to this field tracing concept. As an example two novel, numerically efficient simulation concepts for light propagation in laser crystals with natural-birefringence and stress-induced birefringence respectively are introduced. Furthermore two polynomial-type vector extrapolation methods are applied for the numerically efficient solution of the coupled eigenvalue problem.

The model discussed in this work gives detailed insight into the shape, polarization state and beam power of the transversal mode of cw, solid-state laser resonators. It should help optical engineers further improve their high quality lasers. For the accurate modeling of these lasers the model includes the following most dominant physical effects:

- Light diffraction, refraction and reflection
- Thermal lensing
- Birefringence
- Light amplification and gain saturation
- Polarization cross-talk and rotation.

To provide optical engineers using this tool with a sufficient amount of design freedoms, in this thesis special emphasis was placed on the inclusion of an enormous variety of different intracavity components, like

- Lenses and mirrors
- Active solid-state media
- Brewster plates
- Birefringent crystals
- Inhomogeneous media.

Furthermore the resonators can be either stable or unstable linear cavities or ring resonators. Please note that although the thesis is restricted to cw laser operation, the tools introduced might be also extended to Q-switched lasers. The simulation of mode-locked or fiber lasers is beyond the scope of this thesis. All given concepts might be also the basis for the analysis of other laser classes like gas lasers. However for other classes additional physical effects, which dominate the lasing process, must be added. For gas lasers, e.g. the simulation of gas flow can be included by the techniques given in [9, 10].

This work is structured in the following way: In chapter 2 the state-of-the art techniques for the simulation of lasers are reviewed. Here especially it is distinguished between single-pass simulation approaches, which calculate light propagation through the resonator just once, and multiple-round trip approaches which calculate the formation of the transversal resonator mode due to multiple reflections of light at the resonator mirrors. Special emphasis is placed on the concept of field tracing as a single pass approach in section 2.2 and on the scalar Fox-Li algorithm in section 2.3 as a multiple-round trip approach. It is shown that both concepts are limited in their ability to simulate laser resonators in an accurate, flexible and fast manner. For the calculation of the laser power, the important concept of rate equations is reviewed in section 2.4. In chapter 3 the limitations of field tracing as a single-pass simulation approach are overcome. It is shown that the extension of field tracing to a multiple-round trip approach can be interpreted as a generalization of the scalar Fox-Li algorithm to a fully vectorial technique. Furthermore the general mathematical structure and physical interpretation of different round trip operators are discussed, ending up with two coupled or uncoupled equations which can be interpreted as an eigenvalue problem. In the following, this eigenvalue problem is solved by a simple power method as well as by the numerically more efficient vector extrapolation methods, namely the minimal polynomial extrapolation (MPE) and the reduced rank extrapolation (RRE). To include the important physical effects of natural- or stress-induced birefringence, thermal lensing and nonlinear gain saturation two fully vectorial field tracing operators are introduced in chapter 4. Finally in chapter 5 several numerical examples are given and compared to experimental measurements from literature. Partial results given in this thesis have been already published by the author in the peer-reviewed journals and conference proceedings mentioned at the end of this document.

Chapter 2

Fundamentals of Laser Simulation

The mayor contribution of this thesis is the generalization of the Fox-Li algorithm in a way that any simulation technique which can be formulated to propagate electromagnetic fields can be included in the analysis of laser resonators. Of course this also includes the simulation techniques which are already given in literature. Therefore in this chapter the most important state-of-the-art simulation approaches for laser resonators are given to bring the novel concepts given in the following chapters into a proper context. The concepts of field tracing and the Fox-Li algorithm are also discussed in detail in this chapter. Both approaches will be generalized and combined in this thesis. Please note that due to the abundance of literature and simulation techniques only the most common approaches are discussed. Nevertheless, as shown in the following chapters, in principle any other simulation technique which can be formulated to operate on an electromagnetic field description can also be included into the concept of the generalized Fox-Li algorithm. In this work the discussion is mainly restricted to simulation techniques which are based on classical Maxwell's equations. Only in section 2.4 a simple particle model based on the rate equations is reviewed. Simulation approaches based on a more advanced particle or quantized-field description of light, as they can be found e.g. in [11–14], are beyond the scope of this work.

2.1 State-of-the-Art Techniques

In this section the fully vectorial Fox-Li algorithm is classified with respect to common state-of-the-art simulation approaches in terms of simulation accuracy, numerical effort and flexibility. Here flexibility is understood as the ability of the approaches to model different laser resonator setups containing various intracavity components. The given classification should be understood as a rule of thumb.

In principle the simulation approaches given in the literature for the analysis of single-transversal-mode, solid-state laser resonators can be divided in single-pass and multiple-round trip techniques. The former, which are mainly used in the context of laser rod analysis [15–18], simulate a single pass of the light through the resonator. Therefore a transversal light distribution must be given in front of the outcoupling mirror as an initial condition. Its shape should be close to the desired transversal laser resonator mode. This initial light distribution is propagated along a single loop in the resonator resulting in a disturbed light distribution in front of the outcoupling mirror. Thus single-pass approaches are formulated as input-output problems, meaning that for a given input field, an output field can be calculated. The resonator geometry, the pump light distribution and all other degrees of design freedom now can be optimized by minimizing the deviation between the initial and the disturbed light distribution [19–22]. For the propagation of the light along the single resonator loop, several simulation approaches based on geometrical [23–27] or physical optics are available in literature. Techniques based on geometrical optics typically provide a first insight into the laser system. The fundamental idea of these techniques is the representation of light by a set of Jones vectors which are traced through the optical system by rays, enabling a low computational effort. This rather low computational complexity was also the reason why geometrical optics approaches were most suitable for practical laser resonator design in the 70's, 80's and 90's of the past century. A detailed discussion of these design concepts is given in [28, 29]. The drawbacks of these techniques were the moderate simulation accuracies, which were mainly limited by the constraints of Jones vectors to polarization components in x and y direction as well as the neglection of diffraction effects. These limitations were overcome by the continuous progress in computer technology, enabling the application of more demanding physical optics [30] approaches where the light is represented by an electromagnetic field including the three electric as well as the three magnetic field components. Techniques based on physical optics can be divided in rigorous Maxwell solvers and approximative solutions of Maxwell's equations. The former are based on a direct discretization of the wave equation or Maxwell's equations. As illustrated in Table 2.1 these techniques, like Finite Element Methods (FEM) [31–33], Finite Difference Time Domain (FDTD) [34–38] or Fourier Modal Method (FMM) [39–42], provide in principle a high simulation accuracy. However these techniques are in practice limited in their application to micro optical components, due to their high numerical effort. Table 2.1 also shows approximative solutions of Maxwell's equations, like those given by Feit et al. [43–47] and Collins et al. [48–50]. They are typically restricted in the scope of their applications to specific optical components and physical effects, due to their approximative character and limited accuracy. One of the most flexible single-pass simulation technique is field tracing [51, 52]. It combines geometrical optics techniques with approximative and rigorous simulation approaches from physical optics. Due to the importance of field tracing for the following chapters of this thesis, the fundamentals of field tracing will be reviewed in section 2.2. A disadvantage of all these single-pass techniques is the fact that the actual transversal resonator mode, which is building up in the cavity, has to be known in advance e.g. by an educated guess or measurement [53, 54]. Due to the restriction to a single-pass propagation, the transversal mode structure of the resonator cannot be calculated.

However in several situations the exact calculation of the transversal resonator mode is necessary, e.g. for the analysis of the beam quality, polarization state or power of the laser beam emitted by the laser resonator. In these cases multiple-round trip techniques are required. In literature five classes of multiple-round trip techniques are discussed: rigorous Maxwell solvers, mode expansion methods, Gaussian mode theory, geometrical optics based approaches and the Fox-Li algorithm. Besides the Fox-Li algorithm all of these multiple-round trip techniques have their origin in a single pass analogue. To obtain multiple-round trip techniques it is only necessary to add periodic boundary conditions to the single pass techniques. Thus multiple-round trip approaches are not formulated as classical input-output problems, but as eigenvalue problems.

As shown in Table 2.1 again the rigorous Maxwell solvers are the most accurate techniques. In principle these techniques are based on the same strategies for the exact numerical solution of Maxwell's equations or the wave equation as in the case of the single-pass Maxwell solvers. In comparison only periodic boundary conditions have to be chosen. Further information about multi-pass Maxwell solvers and their concrete implementation can be found in [55–60] and references therein. However also multiple-round trip Maxwell solvers suffer from high numerical effort, which scales with the resonator volume. Therefore these rigorous techniques have a very restricted practical computational volume of the resonator cavities.

Other very accurate methods are based on the combination of the mode expansion [61–67] of the electromagnetic field inside the laser cavity with coupled mode or pertubation theory. These techniques are numerically suitable as long as the cavity geometry or intracavity components do not cause a strong coupling between the expanded modes. Dependening on the mode expansion applied, this is typically the case for radially symmetric cavities where just planar intracavity components are used (e.g. thin-film stacks) or for transversally periodic cavity structures (e.g. photonic-crystal structures). Consequently these techniques might be very suitable for microscopic vertical-cavity surface-emitting lasers (VCSEL). However for realistic macroscopic solid-state laser resonators with plenty of different intracavity components these techniques suffer from a high numerical effort due to the appearance of strong mode coupling.

The high numerical effort of Maxwell solvers and techniques based on mode expansion is probably also the reason why in the past for the simulation of most of the macroscopic solid-state laser resonators Gaussian mode based approaches [68–74] were used. These methods are rather numerically efficient and easy to implement. However as summarized in Table 2.1 these techniques are restricted in its applicability to special resonator setups with transversal modes having a fundamental or higher order Gaussian shape. These Gaussian mode shapes can be just found in a limited number of real resonators setups [71, 75, 76]. For the calculation of the laser beam power the techniques based on Gaussian modes are combined with a semi-classical separation approach [4, 77–80], meaning that the laser beam power is separately calculated from the transversal mode structure by rate equations and an integration of the photon density over the resonator volume. Advantage of this separation approach is that it can be extended to the simulation of multi-mode lasers [81]. Nevertheless the separation results in approximations which are not fulfilled in all laser resonators, e.g. the effects on the beam profile caused by nonlinear gain saturation as well as diffraction losses caused by intracavity apertures are neglected.

Another numerically efficient multi-pass technique is given by Junghans et al. [82–85]. Here the light is modeled by a position dependent Jones vector, which is propagated around the resonator by a Jones matrix, ending up with an eigenvalue problem to be solved. Due to the system description by a Jones matrix, which only takes into account Fresnel losses and the optical path length of the polarization components in x and y direction of the light, this technique is a geometrical optics approach and thus does not include any diffraction effects, which might have significant influence on the transversal mode of realistic laser resonators.

If diffraction effects must be included in the multi-pass resonator analysis, the scalar Fox-Li algorithm [7, 8] is a suitable tool. However this scalar approach is limited to resonators including paraxial optical components and modes only. More details about this technique can be found in section 2.3.

In literature approaches can also be found where some of the above mentioned techniques are combined for solving specific resonator setups. An example of this is the inclusion of natural or stress-induced birefringence effects for which the Gaussian mode theory can be extended by a Jones matrix [82] as shown e.g. in [86]. In this case the polarization state of the beam and transversal mode structure are calculated separately and consequently still fundamental or higher order Gaussian mode shapes must be assumed.

Table 2.1 – Overview of common approaches available in literature for the analysis of cw laser resonators. Dependent on their level of approximation, several restrictions on their applicability to different resonator components, on their numerical effort, simulation accuracy, their ability to calculate the transversal mode shape and on the resonator mode representation occur. For comparison the combination of the fully vectorial Fox-Li algorithm with field tracing, which is the major topic of this thesis, is given.

Simulation approach	Light representation	Included resonator component types	Numerical effort	Simulation Accuracy	Calculates transversal mode shape
Single-pass geometrical optics [23–27]	Rays + local Jones vectors	Only refractive and reflective	Low	Low	No
Collins et al. [48–50]	Paraxial, scalar field	Paraxial lenses, mirrors, Gaussian ducts, no apertures	Low	Moderate	No
Feit et al. [43–47]	Electromagnetic field	Paraxial elements	Moderate	Moderate	No
Single-pass Maxwell solver [31–42]	Electromagnetic field	All	Very high	Very high	No
Single-pass field tracing [51, 52]	Electromagnetic field	All	Scalable (from low to very high)	Scalable (from low to very high)	No
Gaussian mode theory [4, 68–74, 77–80]	Gaussian beams (fundamental and higher order)	Components maintaining the Gaussian mode shape	Low	Moderate	Yes
Junghans et al. [82–85]	Rays + local Jones vectors	Only refractive and reflective	Moderate	Moderate	Yes
Scalar Fox-Li algorithm [7, 8]	Paraxial, scalar field	Paraxial elements	Moderate	High	Yes
Mode expansion techniques [61–67]	Electromagnetic field (decomposed in modes)	All	High	High	Yes
Multi-pass Maxwell solver [55–60]	Electromagnetic field	All	Very high	Very high	Yes
Fully vectorial Fox-Li algorithm + field tracing	Electromagnetic field	All	Scalable (from low to very high)	Scalable (from low to very high)	Yes

2.2 Field Tracing

In 2011 Wyrowski and Kuhn [51] introduced the concept of field tracing. In analogy to ray tracing, where rays are propagated through the optical systems, in field tracing an electromagnetic description of light is used. In contrast to a ray description, this fully vectorial approach has the advantage that additional important physical effects of more complex light sources like partially-coherent light emitting diodes (LEDs) or ultrashort pulses can be included in the simulation [87–96]. Besides this advanced capability in terms of light source modeling, the electromagnetic light representation has the advantage that additional information like polarization, coherence, intensity and color is transferred through the optical system. These (the electromagnetic field inherent) information can be evaluated at any position or volume in the optical system, enabling the definition of a broad variety of different merit functions. In contrast to ray tracing, the electromagnetic light description requires several calculation schemes for the propagation of light through the optical system. However these light propagation schemes have the advantage of including additional waveoptical effects, like diffraction and the Gouy phase shift [97–99], as they occur only if electromagnetic fields are propagated. Wyrowski [100] interprets the field tracing concept not only as a single simulation algorithm to propagate electromagnetic fields, but as a sum or combination of all simulation techniques which can be formulated to propagate electromagnetic fields. Consequently it is a unification of optical modeling on an electromagnetic field basis. Up to now the concept of field tracing was formulated for nonresonant optical systems only [51, 52, 100]. Consequently so far the field tracing approach can be used in the context of laser resonator analysis only as a single-pass technique. Before it is generalized to a multi-pass approach a review of the most important features of single-pass field tracing is given in this section. This review will also be used to introduce a suitable nomenclature for the following chapters.

Field tracing is based on an electromagnetic description of light which is defined by the four macroscopic Maxwell's equations in a source free medium[1] [30]:

$$\nabla \times \hat{\boldsymbol{H}}(\boldsymbol{r}, t) = \frac{\partial \hat{\boldsymbol{D}}(\boldsymbol{r}, t)}{\partial t}, \tag{2.1}$$

$$\nabla \times \hat{\boldsymbol{E}}(\boldsymbol{r}, t) = -\frac{\partial \hat{\boldsymbol{B}}(\boldsymbol{r}, t)}{\partial t}, \tag{2.2}$$

$$\nabla \cdot \hat{\boldsymbol{D}}(\boldsymbol{r}, t) = 0, \tag{2.3}$$

---

[1] Please note that in field tracing it is possible and necessary to simulate light sources. However, as shown later in this section, sources are included in field tracing by proper boundary conditions.

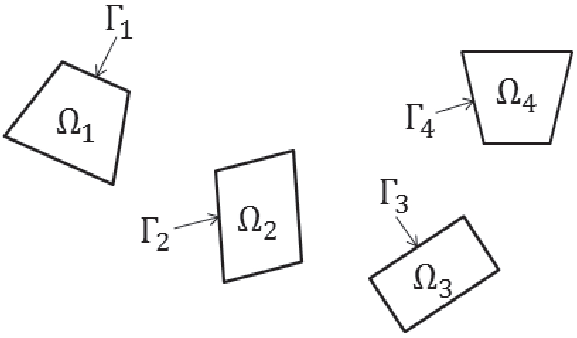

Figure 2.1 – Decomposition of an optical system in subdomains: Formally an optical system is subdivided into M subdomains Ω_m, which are embedded into a linear, isotropic, homogeneous and dispersive medium. The boundaries between the subdomains and the embedding medium are given by Γ_m [51].

$$\nabla \cdot \hat{\boldsymbol{B}}(\boldsymbol{r},t) = 0, \tag{2.4}$$

with the three electric field components $\hat{\boldsymbol{E}}(\boldsymbol{r},t) = (\hat{E}_x(\boldsymbol{r},t), \hat{E}_y(\boldsymbol{r},t), \hat{E}_z(\boldsymbol{r},t))^{\mathrm{T}}$ and the three magnetic field components $\hat{\boldsymbol{H}}(\boldsymbol{r},t) = (\hat{H}_x(\boldsymbol{r},t), \hat{H}_y(\boldsymbol{r},t), \hat{H}_z(\boldsymbol{r},t))^{\mathrm{T}}$ of the electromagnetic field. t is the time and $\boldsymbol{r} = (x,y,z)^{\mathrm{T}}$ is the three dimensional position vector with the space coordinates x, y and z. The electric flux density $\hat{\boldsymbol{D}}(\boldsymbol{r},t)$ and the magnetic flux density $\hat{\boldsymbol{B}}(\boldsymbol{r},t)$ are related to the respective electromagnetic field by [30]:

$$\hat{\boldsymbol{D}}(\boldsymbol{r},t) = \epsilon_0 \hat{\boldsymbol{E}}(\boldsymbol{r},t) + \hat{\boldsymbol{P}}(\boldsymbol{r},t) \tag{2.5}$$

with the polarization density $\hat{\boldsymbol{P}}(\boldsymbol{r},t)$, the electric permittivity ϵ_0 and by

$$\hat{\boldsymbol{B}}(\boldsymbol{r},t) = \mu_0 \hat{\boldsymbol{H}}(\boldsymbol{r},t) \tag{2.6}$$

with the magnetic permeability of vacuum μ_0 and where non-magnetic materials have been assumed. As illustrated in Fig. 2.1, formally an optical system given in $\Omega \subset \mathbb{R}^3$ can be subdivided in M subdomains Ω_m with $m = 1...M$. The boundaries of the subdomains Ω_m are denoted by Γ_m and can be chosen freely to some extent in shape and size [51]. The subdomains embed all positions of the optical system where the medium response is not isotropic, linear and homogeneous [51]. Formally this means that outside the subdomains there is

$$\hat{\boldsymbol{P}}(\boldsymbol{r},t) = \left\{ \boldsymbol{r} \notin \Omega_m : \hat{\boldsymbol{P}}(t) = \epsilon_0 \int_{-\infty}^{\infty} \chi(t-t') \hat{\boldsymbol{E}}(t') \mathrm{d}t' \right\}. \tag{2.7}$$

Here $\epsilon_0 \chi(t)$ describes the system response function of the dispersive, isotropic, linear and homogeneous medium which embeds all subdomains. Typically the subdomains are related to the components, which are positioned in the optical system. However this is not necessary for the following discussions and dependent on the exact simulation task it might be even helpful to decompose a single component in several subdomains or embed several components in a single subdomain. Consequently for specific optical setups it might be also suitable to include dispersive, isotropic, linear and homogeneous regions of the system in subdomains [51]. Plugging Eq. (2.7) and Eqs. (2.5) and (2.6) into Maxwell's equations given by Eqs. (2.1) – (2.4), leads to [30]

$$\nabla \times \boldsymbol{H}(\boldsymbol{r},\omega) = -\mathrm{i}\omega\epsilon(\omega)\boldsymbol{E}(\boldsymbol{r},\omega), \tag{2.8}$$

$$\nabla \times \boldsymbol{E}(\boldsymbol{r},\omega) = \mathrm{i}\omega\mu_0\boldsymbol{H}(\boldsymbol{r},\omega), \tag{2.9}$$

$$\nabla \cdot \boldsymbol{E}(\boldsymbol{r},\omega) = 0, \tag{2.10}$$

$$\nabla \cdot \boldsymbol{H}(\boldsymbol{r},\omega) = 0, \tag{2.11}$$

which describes the light propagation in the dispersive, isotropic, linear and homogeneous medium defined by the permittivity $\epsilon(\omega)$ and which embeds all subdomains. Here the representation of light by a complex field $\boldsymbol{V}(\boldsymbol{r},\omega)$ was used, which is defined by [30]:

$$\hat{\boldsymbol{V}}(\boldsymbol{r},t) = \mathrm{Re}\left\{\int_{-\infty}^{\infty}\boldsymbol{V}(\boldsymbol{r},\omega)\exp\left(-\mathrm{i}\omega t\right)\mathrm{d}\omega\right\}, \tag{2.12}$$

and the simplified notation of the complex electromagnetic field vector [51]

$$\boldsymbol{V} = (V_1, V_2, ..., V_\ell, ..., V_6)^{\mathrm{T}} = (E_x, E_y, E_z, H_x, H_y, H_z)^{\mathrm{T}}. \tag{2.13}$$

ω is the angular frequency. For cw lasers only harmonic or monochromatic fields - which oscillate with the single angular frequency ω_0 - are of concern [2]. Consequently the Dirac-δ function can be used to define a complex harmonic field amplitude $\boldsymbol{V}(\boldsymbol{r},\omega_0)$ by [101]:

$$\boldsymbol{V}(\boldsymbol{r},w) = \boldsymbol{V}(\boldsymbol{r},\omega_0)\delta(\omega-\omega_0), \tag{2.14}$$

which is related to the real electric field by:

$$\hat{\boldsymbol{V}}(\boldsymbol{r},t) = \mathrm{Re}\{\boldsymbol{V}(\boldsymbol{r},\omega_0)\exp\left(-\mathrm{i}\omega_0 t\right)\}. \tag{2.15}$$

---

[2] Wyrowski et al. [89–91,96] showed that field tracing is not restricted to monochromatic light, but can be extended to pulsed or polychromatic light sources. In these cases a set of harmonic fields are propagated through the optical system.

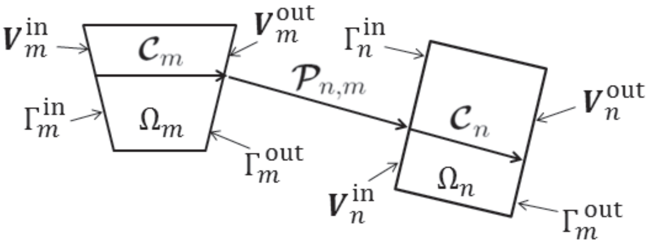

Figure 2.2 – Illustration of field tracing operator notation: the light propagation through the subdomains is described by the component operator $\boldsymbol{\mathcal{C}}_m$. The light propagation inside the linear, isotropic and homogeneous medium between the subdomains is described by the propagation operator $\boldsymbol{\mathcal{P}}_{n,m}$ [51].

Substituting Eq. (2.14) in Eqs. (2.8) – (2.11) yields the Helmholtz equation [30]:

$$\nabla^2 V_\ell(\boldsymbol{r}) + k^2 V_\ell(\boldsymbol{r}) = 0 \qquad \text{for} \qquad \ell = 1, 2, ..., 6 \tag{2.16}$$

with the wavenumber $k = \omega_0 n / c_0$, the vacuum speed of light $c_0 = 1/(\epsilon_0 \mu_0)^{1/2}$ and the refractive index n. V_ℓ represents as it was defined in Eq. (2.13) a single component of the complex amplitude vector of the harmonic field. The variable ω_0 was skipped for better readability. Eq. (2.16) describes the light propagation of a harmonic field in the surrounding isotropic, linear and homogeneous medium. Thus, as illustrated in Fig. 2.2, in field tracing Eq. (2.16) has to be solved to propagate an electromagnetic field $\boldsymbol{V}_m^{\mathrm{out}}$, which leaves the subdomain Ω_m through the boundary Γ_m^{out}, to the boundary Γ_n^{in} of the next subdomain Ω_n. Formally this propagation can be formulated as [51]:

$$\boldsymbol{V}_n^{\mathrm{in}} = \boldsymbol{\mathcal{P}}_{n,m} \boldsymbol{V}_m^{\mathrm{out}} \tag{2.17}$$

for $m \neq n$ with the field entering a subdomain

$$\boldsymbol{V}_m^{\mathrm{in}} := \boldsymbol{V}^{\mathrm{in}}(\boldsymbol{r} \in \Gamma_m^{\mathrm{in}}) \tag{2.18}$$

through the boundary Γ_m^{in} and a field leaving the subdomain

$$\boldsymbol{V}_m^{\mathrm{out}} := \boldsymbol{V}^{\mathrm{out}}(\boldsymbol{r} \in \Gamma_m^{\mathrm{out}}). \tag{2.19}$$

through the boundary Γ_m^{out}. The operator $\boldsymbol{\mathcal{P}}_{n,m}$ describes the light propagation of the six electromagnetic field components in the embedding homogeneous medium. Thus $\boldsymbol{\mathcal{P}}_{n,m}$ is called propagation operator in the following and can be any exact or approximative solution of Eq. (2.16).

Inside the subdomains Ω_m the matter response is not restricted to be linear, isotropic and homogeneous. Consequently for an electromagnetic field $\boldsymbol{V}_m^{\mathrm{in}}$ entering the subdomain Ω_m at the boundary Γ_m^{in}, in most cases it is not sufficient to solve the Helmholtz equation to calculate the field $\boldsymbol{V}_m^{\text{out}}$ leaving this particular subdomain. Instead a particular approximative or exact solution to the general Maxwell's Equations given by Eqs. (2.1) – (2.4) has to be found. Formally this solution can be written by the component operator $\boldsymbol{\mathcal{C}}_m$ [51]

$$\boldsymbol{V}_m^{\text{out}} = \boldsymbol{\mathcal{C}}_m \boldsymbol{V}_m^{\text{in}} \tag{2.20}$$

describing the light propagation of all six field components through the subdomain Ω_m. Fig. 2.2 illustrates this component operator. Using this operator notation enables the formulation of a general scattering problem, where the output field on a certain boundary depends on the output field of all other subdomains [51, 52]

$$\boldsymbol{V}_n^{\text{out}} = \boldsymbol{V}_n^{\text{Source}} + \sum_{m=1, m \neq n}^{M} \boldsymbol{\mathcal{C}}_n \boldsymbol{\mathcal{P}}_{n,m} \boldsymbol{V}_m^{\text{out}}. \tag{2.21}$$

Here $\boldsymbol{V}_n^{\text{Source}}$ is the contribution of an optional source field to the output field of subdomain Ω_n. Thus to model a light source in the system, $\boldsymbol{V}_n^{\text{Source}}$ must be non-zero for at least one subdomain. Eq. (2.21) describes a set of equations with the unknowns $\boldsymbol{V}_n^{\text{out}}$ for $n = 1, 2, ...M$. It can be written in a more compact matrix form [51, 52]

$$\left(\underline{\boldsymbol{I}} - \underline{\boldsymbol{\mathcal{C}}}\underline{\boldsymbol{\mathcal{P}}}\right) \underline{\boldsymbol{V}}^{\text{out}} = \underline{\boldsymbol{V}}^{\text{Source}} \tag{2.22}$$

where $\underline{\boldsymbol{I}}$ is the diagonal matrix with identity operators $\boldsymbol{\mathcal{I}}$. In the following Eq. (2.22) will be called general field tracing equation. Furthermore there is the diagonal matrix

$$\underline{\boldsymbol{\mathcal{C}}} = \begin{pmatrix} \boldsymbol{\mathcal{C}}_1 & 0 & \dots & 0 \\ 0 & \boldsymbol{\mathcal{C}}_2 & \ddots & \vdots \\ \vdots & \ddots & \ddots & 0 \\ 0 & \dots & 0 & \boldsymbol{\mathcal{C}}_M \end{pmatrix}, \tag{2.23}$$

the matrix

$$\underline{\boldsymbol{\mathcal{P}}} = \begin{pmatrix} 0 & \boldsymbol{\mathcal{P}}_{1,2} & \dots & \boldsymbol{\mathcal{P}}_{1,M} \\ \boldsymbol{\mathcal{P}}_{2,1} & 0 & \ddots & \vdots \\ \vdots & \ddots & \ddots & \boldsymbol{\mathcal{P}}_{M-1,M} \\ \boldsymbol{\mathcal{P}}_{M,1} & \dots & \boldsymbol{\mathcal{P}}_{M,M-1} & 0 \end{pmatrix}, \tag{2.24}$$

the vector

$$\underline{\boldsymbol{V}}^{\text{out}} = \left(\boldsymbol{V}_1^{\text{out}}, \boldsymbol{V}_2^{\text{out}}, ..., \boldsymbol{V}_M^{\text{out}}\right)^{\text{T}} \tag{2.25}$$

and the vector

$$\underline{\boldsymbol{V}}^{\text{Source}} = \left(\boldsymbol{V}_1^{\text{Source}}, \boldsymbol{V}_2^{\text{Source}}, ..., \boldsymbol{V}_M^{\text{Source}}\right)^{\text{T}}. \tag{2.26}$$

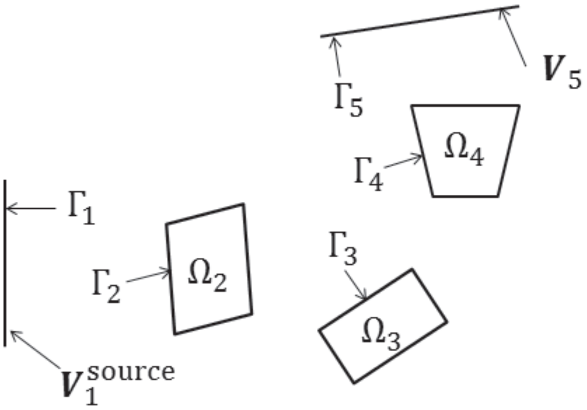

Figure 2.3 – Sequential field tracing: the electromagnetic field $\boldsymbol{V}_1^{\text{Source}}$ emitted by one light source and defined on the boundary Γ_1 is sequentially traced through the optical system consisting of the subdomains Ω_m. The resulting field $\boldsymbol{V}_5$ on the final boundary Γ_5 is of major concern [51].

In the case that

$$||\underline{\mathcal{CP}}|| < 1, \tag{2.27}$$

meaning that there is absorption of light within the optical system, the general field tracing equation given by Eq. (2.22) can be expressed by a Neumann series [51, 52, 102]:

$$\underline{\boldsymbol{V}}^{\text{out}} = \sum_{p=0}^{\infty} (\underline{\mathcal{CP}})^p \underline{\boldsymbol{V}}^{\text{Source}}. \tag{2.28}$$

If only one light source is present in the optical system there is $\boldsymbol{V}_n^{\text{Source}} \neq 0$ for $n = 1$, only. The restriction to a sequential field tracing approach - meaning that the light entering the subdomain Ω_m only depends on the light leaving the subdomain Ω_{m-1} - simplifies Eq. (2.28) to [51]

$$\boldsymbol{V}_n^{\text{out}} = \left(\prod_{m=2}^{n} \boldsymbol{\mathcal{C}}_m \boldsymbol{\mathcal{P}}_{m,m-1} \right) \boldsymbol{V}_1^{\text{Source}} \tag{2.29}$$

which is the principal field tracing equation for the sequential simulation of nonresonant optical systems. It is illustrated in Fig. 2.3. In the following an optical system is said to be nonresonant if the condition given by Eq. (2.27) is fulfilled, meaning that the light energy emitted by the source is totally absorbed in the subdomains, the embedding medium and at the boundaries of the system at infinity.

Please note that in the embedding medium it is not necessary to propagate all six field components V_ℓ separately, because only two of them can be chosen independently and the rest of them follow directly from the four Maxwell's equations given by Eqs. (2.8) – (2.11). Thus to decrease the computational effort, in the following only the V_1 and V_2 field components are propagated in the embedding medium. An important exact or rigorous propagation operator which describes the light propagation between two parallel plane interfaces

Γ_m^{out} and Γ_n^{in} separated by the distance z is the angular spectrum of plane waves (SPW) operator [103], which has the operator matrix form:

$$\boldsymbol{\mathcal{P}}_{n,m}^{\mathrm{SPW}} = \begin{pmatrix} \mathcal{P}^{\mathrm{SPW}} & 0 \\ 0 & \mathcal{P}^{\mathrm{SPW}} \end{pmatrix} \tag{2.30}$$

and is given by

$$V_\ell(\boldsymbol{\rho}, z) = \mathcal{P}^{\mathrm{SPW}} V_\ell(\boldsymbol{\rho}, 0) = \mathscr{F}^{-1} \left\{ \mathscr{F} \left[V_\ell(\boldsymbol{\rho}, 0) \right] \exp\left[\mathrm{i} k_z z \right] \right\}, \tag{2.31}$$

for $\ell = 1, 2$, with $k_z = (k^2 - k_x^2 - k_y^2)^{1/2}$ as well as with the Fourier transformation

$$\mathscr{F} \left[V_\ell(\boldsymbol{\rho}) \right] = \frac{1}{2\pi} \iint_{-\infty}^{+\infty} V_\ell(\boldsymbol{\rho}) \exp(-\mathrm{i} \boldsymbol{\kappa} \cdot \boldsymbol{\rho}) \mathrm{d}x \mathrm{d}y \tag{2.32}$$

and the inverse Fourier transformation $\mathscr{F}^{-1}$ with the conjugate variables $\boldsymbol{\rho} = (x, y)^{\mathrm{T}}$ and $\boldsymbol{\kappa} = (k_x, k_y)^{\mathrm{T}}$. The remaining four field components are calculated on demand by [51]:

$$V_3(\boldsymbol{\rho}) = -\mathscr{F}^{-1} \left[\frac{1}{k_z} \left(k_x \mathscr{F} V_1(\boldsymbol{\rho}) + k_y \mathscr{F} V_2(\boldsymbol{\rho}) \right) \right], \tag{2.33}$$

$$V_4(\boldsymbol{\rho}) = -\sqrt{\frac{\epsilon_0}{\mu_0}} \frac{1}{k_0} \mathscr{F}^{-1} \left[\frac{1}{k_z} \left(k_x k_y \mathscr{F} V_1(\boldsymbol{\rho}) + (k_y^2 + k_z^2) \mathscr{F} V_2(\boldsymbol{\rho}) \right) \right], \tag{2.34}$$

$$V_5(\boldsymbol{\rho}) = -\sqrt{\frac{\epsilon_0}{\mu_0}} \frac{1}{k_0} \mathscr{F}^{-1} \left[\frac{1}{k_z} \left((k_x^2 + k_z^2) \mathscr{F} V_1(\boldsymbol{\rho}) + k_x k_y \mathscr{F} V_2(\boldsymbol{\rho}) \right) \right], \tag{2.35}$$

$$V_6(\boldsymbol{\rho}) = \sqrt{\frac{\epsilon_0}{\mu_0}} \frac{1}{k_0} \mathscr{F}^{-1} \left[\left(k_x \mathscr{F} V_2(\boldsymbol{\rho}) - k_y \mathscr{F} V_1(\boldsymbol{\rho}) \right) \right], \tag{2.36}$$

with the wavenumber in vacuum k_0. This calculation of the remaining field components might be necessary, e.g. for the light propagation $\boldsymbol{\mathcal{C}}_m$ through a subdomain Ω_m with anisotropic or nonlinear matter response. Three operators which require more than two field components are given in chapter 4. A series of other important $\boldsymbol{\mathcal{C}}_m$ and $\boldsymbol{\mathcal{P}}_{n,m}$ operators are given in the following chapters.

So far it has been shown how the principal field tracing equation for sequential simulation of nonresonant optical systems given by Eq. (2.29) can be derived. In principle it is also possible to define, on the basis of a Neumann series, a nonsequential technique for nonresonant optical systems [52]. Nevertheless up to now the condition given by Eq. (2.27) must always be satisfied, which is only the case for optical systems where absorption processes inside the subdomains, in the embedding medium or at the system boundaries (infinity) damp the light. However for a steady-state operation of a laser resonator, all resonator losses have to be balanced by the active medium, meaning that the resonance condition $||\underline{\mathcal{CP}}|| = 1$ must hold. This condition — which is also called lasing threshold [5, 71] — violates the necessary condition for the formulation of the Neumann series given in Eq. (2.28). Thus so far the concept of field tracing is limited to nonresonant optical systems. This limitation to nonresonant optical systems is the reason why up to now field tracing can be only applied as a single-pass technique for laser resonator analysis. In chapter 3 the general field tracing equation given by Eq. (2.22) will be reformulated for the simulation of resonant optical systems, ending up with a the multi-pass simulation approach. It turns out that this reformulation is a fully vectorial generalization of the scalar Fox-Li algorithm.

2.3 Scalar Fox-Li Algorithm

In the 1960's Fox and Li [7, 8] showed that inside a laser resonator one or more possible scalar field distributions exist which reproduce themselves after propagating a single time through the complete cavity. Thus as shown in Fig. 2.4 a scalar field $U^{\mathrm{Left}}(x', y', z_0)$ defined in a transversal plane at the axial position z_0 in front of the outcoupling resonator mirror M_1 can be propagated to the mirror M_2 at the other end of the resonator by

$$U^{\mathrm{Right},+}(x, y, z_1) = \iint K^+(x, y, x', y') U^{\mathrm{Left},+}(x', y', z_0) \mathrm{d}x' \mathrm{d}y' \tag{2.37}$$

where $U(x, y, z_0)$ is the complex amplitude of the harmonic scalar field $\hat{U}(x, y, z_0, t)$, defined by [101]

$$\hat{U}(x, y, z_0, t) = \mathrm{Re}\{U(x, y, z_0) \exp(-\mathrm{i}\omega_0 t)\}, \tag{2.38}$$

which oscillates with angular frequency ω_0 in time t. In Eq. (2.37) the "+" superscript above the field U indicates that the field points in the positive z-direction. The integral kernel $K^+(x, y, x', y')$ describes the propagation of the complex amplitude of the scalar field in forward direction through the entire resonator, which might include several intracavity components embedded in a homogeneous medium. Furthermore the light propagating in backward direction from M_2 to M_1 can be calculated by

$$U^{\mathrm{Left},-}(x, y, z_0) = \iint K^-(x, y, x', y') U^{\mathrm{Right},-}(x', y', z_1) \mathrm{d}x' \mathrm{d}y' \tag{2.39}$$

using the integral kernel $K^-(x, y, x', y')$, which describes the propagation of the complex amplitude of the scalar field in backward direction and the superscript "$-$" above the field U, indicating its propagation in the $-z$-direction. At the mirrors, the forward and backward propagating fields are connected by:

$$U^{\mathrm{Left/Right},+} = r^{M_1/M_2} U^{\mathrm{Left/Right},-} \tag{2.40}$$

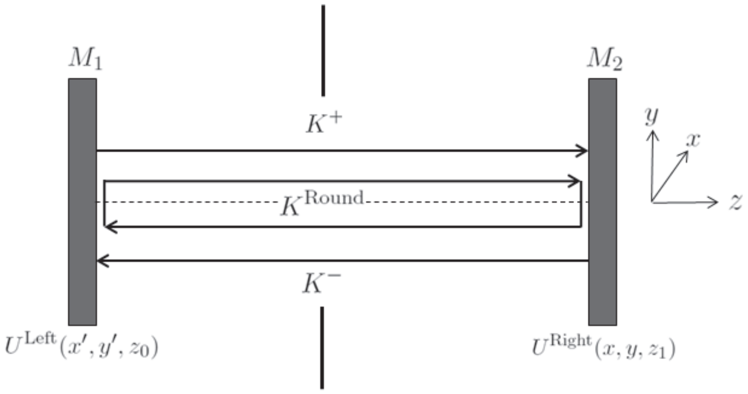

Figure 2.4 – Round trip operator concept for scalar Fox-Li algorithm: A scalar, paraxial field $U^{\mathrm{Left}}(x', y', z_0)$ given in front of the mirror M_1 can be propagated through the resonator, which contains thin optical elements (e.g. a thin aperture), by the integral kernel $K^+(x, y, x', y')$, ending up with the field $U^{\mathrm{Right}}(x, y, z_1)$ in front of the mirror M_2. The inverse propagation can be described by the integral kernel $K^-(x, y, x', y')$. The combination of forward and backward propagation leads to the round trip propagation kernel $K^{\mathrm{Round}}(x, y, x', y')$, describing the light propagation starting and ending in front of mirror M_1.

where r^{M_1/M_2} describes the reflection either at mirror M_1 or at mirror M_2. Substituting Eqs. (2.37) and (2.40) in Eq. (2.39) leads to [7,8]

$$U^{\mathrm{Left},+}(x, y, z_0) = \iint K^{\mathrm{Round}}(x, y, x', y') U^{\mathrm{Left},+}(x', y', z_0) \mathrm{d}x' \mathrm{d}y' \tag{2.41}$$

where the integral kernel K^{Round} describes — as shown in Fig. 2.4 — the propagation of the complex amplitude of the scalar field along the entire laser resonator round trip. Thus it does not only contain the forward and backward propagation kernels K^+ and K^- but also the reflection r^{M_1/M_2} at the resonator mirrors M_1 and M_2. Scalar field distributions which fulfill Eq. (2.41) exactly reproduce themselves after propagating a single time through the complete cavity. Strictly speaking this can only be the case if the resonator is loss-less or if — more realistically — it contains an active medium which compensates the resonator losses. Furthermore the angular frequency ω_0 of the harmonic field must exactly match an axial resonator mode. Nevertheless if lossy laser resonators should be simulated in a first approximation without considering the active medium or axial modes, only the transversal shape, but neither the field power nor the absolute phase, should reproduce itself after one round trip. According to Fox and Li [7,8] this kind of field distributions are called transversal eigenmodes of the laser resonator and can be calculated by solving the eigenvalue problem

$$\gamma U(x, y, z) = \iint K^{\mathrm{Round}}(x, y, x', y') U(x', y', z) \mathrm{d}x' \mathrm{d}y'. \tag{2.42}$$

Please note that Eq. (2.42) is a slightly modified version of Eq. (2.41). The first difference is that the term $U^{\text{Left},+}(x,y,z_0)$ is replaced by $U(x,y,z)$, to emphasize that the eigenmode must reproduce itself not only at the resonator mirrors but at an arbitrary plane in both propagation directions. Of course this is also true for Eq. (2.41). The second difference is the appearance of the complex eigenvalue γ, which is connected to the laser resonator round trip losses by [7,8]:

$$\text{Resonator Round Trip Losses} = 1 - |\gamma|^2. \tag{2.43}$$

For cw laser resonator simulations including an active medium which balances the laser resonator losses, the round trip losses are simply 0 and thus $\gamma = 1$ [3] so that Eq. (2.42) ends up with the form of Eq. (2.41).

Depending on the shape of the resonator mirrors and the applied intracavity components, the propagation kernel $K^{\text{Round}}(x,y,x',y')$ has to be formulated. As derived in appendix A in principle $K^{\text{Round}}(x,y,x',y')$ is limited to solutions of the scalar, inhomogeneous wave equation

$$\nabla^2 U(\boldsymbol{r},\omega_0) + \frac{\omega_0^2}{c_0^2}\epsilon_r(\boldsymbol{r},\omega_0)U(\boldsymbol{r},\omega_0) = 0 \tag{2.44}$$

due to the restriction of Eq. (2.42) to scalar fields. Thus as shown in appendix A only paraxial transversal modes of resonators consisting of linear, isotropic and thin elements can be calculated by the scalar Fox-Li algorithm. In their initial work Fox and Li [7] used Kirchhoff's diffraction formula

$$K(x,y,x',y') = \frac{\mathrm{i}}{\lambda r}\exp(\mathrm{i}kr)(1+\cos\phi) \tag{2.45}$$

as a special solution of Eq. (2.44) to calculate the field propagation through a strip resonator. A drawback of the solution given by Eq. (2.45) is its high computational effort and its limitation to strip resonators only. To emphasize that any simulation technique which solves the approximated Eq. (2.44) can be used to describe the resonator round trip, the eigenvalue problem of Eq. (2.42) is reformulated in an operator notation [104]

$$\gamma U(x,y,z) = \mathcal{R}U(x,y,z) \tag{2.46}$$

where $\mathcal{R}$ is the scalar round trip propagation operator. In the following, Eq. (2.46) is referred to as the scalar Fox-Li algorithm. Nevertheless also Eq. (2.46) is restricted to paraxial fields and resonators consisting of isotropic, linear and thin elements, due to the restriction of Eq. (2.44). Furthermore please note that Eq. (2.46) is restricted to laser

---

[3] Please note that strictly speaking the balancing of the resonator losses by the active medium only leads to $|\gamma| = 1$. Thus there might be an additional phase shift $\arg(\gamma)$ left, which is introduced at each round trip. This additional phase shift only appears if the angular frequency ω_0 of the harmonic field does not exactly match an axial resonator mode.

resonators oscillating in single-transversal-mode operation due to the neglection of mode competition within the active medium [105]. In principle this mode competition can be included in the scalar simulation by an extension of Eq. (2.46). Further details about this extension can be found in [106, 107].

2.4 Description of Light Amplification by Rate Equations

In the previous sections the propagation of electromagnetic fields by Maxwell's equations was discussed. However for a realistic simulation of lasers, the process of light amplification must be considered, too. Therefore a semi-classical approach is used, meaning that the rate equations [4, 71] are applied to describe the energy kinetics of the laser, whereas the light propagation inside the laser cavity is still governed by the classical Maxwell's equations. In the following, stationary solutions of the rate equations for three- and four-level laser systems are given. This time invariance is assumed to be valid for cw-laser emission. Furthermore the connection between a plane wave — which is a special solution of Maxwell's equations — and the rate equations by means of Lambert-Beer's law is reviewed. In section 4.2 it will be shown that this connection is also the basis for the description of light amplification of harmonic non-plane wave fields in active media.

In the classical model of laser kinetics there are four different processes for energy transitions between different possible atom energy levels $\mathscr{E}_i$ [71]. Normally each of these processes has an influence on the temporal evolution of the energy level population. Fig. 2.5 shows the four processes and their contribution to the energy level population on a simple two level system with population densities N_1 and N_2 of the corresponding energy levels $\mathscr{E}_1$ and $\mathscr{E}_2$ [4]. Here in principle there are non-radiative and radiative transitions. Furthermore the radiative transitions can be classified into stimulated and spontaneous (or statistical) processes. Stimulated radiative transition processes depend on the cross-section σ_{ij} and the photon flux [4]

$$F_{ij} = \frac{I_{ij}}{h\nu_{ij}} \tag{2.47}$$

with Planck's constant h and the light intensity I_{ij} with the light frequency ν_{ij}. Spontaneous radiative as well as non-radiative processes normally are modeled by (statistically weighted) transition rates γ_{ij} with $\mathscr{E}_i$ being the initial and $\mathscr{E}_j$ being the target energy level of the energy transition. In a real laser material energy transitions are taking place between more than two energy levels [71]. Normally three- or four-level systems are considered in literature [4, 71]. Fig. 2.6 shows all relevant transitions in a four-level pumping scheme. Please note that here all radiative and non-radiative spontaneous energy transitions, which

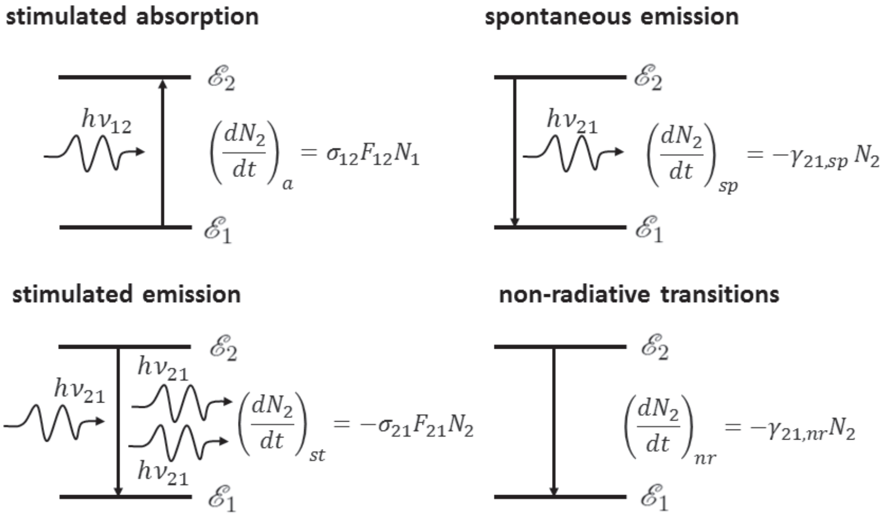

Figure 2.5 – Different energy transitions in laser materials and their contribution to the rate equations [4].

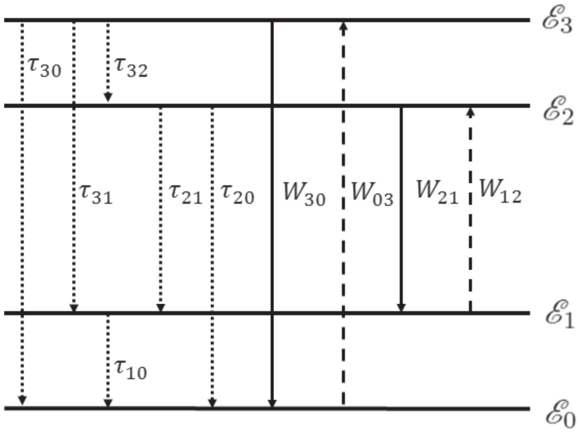

Figure 2.6 – Relevant transitions of 4-level laser system: solid lines show energy transition due to stimulated emission, the dashed lines show photon absorption or non-optical pumping, and the dotted lines show non-radiative relaxation processes [108].

are given by the decay rates $\gamma_{ij,\mathrm{sp}}$ and $\gamma_{ij,\mathrm{nr}}$, are pooled by the averaged lifetime [71]

$$\tau_{ij} = \frac{1}{\gamma_{ij,\mathrm{nr}} + \gamma_{ij,\mathrm{sp}}} \tag{2.48}$$

and represented by dotted lines in Fig. 2.6. Stimulated radiative transitions are characterized by the transition probability W_{ij}, which for the optical stimulation is given by [71]

$$W_{ij} = f_i \sigma_{ij} F_{ij} \tag{2.49}$$

with the material-specific cross-section σ_{ij}, the fractional population f_i and the photon flux F_{ij} defined according to Eq. (2.47). Furthermore it is assumed that the energy levels are separated enough to avoid non-radiative energy transfer from a lower to an upper energy level [71]. In real active media there are further spontaneous radiative and non-radiative transitions from the four shown energy levels to other energy states [71]. However normally all of these transitions end up in the ground state $\mathscr{E}_0$ and are of no relevance for further discussion besides replacing the averaged lifetimes for transitions to the ground state τ_{i0} by an effective averaged lifetime τ'_{i0}, which can be determined by fluorescence lifetime measurements [71, 109, 110].

For the four-level laser diagram in Fig. 2.6 the rate equations, which describe the change in state population, can be written as [4, 108]:

$$\frac{\mathrm{d}N_3}{\mathrm{d}t} = -\frac{N_3}{\tau'_{30}} - \frac{N_3}{\tau_{31}} - \frac{N_3}{\tau_{32}} + W_{03}N_0 - W_{30}N_3 \ , \tag{2.50}$$

$$\frac{\mathrm{d}N_2}{\mathrm{d}t} = \frac{N_3}{\tau_{32}} - \frac{N_2}{\tau'_{20}} - \frac{N_2}{\tau_{21}} + W_{12}N_1 - W_{21}N_2 \ , \tag{2.51}$$

$$\frac{\mathrm{d}N_1}{\mathrm{d}t} = \frac{N_3}{\tau_{31}} + \frac{N_2}{\tau_{21}} - \frac{N_1}{\tau'_{10}} - W_{12}N_1 + W_{21}N_2 \ , \tag{2.52}$$

$$\frac{\mathrm{d}N_0}{\mathrm{d}t} = \frac{N_3}{\tau'_{30}} + \frac{N_2}{\tau'_{20}} + \frac{N_1}{\tau'_{10}} - W_{03}N_0 + W_{30}N_3 \ . \tag{2.53}$$

Furthermore a fifth equation is obtained, if the invariance of density of doped ions N is assumed:

$$N = N_0 + N_1 + N_2 + N_3 \ . \tag{2.54}$$

In the following the definition of the pump quantum efficiency [5]

$$\frac{1}{\eta_\mathrm{p}} = 1 + \frac{\tau_{32}}{\tau_{31}} + \frac{\tau_{32}}{\tau'_{30}} \ , \tag{2.55}$$

is used with the emission lifetime [108]

$$\frac{1}{\tau_\mathrm{em}} = \frac{1}{\tau_{21}} + \frac{1}{\tau'_{20}} \ , \tag{2.56}$$

the saturation intensity for absorption [108]

$$I_\mathrm{s}^\mathrm{p} = \frac{h\nu_p}{f_0\sigma_{03}\tau_\mathrm{em}} \ , \tag{2.57}$$

and the saturation intensity for emission [108]

$$I_\mathrm{s}^\mathrm{L} = \frac{h\nu_L}{f_2\sigma_{21}\tau_\mathrm{em}} \ , \tag{2.58}$$

where optical pumping and emission is given according to Eq. (2.49) and the definitions of the pump light frequency $\nu_p = \nu_{03}$ and the laser light frequency $\nu_L = \nu_{21}$.

According to Sato and Taira [108], the steady state condition

$$\frac{\mathrm{d}N_3}{\mathrm{d}t} = \frac{\mathrm{d}N_2}{\mathrm{d}t} = \frac{\mathrm{d}N_1}{\mathrm{d}t} = \frac{\mathrm{d}N_0}{\mathrm{d}t} = 0 \ , \tag{2.59}$$

can be used to obtain the stationary solution of Eqs. (2.50) – (2.54) in the form

$$N_3 \approx 0 \ , \tag{2.60}$$

$$N_2 \approx \frac{\eta_\mathrm{p} \frac{I_\mathrm{p}}{I_\mathrm{s}^\mathrm{P}}}{1 + \frac{I_\mathrm{L}}{I_\mathrm{s}^\mathrm{L}} + \eta_\mathrm{p} \frac{I_\mathrm{p}}{I_\mathrm{s}^\mathrm{P}}} N \ , \tag{2.61}$$

$$N_1 \approx 0 \ , \tag{2.62}$$

$$N_0 \approx \frac{1 + \frac{I_\mathrm{L}}{I_\mathrm{s}^\mathrm{L}}}{1 + \frac{I_\mathrm{L}}{I_\mathrm{s}^\mathrm{L}} + \eta_\mathrm{p} \frac{I_\mathrm{p}}{I_\mathrm{s}^\mathrm{P}}} N \ , \tag{2.63}$$

where the assumptions

$$\frac{\tau_{10}'}{\tau_\mathrm{em}} \approx 0 \ , \tag{2.64}$$

$$\frac{\tau_{3i}}{\tau_{2i}} \approx 0 \ , \tag{2.65}$$

and

$$\eta_\mathrm{p} < 1 \ , \tag{2.66}$$

have been used, which are realistic for useful laser materials [108]. Furthermore there is

$$f_0 = f_1 = f_2 = f_3 = 1 \ , \tag{2.67}$$

due to non-degenerated energy-levels in Fig. 2.6.

The field amplification inside a uniformly pumped, solid-state laser medium for monochromatic plane wave illumination is described by Lambert-Beer's law [71]

$$\frac{\mathrm{d}I}{\mathrm{d}z} = gI \tag{2.68}$$

with the gain coefficient g and the light intensity defined by the time-averaged Poynting vector $\langle \boldsymbol{S} \rangle$, which is given for plane waves by [111]

$$I \equiv |\langle \boldsymbol{S} \rangle| = n \frac{\epsilon_0}{2} c \left(|V_{1,\mathrm{plane}}|^2 + |V_{2,\mathrm{plane}}|^2 \right) \ . \tag{2.69}$$

Here again c is the vacuum speed of light, n is the real part of the refractive index, $V_{1,\text{plane}}$ and $V_{2,\text{plane}}$ are the complex amplitudes of the E_x and E_y polarization components of the plane wave and ϵ_0 is the vacuum permittivity. The plane wave propagation inside the homogeneous solid-state laser medium must be a solution of Eq. (2.68) as well as solution of the Helmholtz equation given by Eq. (2.16). Thus the propagation of a plane wave along the optical axis, which points in the $+z$-direction, can be described by

$$V_{\ell,\text{plane}}(z) = V_{\ell,\text{plane}}(0) \exp\left(\mathrm{i}k_0 n z + 0.5 g z\right), \tag{2.70}$$

if n is replaced by $\tilde{n} = n - \mathrm{i}0.5g/k_0$ in Eq. (2.16). Thus the refractive index of an active medium can be described by a complex value, where its negative imaginary part represents half of the gain coefficient g divided by the vacuum wavenumber k_0[4]. According to [4, 71, 108] the gain coefficient is connected to the rate equations by

$$g = f_\text{a}\sigma_\text{ab}N_\text{a} - f_\text{b}\sigma_\text{ba}N_\text{b} \tag{2.71}$$

with a being the index of the upper laser level and b being the index of the lower laser level. Furthermore there is $\sigma_{ji} = \sigma_{ij}$ [4, 71]. According to Fig. 2.6 and Eqs. (2.60) – (2.63) the gain coefficient for a 4-level pumping scheme can be written in absence of degeneration ($f_2 = f_1 = 1$) as

$$g = \frac{\eta_\text{p}\frac{I_\text{p}}{I_\text{s}^\text{P}}}{1 + \frac{I_\text{L}}{I_\text{s}^\text{L}} + \eta_\text{p}\frac{I_\text{p}}{I_\text{s}^\text{P}}}\sigma_{12}N \ . \tag{2.72}$$

In the same way the absorption coefficient α for the pumping process of the non-degenerated 4-level laser medium between the ground state and the pumping level can be calculated by [108]

$$\alpha = f_c\sigma_\text{cd}N_\text{c} - f_\text{d}\sigma_\text{dc}N_\text{d} = \frac{1 + \frac{I_\text{L}}{I_\text{s}^\text{L}}}{1 + \frac{I_\text{L}}{I_\text{s}^\text{L}} + \eta_\text{p}\frac{I_\text{p}}{I_\text{s}^\text{P}}}\sigma_{03}N \ . \tag{2.73}$$

where c is the index of the lower pump level and d is the index of the upper pump level. From Eqs. (2.72) and (2.73) it can be seen that the pumping and gain processes are coupled with each other, meaning that the absorption process α of the pump beam I_p depends on the laser intensity I_L and the amplification process g of the laser light I_L depends on the

---

[4] Please note that with the same ad-hoc argumentation also absorption coefficients α and the entire concept of complex refractive indices are introduced in literature. Also in the formulation given above it is possible to add an additional absorption coefficient ending up with the complex refractive index $\tilde{n} = n + \mathrm{i}0.5(\alpha - g)/k_0$. However as shown in this work, the stimulated reabsorption processes from the lower to the upper laser level is directly incorporated into the gain coefficient g, representing the stationary solution of the rate equations. Furthermore as shown in [71] it is possible to include the additional phase shift which is introduced by the atomic transition into n. However in the following this phase shift is neglected, because it is very small for most cw solid-state lasers. For solid-state lasers typically it is only relevant if the exact axial mode frequency of the laser resonator should be determined, which is not the scope of this thesis.

pump beam I_p. This coupling is caused by the population depletion of the ground level for larger pump intensities. For pump intensities much smaller than the saturation intensity for absorption I_s^p, it is assumed that

$$1 + \frac{I_\mathrm{L}}{I_\mathrm{s}^\mathrm{L}} >> \eta_\mathrm{p} \frac{I_\mathrm{p}}{I_\mathrm{s}^\mathrm{p}} \ , \tag{2.74}$$

which leads approximately to a constant pump absorption

$$\alpha \approx \sigma_{03} N \ , \tag{2.75}$$

and the well known gain staturation formula

$$g \approx \frac{\eta_\mathrm{p} \frac{I_\mathrm{p}}{I_\mathrm{s}^\mathrm{p}}}{1 + \frac{I_\mathrm{L}}{I_\mathrm{s}^\mathrm{L}}} \sigma_{12} N \ , \tag{2.76}$$

which can be found in plenty of standard textbooks [4, 71]. In appendix B similar expressions for gain and pump absorption coefficients of other important energy diagrams are given for completeness, using the same stationary solution of the corresponding rate equation system.

In this section the connection between an infinitely extended plane wave and the rate equations was shown. It serves as a basis for the discussions in section 4.2, where a vectorial beam propagation method (vBPM) is derived to propagate non-plane wave fields through laser crystals.

Chapter 3

Generalization of the Fox-Li Algorithm to a Fully Vectorial Formulation

Up to now it was shown that the general field tracing equation given by Eq. (2.22) can be simplified for the simulation of nonresonant optical systems — which fulfill the condition $||\underline{\mathcal{CP}}|| < 1$ — by the application of a Neumann series. However for laser resonators, where the resonator losses are balanced by light amplification within the active medium, there is $||\underline{\mathcal{CP}}|| = 1$ and no solution of Eq. (2.22) is known so far. Therefore in this chapter Eq. (2.22) is solved to calculate the fully vectorial transversal resonator mode of single laser cavities oscillating in single-transversal-mode operation. Thus in section 3.1 the general field tracing equation is simplified to a set of two nonlinear operator equations representing an eigenvalue problem. It turns out that this eigenvalue problem can be understood as the generalization of the scalar Fox-Li algorithm to a fully vectorial approach. After that different component and free space propagation operators which might be important for different laser resonator setups are given in section 3.2. At the end of this chapter two different eigenvalue solvers are discussed in sections 3.3 and 3.4 for the practical numerical solution of the eigenvalue problem.

3.1 Formulation of the General Eigenvalue Problem

In a nonresonant optical system all light which is emitted by one or more light sources will be either absorbed within the subdomains of the optical system or at the system boundaries at infinity. Thus for a cw operation of a nonresonant optical system, all the light which either is absorbed or leaves the system must be provided by the light sources. In contrast

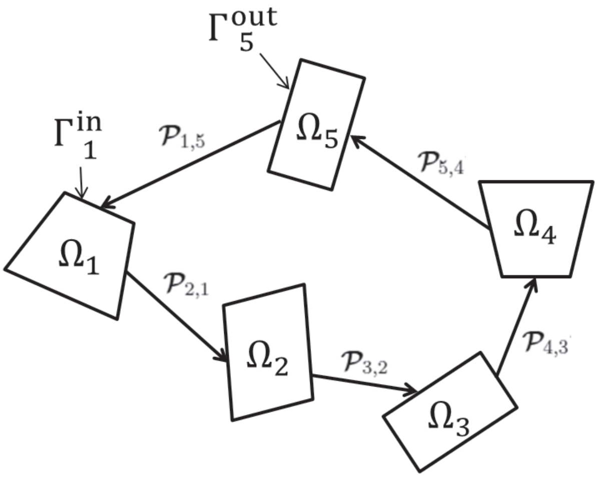

Figure 3.1 – Decomposition of an arbitrary sequential laser resonator in $M = 5$ subdomains Ω_n, which are embedded in a homogeneous medium. To form a stable transversal resonator mode, the electromagnetic field $\boldsymbol{V}_1^{\text{in}}$ given on the boundary Γ_1^{in} must reproduce itself after a complete round trip.

in a cw laser resonator there is no external light source [1], but always light inside the cavity. Here the absorption losses and the light which is leaving the cavity is counterbalanced by the light amplification within the active medium. It was already shown in section 2.4 that the amplification of light in form of a plane wave can be described by Maxwell's equations, whereas the gain, which was described by the rate equations, was included by a complex refractive index. In section 4.2 it will be shown that this concept is also valid for non-plane wave light. Thus the light propagation inside the laser resonator is governed by the general field tracing equation given by Eq. (2.22), where the external source term on the right hand side is zero. Consequently Eq. (2.22) can be reformulated to:

$$\underline{\boldsymbol{I}\boldsymbol{V}}^{\text{out}} = \underline{\boldsymbol{\mathcal{C}}\boldsymbol{\mathcal{P}}\boldsymbol{V}}^{\text{out}}. \tag{3.1}$$

If nonsequential reflections between intracavity laser components can be neglected, the indices n of the subdomains Ω_n inside the resonator can be ordered in the sequence as the light passes them. Furthermore to ensure that a stable transversal mode is formed in the cavity, the field $\boldsymbol{V}_M^{\text{out}}$ which is obtained after the last subdomain on the boundary Γ_M^{out} must reproduce the initial field $\boldsymbol{V}_1^{\text{in}}$ at the boundary Γ_1^{in} by propagating in the embedding medium from Γ_M^{out} to Γ_1^{in}. Consequently the light inside the resonator has to travel through the subdomains and the embedding medium along a closed loop. This closed loop is called resonator round trip in the following. Fig. 3.1 illustrates the subdomains and the corresponding resonator round trip inside the laser cavity. Due to the above given conditions

---

[1] Please note that a cw lasing process is typically started from spontaneous emission taking place in the active medium. Thus in the moment when the laser is started, there is an external light source. However after the mode evolution has reached the steady state the radiation generated by spontaneous emission will be neglected.

of sequential light propagation and closed resonator round trip, the propagation operator matrix is given by:

$$\underline{\boldsymbol{\mathcal{P}}} = \begin{pmatrix} 0 & 0 & \dots & 0 & \boldsymbol{\mathcal{P}}_{1,M} \\ \boldsymbol{\mathcal{P}}_{2,1} & 0 & 0 & \ddots & 0 \\ 0 & \boldsymbol{\mathcal{P}}_{3,2} & 0 & \ddots & \vdots \\ \vdots & \ddots & \ddots & \ddots & 0 \\ 0 & \dots & 0 & \boldsymbol{\mathcal{P}}_{M,M-1} & 0 \end{pmatrix}, \tag{3.2}$$

and the component operator matrix by Eq. (2.23). Plugging Eqs. (3.2) and (2.23) into Eq. (3.1) leads after matrix multiplication to a sef of M equations given by:

$$\boldsymbol{V}_n^{\text{out}} = \boldsymbol{\mathcal{C}}_n \boldsymbol{\mathcal{P}}_{n,n-1} \boldsymbol{V}_{n-1}^{\text{out}} \quad \text{for } 2 \leq n \leq M \tag{3.3}$$

and

$$\boldsymbol{V}_1^{\text{out}} = \boldsymbol{\mathcal{C}}_1 \boldsymbol{\mathcal{P}}_{1,M} \boldsymbol{V}_M^{\text{out}}. \tag{3.4}$$

The solution of $\boldsymbol{V}_1^{\text{out}}$ for the set of equations given by Eqs. (3.3) and (3.4) is:

$$\boldsymbol{V}_1^{\text{out}} = \prod_{n=2}^{M+1} \left(\boldsymbol{\mathcal{C}}_n \boldsymbol{\mathcal{P}}_{n,n-1}\right) \boldsymbol{V}_1^{\text{out}} \tag{3.5}$$

with $\boldsymbol{\mathcal{C}}_{M+1} = \boldsymbol{\mathcal{C}}_1$ and $\boldsymbol{\mathcal{P}}_{M+1,M} = \boldsymbol{\mathcal{P}}_{1,M}$. An expression similar to Eq. (3.5) can be obtained for $\boldsymbol{V}_2^{\text{out}}, \boldsymbol{V}_3^{\text{out}}, ..., \boldsymbol{V}_M^{\text{out}}$ from Eqs. (3.3) and (3.4) as well as also for $\boldsymbol{V}_1^{\text{in}}, \boldsymbol{V}_2^{\text{in}}, ..., \boldsymbol{V}_M^{\text{in}}$ due to the relation given by Eq. (2.20). Furthermore it is always possible to introduce additional subdomains (and by this additional boundaries Γ_n) in the embedding medium so that consequently Eq. (3.5) can be reformulated to

$$\boldsymbol{V} = \boldsymbol{\mathcal{R}} \boldsymbol{V} \tag{3.6}$$

to emphasize that the resonator eigenmode can be calculated on an arbitrary surface in the embedding medium. In Eq. (3.6) there is the round trip operator

$$\boldsymbol{\mathcal{R}} = \prod_{n} \left(\boldsymbol{\mathcal{C}}_n \boldsymbol{\mathcal{P}}_{n,n-1}\right) \tag{3.7}$$

which describes the light propagation in a closed loop, which starts and ends on the surface where the dominant transversal resonator eigenmode $\boldsymbol{V}$ should be calculated. Please note that the vector $\boldsymbol{V} = (V_1, V_2, ..., V_6)^{\text{T}} = (E_x, E_y, E_z, H_x, H_y, H_z)^{\text{T}}$ in Eq. (3.6) contains the three electric (E_x, E_y, E_z) and the three magnetic (H_x, H_y, H_z) field components. Thus the bold symbols represent the fully vectorial nature of Eq. (3.6). In the case that the resonator mode should be calculated on a plane in a homogeneous, isotropic and linear medium, only the two transversal electric field components V_ℓ with $\ell = 1, 2$ have to be calculated by Eq. (3.6). The remaining components can be calculated on demand directly by Eqs. (2.33) – (2.36). In this case Eq. (3.6) simplifies to

$$\begin{pmatrix} V_1 \\ V_2 \end{pmatrix} = \boldsymbol{\mathcal{R}} \begin{pmatrix} V_1 \\ V_2 \end{pmatrix} = \begin{pmatrix} \mathcal{R}_{11} & \mathcal{R}_{12} \\ \mathcal{R}_{21} & \mathcal{R}_{22} \end{pmatrix} \begin{pmatrix} V_1 \\ V_2 \end{pmatrix}. \tag{3.8}$$

Eq. (3.8) describes the mathematical problem which must be solved to calculate the dominant mode of a sequential cw laser resonator containing an active medium. Physically Eq. (3.8) can be interpreted by the following question: What kind of field distribution given on a plane reproduces itself after applying a round-trip propagation operator, described by Eq. (3.7)? Fields which fulfill this requirement are called resonator eigenmodes. However please note that strictly speaking, Eq. (3.8) can only be fulfilled, if the angular frequency ω_0 of the harmonic field amplitude $\boldsymbol{V}$ is chosen to be identical to an axial resonator mode. Otherwise there will be phase shifts ϕ_1 and ϕ_2 for both field components V_1 and V_2 after each round trip. However in the practical design and simulation of cw lasers, a small change of the resonator setup would already change the axial modes of the cavity. For example a small change of a mirror curvature would change the transversal shape of V_ℓ, which will result in a change of the Gouy phase shift and consequently in an axial mode shift. Thus it would be unpractical to determine always in a first step the exact axial modes of the resonators, to make the correct choice for ω_0. Instead it is more convenient to introduce this possible phase shifts in the problem formulation of Eq. (3.8). Therefore Eq. (3.8) can be modified to

$$\begin{pmatrix} \exp(\mathrm{i}\phi_1)V_1 \\ \exp(\mathrm{i}\phi_2)V_2 \end{pmatrix} = \boldsymbol{\mathcal{R}} \begin{pmatrix} V_1 \\ V_2 \end{pmatrix} = \begin{pmatrix} \mathcal{R}_{11} & \mathcal{R}_{12} \\ \mathcal{R}_{21} & \mathcal{R}_{22} \end{pmatrix} \begin{pmatrix} V_1 \\ V_2 \end{pmatrix}. \tag{3.9}$$

In some situations it might be useful to start the analysis of complex laser resonators not directly with the loaded laser resonator containing the active medium, but to investigate as a first step a simplified version of the resonator which neglects the active medium. This simulation of the unloaded laser resonator should provide a first insight into the effects influencing the transversal mode shape. In the absence of the active medium, Eq. (3.9) cannot be fulfilled if resonator round trip losses are present. Typical round trip losses are caused e.g. by the transmission of laser light through the resonator mirrors, diffraction losses at intracavity apertures and absorption in intracavity optical components. Thus after each round trip the transversal shape of the mode components is reproduced, but their power is damped by:

$$\text{field component round trip loss} := 1 - |\gamma_\ell|^2. \tag{3.10}$$

Using the above given definition of the field component round trip loss enables the reformulation of Eq. (3.9) to

$$\begin{pmatrix} \gamma_1 V_1 \\ \gamma_2 V_2 \end{pmatrix} = \boldsymbol{\mathcal{R}} \begin{pmatrix} V_1 \\ V_2 \end{pmatrix} = \begin{pmatrix} \mathcal{R}_{11} & \mathcal{R}_{12} \\ \mathcal{R}_{21} & \mathcal{R}_{22} \end{pmatrix} \begin{pmatrix} V_1 \\ V_2 \end{pmatrix} \tag{3.11}$$

where the field component round trip losses and the phase shifts were pooled in the complex values $\gamma_\ell = |\gamma_\ell| \exp(\mathrm{i}\phi_\ell)$. Eq. (3.11) can be rewritten formally to

$$\begin{pmatrix} \gamma_1 & 0 \\ 0 & \gamma_2 \end{pmatrix} \begin{pmatrix} V_1 \\ V_2 \end{pmatrix} = \boldsymbol{\mathcal{R}} \begin{pmatrix} V_1 \\ V_2 \end{pmatrix} = \begin{pmatrix} \mathcal{R}_{11} & \mathcal{R}_{12} \\ \mathcal{R}_{21} & \mathcal{R}_{22} \end{pmatrix} \begin{pmatrix} V_1 \\ V_2 \end{pmatrix}. \tag{3.12}$$

Please note again that in general γ_ℓ is a complex value. It can be interpreted in the following way: Its phase $\phi_\ell = \arg[\gamma_\ell]$ represents the phase shift introduced on V_ℓ by a single round trip. So in addition to the calculation of the dominant transversal resonator mode, the solution of Eq. (3.12) can be used to check if the angular frequency ω_0 of the vectorial harmonic field $\hat{\boldsymbol{V}}(\boldsymbol{r}, t)$ is an axial resonator mode. It will be an axial mode if there is a 2π modulo phase shift, so that $\exp(\mathrm{i}\phi_\ell) = 1$. The amplitude $|\gamma_\ell|$ can be interpreted according to Eq. (3.10) as a damping of the field components V_ℓ per resonator round trip. Please note that Eq. (3.12) also includes the cases when an active medium is included in the resonator round trip operator to counterbalance the resonator round trip losses. In these cases there is always $|\gamma_1| = |\gamma_2| = 1$. Thus if there is no phase shift and if an active medium is present there will be $\gamma_1 = \gamma_2 = 1$ and Eq. (3.12) simplifies to the initial Eq. (3.8).

A comparison of the scalar Fox-Li algorithm given by Eq. (2.46) with Eq. (3.12) shows that the latter can be interpreted as a fully vectorial generalization of the Fox-Li algorithm. Up to now in Eq. (3.7) no specific component and free-space propagation operators and consequently no specific resonator round trip operator $\boldsymbol{\mathcal{R}}$ in Eq. (3.12) were chosen. However any rigorous or approximative modeling technique which can be formulated to operate for electromagnetic fields can be used to simulate light propagation through the resonator subdomains or the embedding medium. Due to the vectorial treatment of the resonator mode, the application of $\boldsymbol{\mathcal{R}}$ in Eq. (3.12) is not restricted to paraxial transversal modes and thin intracavity components as is the case for the scalar approximation in Eq. (2.46). Fig. 3.2 exemplarily illustrates the round trip operator formulated by a sequence of different components and free-space propagation operators for a resonator consisting of two cavity end mirrors, one lens, a component with inhomogeneous refractive index distribution, an intracavity aperture and a binary diffractive optical element (DOE). Different modeling techniques for important optical components in resonators are given in the next section, in chapter 4 as well as in previous publications about field tracing for nonresonant optical systems [51, 52]. Also there are plenty of different free-space propagation operators avail-

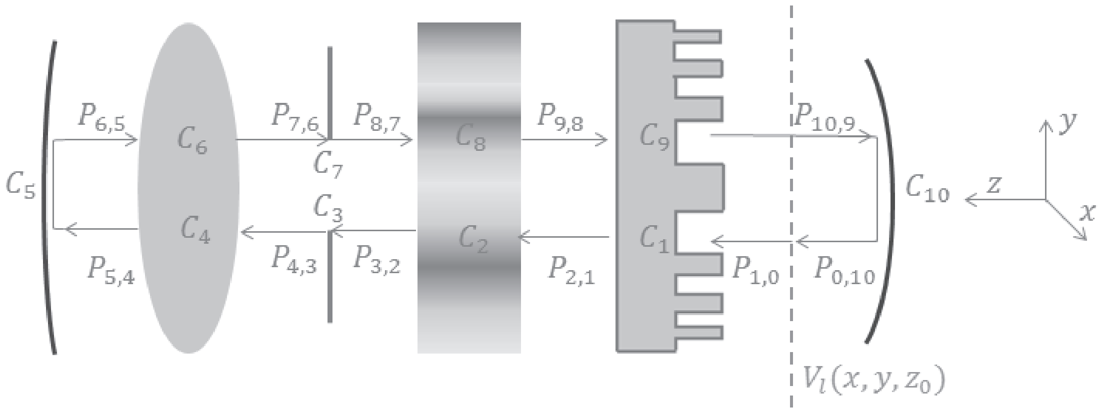

Figure 3.2 – Example for single round trip of a resonator including several optical elements: round trip operator consists of DOE operator in forward ($\boldsymbol{\mathcal{C}}_1$) and backward ($\boldsymbol{\mathcal{C}}_9$) direction, operators for inhomogeneous refractive index distributions ($\boldsymbol{\mathcal{C}}_2$ and $\boldsymbol{\mathcal{C}}_8$), intracavity aperture operators ($\boldsymbol{\mathcal{C}}_3$ and $\boldsymbol{\mathcal{C}}_7$), lens component operators in forward ($\boldsymbol{\mathcal{C}}_4$) and backward direction ($\boldsymbol{\mathcal{C}}_6$), component operators due to light reflection at cavity mirrors ($\boldsymbol{\mathcal{C}}_5$ and $\boldsymbol{\mathcal{C}}_{10}$) as well as free-space propagation operators between the optical components ($\boldsymbol{\mathcal{P}}_{1,0}$ to $\boldsymbol{\mathcal{P}}_{0,10}$).

able in literature. An overview of different free-space operators can be found in the next section and in [51, 112, 113].

It will be shown in the following section that the choice of component operators with different approximation levels will have a significant influence on the structure of the round trip operator $\boldsymbol{\mathcal{R}}$. Furthermore the structure of the round trip operator will influence the solution of Eq. (3.12). It strongly depends on whether there is a diagonal or non-diagonal structure of the round trip operator $\boldsymbol{\mathcal{R}}$. It will be shown that the problem formulated by Eq. (3.12) will transform to a single eigenvalue problem with coupled field components V_1 and V_2 and with $\gamma_1 = \gamma_2$ for non-diagonal round trip operators, or will decouple into two separate eigenvalue problems with V_1 and V_2 being independent from each other for diagonal round trip operators. Due to this transformation or decoupling of Eq. (3.12), the solutions V_1 and V_2 of Eq. (3.12) can still be called field components of the resonator eigenmode, even if the mathematical formulation of Eq. (3.12) is not an eigenvalue problem in the strict mathematical sense.

3.2 Round Trip Operator for Vectorial Resonator Modeling

In the previous section a fully vectorial generalization of the scalar Fox-Li algorithm was formulated by Eq. (3.12). Therefore a round trip operator $\boldsymbol{\mathcal{R}}$ was introduced which consists, based on the idea of field tracing and according to Eq. (3.7), of a sequence of component operators $\boldsymbol{\mathcal{C}}_n$ and free-space propagation operators $\boldsymbol{\mathcal{P}}_{n,n-1}$. In the following several important component and free-space propagation operators are given and their influence on the structure of the round trip operator is discussed. It will be shown that this structure has a significant impact on the solution of the eigenvalue problem given by Eq. (3.12). In principle there are two different round trip operator structures: Diagonal round trip operators

$$\boldsymbol{\mathcal{R}}^{\mathrm{D}} = \begin{pmatrix} \mathcal{R}_{11} & 0 \\ 0 & \mathcal{R}_{22} \end{pmatrix} \tag{3.13}$$

and non-diagonal round trip operators

$$\boldsymbol{\mathcal{R}}^{\mathrm{ND}} = \begin{pmatrix} \mathcal{R}_{11} & \mathcal{R}_{12} \\ \mathcal{R}_{21} & \mathcal{R}_{22} \end{pmatrix}. \tag{3.14}$$

Diagonal Round Trip Operator

If Eq. (3.13) is plugged into Eq. (3.12), it can be directly seen that for diagonal round trip operators the problem of Eq. (3.12) decouples into two separate eigenvalue problems

$$\gamma_1 V_1 = \mathcal{R}_{11} V_1 \tag{3.15}$$

and

$$\gamma_2 V_2 = \mathcal{R}_{22} V_2. \tag{3.16}$$

In this case the decoupled eigenvalue problems can be solved independently, which might result in different eigenvalues $\gamma_1 \neq \gamma_2$ for the different polarization components. This difference can be caused by $|\gamma_1| \neq |\gamma_2|$ and/or by $\phi_1 \neq \phi_2$. In the case of different absolute values of the eigenvalues $|\gamma_1| \neq |\gamma_2|$, only the eigenmode component with the lowest round trip loss (see definition by Eq. (3.10)) will remain in the resonator, ending up with linearly polarized light. If the difference between γ_1 and γ_2 is only caused by $\phi_1 \neq \phi_2$, the transversal eigenmode components V_ℓ have different axial modes. Diagonal round trip operators are obtained if all component operators $\boldsymbol{\mathcal{C}}_n$ and free-space propagation operators $\boldsymbol{\mathcal{P}}_{n,n-1}$ have a diagonal form[2]:

$$\boldsymbol{\mathcal{C}}_n = \begin{pmatrix} \mathcal{C}_{11} & 0 \\ 0 & \mathcal{C}_{22} \end{pmatrix} \tag{3.17}$$

and

$$\boldsymbol{\mathcal{P}}_{n,n-1} = \begin{pmatrix} \mathcal{P}_{11} & 0 \\ 0 & \mathcal{P}_{22} \end{pmatrix}. \tag{3.18}$$

---

[2] Please note that theoretically it might be also possible to obtain a diagonal round trip operator by non-diagonal component or free-space propagation operators, if their off-diagonal components cancel each other. However this might only be the case for a few realistic resonator setups. Nevertheless it is also possible to simulate such situations and the resulting diagonal round trip operator will result in the same decoupled structure given by Eqs. (3.15) and (3.16).

Thus polarization cross-talk effects which are described by the off-diagonal terms $\mathcal{C}_{12}$, $\mathcal{C}_{21}$, $\mathcal{P}_{12}$ and $\mathcal{P}_{21}$ must be neglected in the entire resonator simulation to obtain a diagonal round trip operator. In the following important diagonal component and free-space propagation operators are given.

Diagonal Jones matrix component operators

As already mentioned, it is not possible to include polarization cross-talk effects into a diagonal round trip operator formulation. Nevertheless simple vectorial effects like different losses and phase shifts per field component can be included in diagonal round trip operators by diagonal component operators. An important example for a diagonal component operator is the diagonal Jones matrix. For the simulation of intracavity Brewster plates it can be used to introduce different transmission coefficients for the different field components according to the Fresnel equations. The Jones matrix for Brewster plates is given by [83]:

$$\boldsymbol{\mathcal{C}}_n^{\text{Brewster, Jones}} = \begin{pmatrix} \left[\frac{2n}{n^2+1}\right]^2 & 0 \\ 0 & 1 \end{pmatrix} \tag{3.19}$$

with n being the real part of the refractive index of the Brewster plate, embedded in a surrounding medium with unity refractive index.

Diagonal identity matrix type operators

The condition given by Eq. (3.18) is always fulfilled for free-space propagation operators describing the light propagation in a homogeneous, linear and isotropic medium between parallel and plane boundaries. Thus the rigorous Angular Spectrum of Plane Waves (SPW) operator [103] given by Eq. (2.30) has a diagonal operator structure. It has even a diagonal identity matrix type structure, meaning that $\mathcal{P}_{11} = \mathcal{P}_{22}$. This diagonal identity matrix type structure is obtained for any free-space propagation operator which is applied to propagate an electromagnetic field between parallel and plane boundaries [114]. An important approximated operator of Eq. (2.30) is the Fresnel integral [115]

$$\boldsymbol{\mathcal{P}}_{n,n-1}^{\text{Fresnel}} = \begin{pmatrix} \mathcal{P}^{\text{Fresnel}} & 0 \\ 0 & \mathcal{P}^{\text{Fresnel}} \end{pmatrix} \tag{3.20}$$

with

$$\begin{aligned} V_\ell(x,y,z) &= \mathcal{P}^{\text{Fresnel}} V_\ell(x',y',0) \\ &= \frac{a(z)}{2\pi} \iint_{-\infty}^{\infty} V_\ell(x',y',0) \exp\left[\frac{ik}{2z}(x'^2+y'^2)\right] \exp\left[-\frac{ik}{z}(x'x+y'y)\right] dx'dy' \end{aligned} \tag{3.21}$$

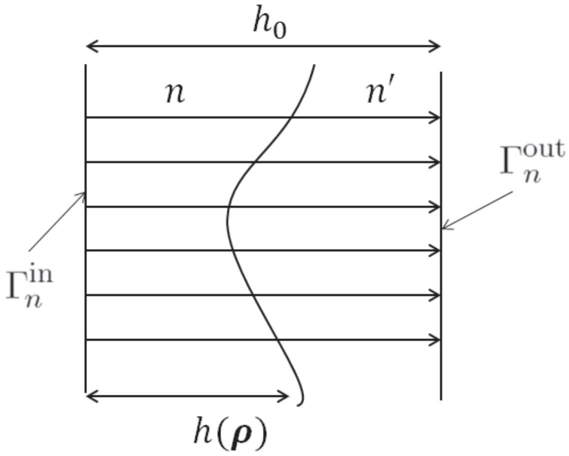

Figure 3.3 – Illustration of the light propagation through a single interface with the height profile $h(\boldsymbol{\rho})$ by the thin element approximation [51]: A position dependent phase shift and the effect of light absorption are multiplied on the initial field given on the boundary Γ_n^{in}. Therefore the optical path length (OPL) is evaluated along rays starting at different lateral positions $\boldsymbol{\rho}$ and propagating parallel to the optical axis to the boundary Γ_n^{out}. Refraction effects at the interface are neglected.

for paraxial fields with

$$a(z) = \frac{k\exp(\mathrm{i}kz)}{\mathrm{i}z}\exp\left[\frac{\mathrm{i}k}{2z}(x^2+y^2)\right] \ . \tag{3.22}$$

Further diagonal identity matrix type free-space propagation operators can be found in [51, 112, 113].

In the special case that only diagonal identity matrix type free-space propagation and component operators are used to formulate the round trip operator, an diagonal round trip operator with identity matrix type structure $\mathcal{R}_{11} = \mathcal{R}_{22}$ is obtained. In this case $\gamma_1 = \gamma_2$, resulting in a degeneration of Eq. (3.12) to the scalar eigenvalue problem given by Eq. (2.46). Thus the resonator has no preferred polarization direction, resulting in unpolarized light emitted by the laser. What diagonal identity matrix type round trip operators mean physically is that polarization cross-talk is neglected (through the non-diagonal elements $\mathcal{R}_{21}$ and $\mathcal{R}_{12}$ being zero) and the effect on both field components V_ℓ is the same, because $\mathcal{R}_{11} = \mathcal{R}_{22}$. Free-space propagation operators $\boldsymbol{\mathcal{P}}_{n,n-1}$, describing the light propagation between two parallel planes have (as already mentioned above) always a diagonal identity matrix type structure.

As already mentioned above, an identity matrix type structure of $\boldsymbol{\mathcal{R}}$ is obtained only if exclusively diagonal identity matrix type component operators

$$\boldsymbol{\mathcal{C}}_n = \begin{pmatrix} \mathcal{C} & 0 \\ 0 & \mathcal{C} \end{pmatrix} \tag{3.23}$$

are applied for the simulation of light propagation through the resonator subdomains. Thus all polarization effects taking place in the resonator must be neglected. Again the arguments given by appendix A show that the diagonal components $\mathcal{C}_{11} = \mathcal{C}_{22} = \mathcal{C}$ of the diagonal identity matrix type component operators can be only a solution of the inhomogeneous wave equation given by Eq. (2.44). In literature several approximated solutions of Eq. (2.44) can be found. Most common solvers, including the Gaussian beam propagation [69, 71], the Collins integral [48–50], and the BPM [43–47], are based on a combination of the Fresnel integral given by Eq. (3.21) with the thin element approximation (TEA) [51]. In operator notation this means:

$$\mathcal{C} = \prod \left(\mathcal{C}^{\mathrm{TEA}} \mathcal{P}^{\mathrm{Fresnel}}\right), \tag{3.24}$$

with the TEA operator:

$$\mathcal{C}^{\mathrm{TEA}} = t^{\mathrm{Fresnel}} \exp\left[\mathrm{i}\Phi(\boldsymbol{\rho}) - \alpha(\boldsymbol{\rho})\right]. \tag{3.25}$$

Here t^{Fresnel} describes the Fresnel losses at an optical interface. It is calculated by the Fresnel equations [30] assuming normal light incidence. The position dependent phase shift $\Phi(\boldsymbol{\rho})$ and the effect of light absorption $\alpha(\boldsymbol{\rho})$ are calculated by evaluating the optical path length (OPL) of rays starting at different lateral positions [51]. For the OPL analysis light refraction at the optical interfaces is neglected as illustrated in Fig. 3.3. Thus the rays are propagating straight through the optical components. For light transition through a single optical interface (Fig. 3.3) which separates two media with the refractive indices n and n' there is [51]:

$$\Phi(\boldsymbol{\rho}) = \frac{2\pi}{\lambda}\mathrm{OPL}(\boldsymbol{\rho}) = \frac{2\pi}{\lambda}\left[(n - n')h(\boldsymbol{\rho}) + n'h_0\right] \tag{3.26}$$

and

$$\alpha(\boldsymbol{\rho}) = \frac{2\pi}{\lambda}\left[(\kappa - \kappa')h(\boldsymbol{\rho}) + \kappa'h_0\right] \tag{3.27}$$

with the height profile $h(\boldsymbol{\rho})$ of the interface, the absorption coefficients κ and κ' and the the vacuum wavelength of the light λ. Please note that typically if the light propagation through a subdomain Γ_n is modeled by the Collins integral or the Gaussian beam propagation method, the subdomain size is chosen in a way that several optical components and the embedding medium between them are pooled in the subdomain. A numerical example for modeling the light propagation by the Collins integral through two lenses pooled in a single resonator subdomain is given in section 5.1.

Non-Diagonal Operators

If the non-diagonal round trip operator given by Eq. (3.14) is inserted into Eq. (3.12), there is a coupling between the two field components due to polarization cross-talk, which is caused by nonzero off-diagonal terms $\mathcal{R}_{12}$ and $\mathcal{R}_{21}$. Due to the coupling of the field components, there must also be a coupling of their round trip losses and phase shifts[3]. This is only the case for the degenerated situation, when $\gamma_1 = \gamma_2$. Then Eq. (3.12) can be interpreted as an eigenvalue problem, where both eigenmode components V_ℓ have the same eigenvalue. Again according to Eq. (3.10) the amplitude of the eigenvalue can be interpreted in terms of the resonator round trip loss per field component, which must be equal for both components due to the polarization cross-talk. Furthermore due to $\gamma_1 = \gamma_2$, an equal phase shift $\phi_1 = \phi_2$ per round trip is guaranteed. Please note that there is a fundamental difference in the case of $\gamma_1 = \gamma_2$ between diagonal identity matrix type and non-diagonal operators. For diagonal identity matrix type operators the eigenmode components also degenerate to the scalar case of $V_1 = V_2$. For non-diagonal operators both eigenmode components V_ℓ can be different. A non-diagonal round trip operator is obtained if the operator sequence given by Eq. (3.7) contains at least one non-diagonal free-space propagation or component operator. In the remaining part of this section as well as in chapter 4 several important non-diagonal operators for the simulation of intracavity laser components are given.

Non-diagonal free-space propagation operators

Up to now only free-space propagation operators describing the light propagation between parallel plane boundaries were discussed. In this case the free-space propagation operators have a diagonal identity matrix type structure [114]. However several resonator setups contain optical components tilted with respect to the optical axis, like folded or misaligned resonators. Thus in several situations it might be necessary to propagate an electromagnetic field given on a plane boundary $\Gamma_{n-1}^{\text{out}}$ of the subdomain Ω_{n-1} to a nonparallel plane boundary Γ_n^{in} of the next subdomain Ω_n. Typically the electric and magnetic field vectors $\boldsymbol{E}_{n-1}^{\text{out}}(\boldsymbol{r} \in \Gamma_{n-1}^{\text{out}})$ and $\boldsymbol{H}_{n-1}^{\text{out}}(\boldsymbol{r} \in \Gamma_{n-1}^{\text{out}})$ given on $\Gamma_{n-1}^{\text{out}}$ are expressed in the same Cartesian coordinate basis $(\hat{\boldsymbol{x}}, \hat{\boldsymbol{y}}, \hat{\boldsymbol{z}})$ as the position vector $\boldsymbol{r}$. Mathematically this means [114]:

$$\boldsymbol{r} = x\hat{\boldsymbol{x}} + y\hat{\boldsymbol{y}} + z\hat{\boldsymbol{z}} \tag{3.28}$$

and

$$\boldsymbol{E}_{n-1}^{\text{out}}(\boldsymbol{r}) = E_x^{\text{out}}(\boldsymbol{r})\hat{\boldsymbol{x}} + E_y^{\text{out}}(\boldsymbol{r})\hat{\boldsymbol{y}} + E_z^{\text{out}}(\boldsymbol{r})\hat{\boldsymbol{z}}. \tag{3.29}$$

---

[3] A physical justification of this statement is given later in section 5.1.

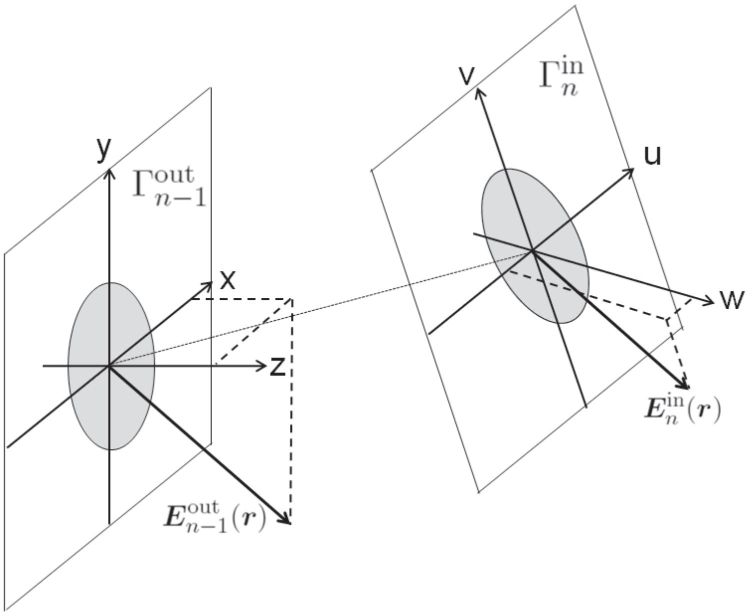

Figure 3.4 – Free-space propagation of light between non-parallel plane boundaries $\Gamma_{n-1}^{\text{out}}$ and Γ_{n}^{in}: Two Cartesian coordinate systems $x-y-z$ and $u-v-w$ are created, having their origins located on the corresponding boundaries, so that $z=0$ and $w=0$. The absolute direction of the electric field vector $\boldsymbol{E}$ is not changing during the free-space propagation. However due to the expression of the polarization vector relative to different coordinate bases, there are off-diagonal terms in the free-space propagation operator.

Here the the discussion of the magnetic field $\boldsymbol{H}$ is skipped, due to the fact that in a homogeneous, isotropic and linear medium only two field components are independent. The remaining field components can be calculated on demand by Eqs. (2.34) – (2.36). Furthermore as illustrated in Fig. 3.4 it is convenient to formulate the propagated electric field $\boldsymbol{E}_n^{\text{in}}(\boldsymbol{r} \in \Gamma_n^{\text{in}})$ in a Cartesian coordinate system with another coordinate basis $(\hat{\boldsymbol{u}}, \hat{\boldsymbol{v}}, \hat{\boldsymbol{w}})$ [114]:

$$\boldsymbol{r} = u\hat{\boldsymbol{u}} + v\hat{\boldsymbol{v}} + w\hat{\boldsymbol{w}} \tag{3.30}$$

and

$$\boldsymbol{E}_n^{\text{in}}(\boldsymbol{r}) = E_u^{\text{in}}(\boldsymbol{r})\hat{\boldsymbol{u}} + E_v^{\text{in}}(\boldsymbol{r})\hat{\boldsymbol{v}} + E_w^{\text{in}}(\boldsymbol{r})\hat{\boldsymbol{w}}. \tag{3.31}$$

The transformation of the two coordinate systems is given by:

$$\begin{pmatrix} u \\ v \\ w \end{pmatrix} = \underline{\boldsymbol{T}} \begin{pmatrix} x \\ y \\ z \end{pmatrix} = \begin{pmatrix} t_{11} & t_{12} & t_{13} \\ t_{21} & t_{22} & t_{23} \\ t_{31} & t_{32} & t_{33} \end{pmatrix} \cdot \begin{pmatrix} x \\ y \\ z \end{pmatrix} \tag{3.32}$$

where $\underline{\boldsymbol{T}}$ is the transformation matrix, describing the coordinate rotations and translations. If the coordinate systems are chosen as shown in Fig. 3.4, meaning that their origins are located in the planes $\Gamma_{n-1}^{\text{out}}$ and Γ_n^{in}, respectively, there is $z=0$ and $w=0$ and the field propagation between non-parallel planes can be described by the non-diagonal free-space propagation operator:

$$\begin{pmatrix} E_u^{\text{in}}(u,v,0) \\ E_v^{\text{in}}(u,v,0) \end{pmatrix} = \begin{pmatrix} \mathcal{P}_{11} & \mathcal{P}_{21} \\ \mathcal{P}_{12} & \mathcal{P}_{22} \end{pmatrix} \begin{pmatrix} E_x^{\text{out}}(x,y,0) \\ E_y^{\text{out}}(x,y,0) \end{pmatrix}. \tag{3.33}$$

Here again it is only necessary to calculate two field components. The remaining components can be calculated on demand by Eqs. (2.33) – (2.36). Please note that in Eq. (3.33) the off-diagonal terms $\mathcal{P}_{12}$ and $\mathcal{P}_{21}$ describe in a mathematical sense a polarization cross-talk. However this cross-talk is, as proved in [114], only caused by the coordinate transformation. So its origin is a mathematical requirement and has no physical meaning (this is in contrast to non-diagonal component operators, where the off-diagonal terms normally have a physical meaning). Nevertheless of course it has the same influence on the structure of the round trip operator as physically motivated polarization cross-talk effects. In the following no mathematical details are given for the exact formulation of non-diagonal free-space propagation operators. Interested readers are referred to a previous publication [114] which gives a rigorous as well as an approximative free-space propagation operator for the field propagation between non-parallel planes.

In principle it is also possible to calculate the light distribution on non-plane boundaries Γ_n for the subdomains Ω_n. However it is always possible to calculate at first the light distribution on a plane boundary using the above given free-space propagation operator. If the plane boundary is chosen to be close to the non-plane target boundary then the thin element approximation or other suitable geometrical optics operators [51, 116] can be used to project the field from the plane to the non-plane boundary. This approximated approach has the advantage that for the free-space propagation, a numerically efficient uniform fast Fourier Transformation (FFT) [117] can be used. Alternatively a numerically more extensive evaluation of the rigorous Rayleigh-Sommerfeld diffraction integral is also possible [118].

Non-diagonal Jones matrix component operators

General, non-diagonal and position dependent Jones matrices $\boldsymbol{\mathcal{C}}_n^{\text{Jo}}$ are an example for a non-diagonal component operator, when the modeling of the subdomain is reduced to its effect on the polarization. Important Jones matrices are used e.g. for [83]

Linear polarizers:

$$\boldsymbol{\mathcal{C}}_n^{\text{Jo,Pol}} = \begin{pmatrix} \cos^2\alpha & \sin\alpha\cos\alpha \\ \cos\alpha\sin\alpha & \sin^2\alpha \end{pmatrix} \tag{3.34}$$

with α being the tilt angle between the x-axis and the polarizer's transmission axis.

Azimuthal-birefringent components:

$$\mathcal{C}_n^{\text{Jo,Az-B}} = \begin{pmatrix} \exp(\mathrm{i}\Phi)\cos^2\theta + \sin^2\theta & [\exp(\mathrm{i}\Phi) - 1]\sin\theta\cos\theta \\ [\exp(\mathrm{i}\Phi) - 1]\sin\theta\cos\theta & \exp(\mathrm{i}\Phi)\sin^2\theta + \cos^2\theta \end{pmatrix} \tag{3.35}$$

with θ being the azimuthal position angle and $\Phi = [\frac{2\pi}{\lambda}(n_r - n_\theta)]l$ being the relative phase shift between the azimuthal and radial field components after propagating over a distance l. Here n_r and n_θ represent the corresponding refractive indices for azimuthal and radial field components.

Phase retarder:

$$\mathcal{C}_n^{\text{Jo,PR}} = \begin{pmatrix} \cos^2\alpha + \sin^2\alpha\exp(\mathrm{i}\Phi) & \sin\alpha\cos\alpha[1 - \exp(\mathrm{i}\Phi)] \\ \sin\alpha\cos\alpha[1 - \exp(\mathrm{i}\Phi)] & \sin^2\alpha + \cos^2\alpha\exp(\mathrm{i}\Phi) \end{pmatrix} \tag{3.36}$$

with α being the tilt angle between the x-axis and the phase retarder's transmission axis and Φ being the phase delay.

Polarization rotator:

$$\mathcal{C}_n^{\text{Jo,Pol-Rot}} = \begin{pmatrix} \cos\beta & -\sin\beta \\ \sin\beta & \cos\beta \end{pmatrix} \tag{3.37}$$

with β being the polarization rotation angle.

Non-diagonal Brewster window component operator

In section 5.1 the simulation of a plane resonator including a Brewster window is shown. In the simplest case, a Brewster window is a glass plate consisting of two parallel interfaces which are tilted with respect to the optical axis by the Brewster angle. Polarization cross-talk effects are included in the simulation due to the modeling of the Brewster window by applying the non-diagonal interface operator on each interface of the Brewster window. This interface operator was published previously [119, 120], so no mathematical derivation of the operator will be given in detail here. However, due to the relevance of the operator in the simulation results obtained in section 5.1, the physical reason for polarization cross-talk caused by light propagation through a tilted plane interface will be discussed in the following.

The rigorous interface operator requires as an initial condition the light distribution in the plane of the interface. Thus typically the complex amplitudes of the harmonic field components $V_\ell(x, y, z)$ are calculated in the plane of the interface by applying the non-

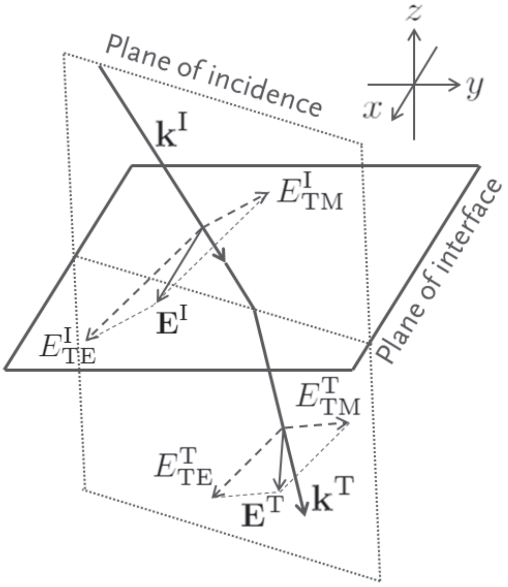

Figure 3.5 – Polarization cross-talk at a single plane interface for an incident plane wave: The polarization vector $\boldsymbol{E}^{\mathrm{I}}$ of the incident plane wave is decomposed in its TE and TM components. For non-normal incident plane waves, Fresnel equations lead to different transmission coefficients τ_{TE} and τ_{TM}. Consequently, the initial ratio $E^{\mathrm{I}}_{\mathrm{TE}}/E^{\mathrm{I}}_{\mathrm{TM}}$ is changed to $E^{\mathrm{T}}_{\mathrm{TE}}/E^{\mathrm{T}}_{\mathrm{TM}} = (\tau_{\mathrm{TE}}E^{\mathrm{I}}_{\mathrm{TE}})/(\tau_{\mathrm{TM}}E^{\mathrm{I}}_{\mathrm{TM}})$ and the direction of $\boldsymbol{E}^{\mathrm{I}}$ is changed to $\boldsymbol{E}^{\mathrm{T}}$.

diagonal free-space propagation operators mentioned above. After that, the initial field is decomposed into a set of plane waves using a Fourier transformation. Then the Fresnel equations are applied on each plane wave $\boldsymbol{E}^{\mathrm{I}}$. Thus each plane wave has to be represented in its principal coordinate system. This coordinate system is spanned by the plane of incidence (which consists of the incident wavevector $\boldsymbol{k}^{\mathrm{I}}$ and the interface normal vector $\boldsymbol{n}$) and an axis which is orthogonal to this plane of incidence. As a consequence, for each plane wave in its principal coordinate system a TE and TM polarization component is obtained. Fig. 3.5 illustrates an incident plane wave, which has the wavevector $\boldsymbol{k}^{\mathrm{I}}$ and electric field vector $\boldsymbol{E}^{\mathrm{I}}$. To apply Fresnel coefficients, $\boldsymbol{E}^{\mathrm{I}}$ is decomposed into $E^{\mathrm{I}}_{\mathrm{TE}}$ and $E^{\mathrm{I}}_{\mathrm{TM}}$. The application of the Fresnel equations leads to a transmitted plane wave with the wavevector $\boldsymbol{k}^{\mathrm{T}}$ and electric field components $E^{\mathrm{T}}_{\mathrm{TE}} = \tau_{\mathrm{TE}}E^{\mathrm{I}}_{\mathrm{TE}}$ and $E^{\mathrm{T}}_{\mathrm{TM}} = \tau_{\mathrm{TM}}E^{\mathrm{I}}_{\mathrm{TM}}$. For non-normal incident plane waves, the Fresnel equations predict different transmission coefficients τ_{TE} and τ_{TM} for TE and TM field components. This effect is in particular strong for incident angles around the Brewster angle. As a consequence the relation between TE and TM field components will change by passing through the interface. The direction of polarization of the combination of both field components in the initial coordinate system will change from $\boldsymbol{E}^{\mathrm{I}}$ to $\boldsymbol{E}^{\mathrm{T}}$. This change of the polarization direction can be interpreted as polarization cross-talk. The transmission of light through a single interface will additionally alter the direction of the TM component due to the change of the propagation direction of the plane wave caused by Snell's law. This change of direction also has an influence on the change of the polarization direction. However, the Brewster window typically consists of two parallel interfaces. Thus the direction change of the TM component by Snell's law at the first interface will be compensated by the second interface. So, in summary, the polarization cross-talk a general beam experiences by propagating through a plane interface is caused by different Fresnel reflection losses for the TE and TM field components of the beam's angular spectrum.

Summary of Section 3.2

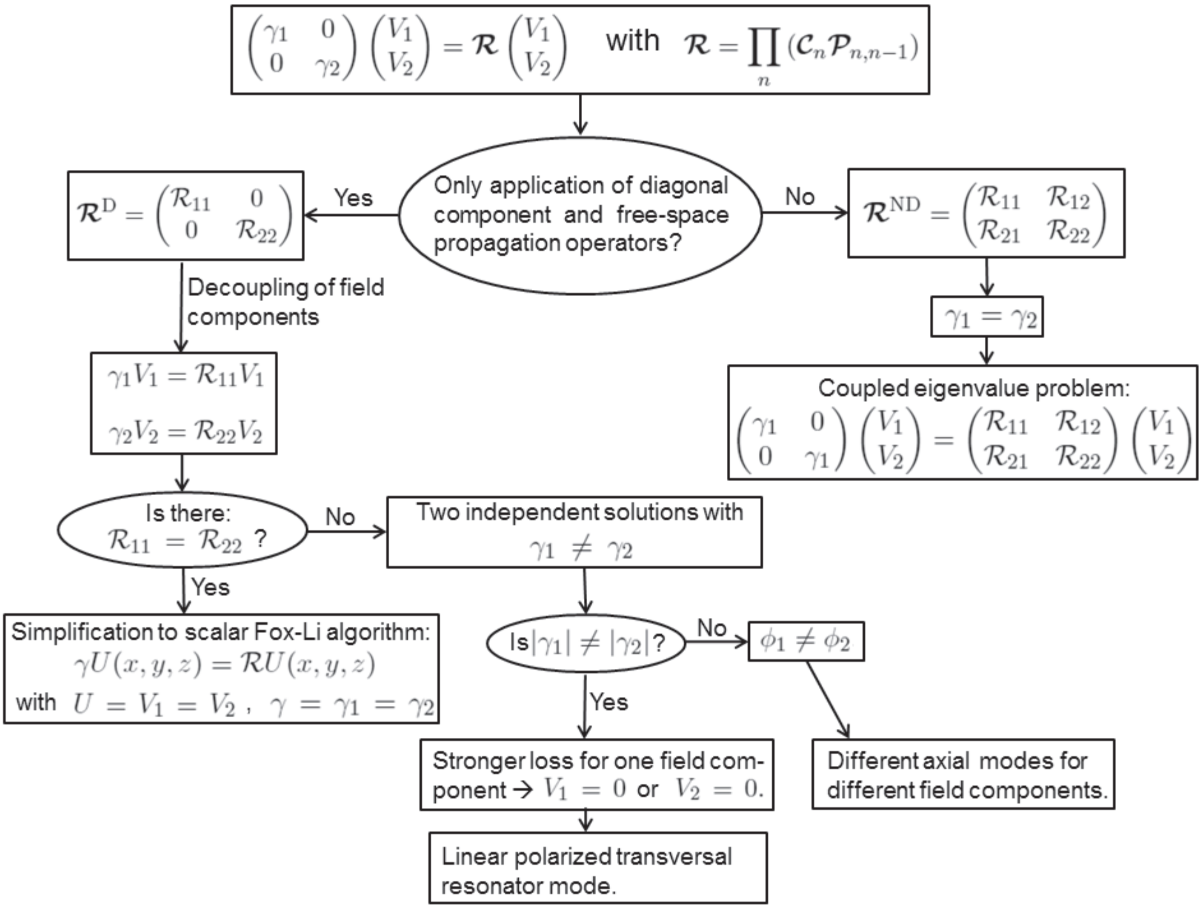

Figure 3.6 – Dependent on the structure of the round trip operator, the eigenvalue problem given by Eq. (3.12) has different solutions.

In this section it was shown that Eq. (3.12) has, dependent on the structure of the round trip operator, different kinds of solutions. Fig. 3.6 gives a summary of these different solution classes. The round trip operator has either a non-diagonal or diagonal structure. For the diagonal structure, there is the special case of identity matrix type structure. An identity matrix type round trip operator can only be obtained if identity matrix type component and identity matrix type free-space propagation operators are used only. Diagonal round trip operators are only constructed by diagonal component and free-space propagation operators. Otherwise there is a non-diagonal round trip operator. Furthermore it was discussed that the inclusion of an active medium, which balances resonator round trip losses and is modeled by a suitable component operator, will cause $||\boldsymbol{\mathcal{R}}|| = 1$ and $|\gamma_1| = |\gamma_2| = 1$. Consequently the round trip operator and by that also the solution of Eq. (3.12) depends on the applied component and free-space propagation operators. Several important operators for the practical simulation of different laser resonator setups were given in this section. Further non-diagonal field tracing component operators which take polarization as well as other propagation effects into account can be obtained e.g. by the geometrical optics operator [51], Maxwell solvers or any other simulation technique which can be formulated for electromagnetic fields. Two important non-diagonal component operators for anisotropic materials are also given in chapter 4. In conclusion: if anisotropic effects should be included in the simulation or if the area of validity of the paraxial approximation is left, non-diagonal operators are quite normal and the solution of the coupled eigenvalue problem becomes essential.

3.3 Simple Eigenvalue Solver: Iterative Power Method

Up to now only the formulation of the mathematical problem for the calculation of the dominant transversal resonator mode of arbitrary cw laser resonators was discussed. It was shown that the simulation task can be formulated by the eigenvalue problem given by Eq. (3.12). As mentioned in the summary of the previous section, the exact structure of this eigenvalue problem depends on the component and free-space propagation operators applied. The choice of these operators depends on the required simulation accuracy. Thus an increase of the simulation accuracy might change the eigenvalue problem structure e.g. from the uncoupled problem given by Eqs. (3.15) and (3.16) to the coupled eigenvalue problem with non-diagonal round trip operator structure. In the following three numerical solvers for the eigenvalue problem given by Eq. (3.12) will be given. In algebra several different eigenvalue solvers can be found. However most of them, e.g. the Newton method [121], cannot be applied to the laser resonator eigenmode calculation, because they require round trip operators $\boldsymbol{\mathcal{R}}$ in a closed matrix form. For most of the resonator setups this closed matrix form of $\boldsymbol{\mathcal{R}}$ is not known. That is why in literature just a few alternative eigenvalue solver techniques are commonly used in laser resonator analysis. The most important techniques are based on the Schmidt approach [122,123], the Prony method [124,125], the Arnoldi method [126,127], the selective iteration method [105] or on the spectral approach of Feit and Fleck [128]. Up to now in the literature all of these techniques are either applied only for the case of round trip operators with identity matrix type structures where Eq. (3.12) degenerates to a single scalar eigenvalue problem, or are restricted to linear round trip operators. However for the practical resonator simulation it would be preferable to have a formulation for the eigenvalue solver which could handle all the possible different eigenvalue problem structures of Eq. (3.12), ranging from the scalar up to the coupled case for either linear or nonlinear round trip operators with an unknown closed matrix form. In this section the iterative power method, which was used by Fox and Li [7, 8] to solve the scalar eigenvalue problem, is modified in a way that it can be used to solve the general eigenvalue problem given by Eq. (3.12). However as discussed later, this power method might suffer from low convergence speed. That is why in the following section two eigenvalue solvers which are based on the vector extrapolation method are given. Compared to the power method these techniques have an accelerated convergence speed.

Fox and Li showed [7, 8] that their scalar eigenvalue problem given by Eq. (2.42) could be solved numerically using the power iteration method. The power iteration method can also solve the general problem formulated by Eq. (3.12) applying iteratively several round trip operations:

$$\begin{pmatrix} V_1^{(j+1)} \\ V_2^{(j+1)} \end{pmatrix} = \frac{1}{\alpha^{(j)}} \boldsymbol{\mathcal{R}} \begin{pmatrix} V_1^{(j)} \\ V_2^{(j)} \end{pmatrix} \tag{3.38}$$

with $V_\ell^{(j)}$ representing the propagation result after round trip number j. $\alpha^{(j)}$ represents a suitable normalization factor after each iteration, which is discussed later. The dominant transversal resonator eigenmode is obtained by

$$W_\ell = \lim_{j \to \infty} V_\ell^{(j)} \tag{3.39}$$

and its corresponding eigenvalue by convergence of

$$\gamma_\ell = \lim_{j \to \infty} \gamma_\ell^{(j)} \tag{3.40}$$

with

$$\gamma_\ell^{(j)} = \frac{\iint \left(V_\ell^{(j)}(x, y, z_0) \alpha^{(j)} V_\ell^{*(j+1)}(x, y, z_0) \right) \mathrm{d}x\mathrm{d}y}{\iint \left(V_\ell^{(j)}(x, y, z_0) V_\ell^{*(j)}(x, y, z_0) \right) \mathrm{d}x\mathrm{d}y}. \tag{3.41}$$

Here * denotes the complex conjugate and the variable dependency (x, y, z_0) is used to emphasize the fact that the eigenvalue is typically calculated by integration over a single plane boundary Γ_0.

Fox and Li [7] already mentioned that without a gain medium, the power of the resonator mode will decay with successive round trips. Therefore they normalized the mode after each round trip, so that the maximum amplitude is unity:

$$\max |U^{(j)}(x, y, z_0)| = 1. \tag{3.42}$$

In the case of the vectorial problem given by Eq. (3.12) a normalization in the fashion of Eq. (3.42) would cause an inadvertent modification of the power ratio between the E_x and E_y component. Hence a Jones vector invariant normalization factor

$$\alpha^{(j)} = \left[\sum_{\ell=1,2} \iint \left| V_\ell^{(j)}(x, y, z_0) \right|^2 \mathrm{d}x\mathrm{d}y \right]^{1/2} \tag{3.43}$$

is used in the following. Please note that this normalization is only necessary for resonator simulations including no active medium (meaning that $||\boldsymbol{\mathcal{R}}|| < 1$) independent on whether the round trip operator is diagonal or non-diagonal. For resonators with gain (meaning that $||\boldsymbol{\mathcal{R}}|| = 1$), the normalization factor after each iteration is unity.

Fox and Li [7,8] already showed that if the iterative power method is applied on the scalar eigenvalue problem given by Eq. (2.42), it will converge to the most dominant eigenmode. This most dominant eigenmode is defined by the corresponding eigenvalue γ_1 with the largest absolute value, meaning that

$$|\gamma_1| > |\gamma_2| > ... > |\gamma_n| \tag{3.44}$$

with all possible eigenvalues $\gamma_1 ... \gamma_n$ of the scalar eigenvalue problem. Strictly speaking Fox and Li's argumentation is only true for linear round trip operators of the scalar eigenvalue problem. However as proven in [129, 130], the iterative power method can be also applied to all structures of the general eigenvalue problem represented by Eq. (3.12) with $\boldsymbol{\mathcal{R}}$ being a nonlinear operator. Also in these cases the iterative power method converges to the most dominant eigenvector W_ℓ with the largest absolute eigenvalue [129]

$$|\gamma_{\ell,1}| > |\gamma_{\ell,2}| > ... > |\gamma_{\ell,n}| \tag{3.45}$$

if the iterative procedure given by Eq (3.38) is started by an initial condition $V_\ell^{(0)} \in \boldsymbol{\mathcal{H}}$ which does not entirely lie in $\boldsymbol{\mathcal{M}}^\perp$. Here $\boldsymbol{\mathcal{H}}$ is the Hilbert space of $\boldsymbol{\mathcal{R}}$. Furthermore there is $\boldsymbol{\mathcal{H}} = \boldsymbol{\mathcal{M}} \otimes \boldsymbol{\mathcal{M}}^\perp$ where $\boldsymbol{\mathcal{M}}$ is the subspace spanned by the most dominant eigenvector W_ℓ [129]. Thus to guarantee the convergence of the power method, $V_\ell^{(0)}$ is chosen as a field with random phase distribution to ensure that it contains a component pointing into the direction of W_ℓ. As in the case of the scalar eigenvalue problem, also the convergence of the power method for the solution of Eq. (3.12) strongly depends on the root convergence index $\left|\frac{\gamma_{\ell,2}}{\gamma_{\ell,1}}\right|$, where $\gamma_{\ell,2}$ represents the second dominant eigenvalue [129]. As a consequence, the convergence of the power method is poor if there is a second eigenmode with round trip losses close to those of the dominant eigenmode. This slow computational performance of the power method (which is also shown by several numerical examples in chapter 5) is very critical in parametric optimization of resonator setups, where the dominant eigenmode has to be calculated plenty of times till the best resonator setup for the specific application is found.

3.4 Accelerated Eigenvalue Solver: Vector Extrapolation Methods

To overcome the convergence problems of the iterative power method two polynomial-type vector extrapolation methods, namely the minimal polynomial extrapolation (MPE) and the reduced rank extrapolation (RRE), are applied to the problem of Eq. (3.12), resulting in a drastically increased computational speed of the dominant eigenmode calculation. Both techniques do not require a closed matrix form of $\boldsymbol{\mathcal{R}}$ and are not limited to decoupled or linear types of Eq. (3.12). In principle they can be applied to any nonlinear round trip operator $\boldsymbol{\mathcal{R}}$ and to either coupled or decoupled types of Eq. (3.12).

The aim of this section is the explicit application of the MPE and the RRE for accelerated dominant eigenmode calculation of laser resonators based on Eq. (3.12). Therefore no general mathematical derivation and detailed convergence discussion of both methods is given. A detailed mathematical discussion can be found in Sidi [131].

Sidi [131] showed that the exact solution $\lim_{j\to\infty} V_\ell^{(j)} = W_\ell$ of Eq. (3.12) can be constructed by a weighted sum of k iteration results $V_\ell^{(j)}$:

$$W_\ell = \sum_{j=0}^{k} \beta_\ell^{(j)} V_\ell^{(j)} \tag{3.46}$$

where $\beta_\ell^{(j)}$ represents the weighting factors. Please note that the iteration results $V_\ell^{(j)}$ are calculated by the same iterative procedure given by Eq. (3.38) and with the same normalization factor $\alpha^{(j)}$ as for the iterative power method. The calculation algorithm for $\beta_\ell^{(j)}$ is different depending on whether MPE or RRE is used. The comparison of Eq. (3.46), which is the fundamental equation for the vector extrapolation methods, with the power method given by Eq. (3.38), qualitatively shows the reason why MPE and RRE will have a faster convergence compared to the power method. In the case of MPE and RRE several iteration results are used to construct the dominant eigenmode. In the case of the power method only the previous iteration result $V_\ell^{(j)}$ is used in each iteration step. Fig. 3.7 again illustrates the different working principles of the power method and the techniques based on vector extrapolation. Please note that besides the efficient calculation of the weighting factors $\beta_\ell^{(j)}$ a cycling and a multi round trip approach [131] for the MPE and RRE algorithms are used to avoid the storage of a large number of k iteration results $V_\ell^{(j)}$. Both approaches will be discussed later. Otherwise, especially for iteration results $V_\ell^{(j)}$

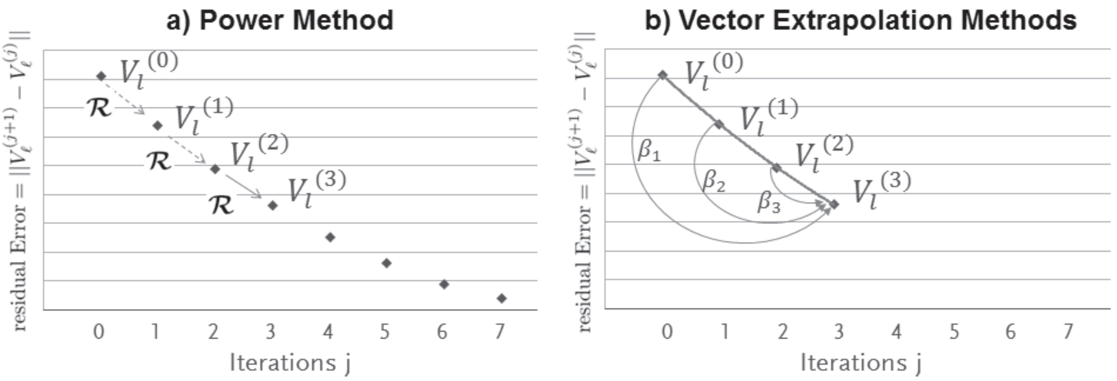

Figure 3.7 – Fundamental working principle of a) power method and b) vector extrapolation methods. In a) only the prior iteration result is used to construct the next one. In case b) several iteration results are used to calculate the next iteration.

requiring a high number of sampling points, the summation in Eq. (3.46) would be very time and memory consuming.

Compared to other eigenvalue solvers based e.g. on the Newton method, the RRE and MPE are defined exclusively by the iteration results $V_\ell^{(j)}$, no matter how they have been obtained. This means that the RRE and MPE algorithms do not require a representation of the round trip operator $\boldsymbol{\mathcal{R}}$ in a closed matrix form, which is typically not possible to obtain. Also both vector extrapolation techniques can be applied to nonlinear round trip operators or to polarization-coupled eigenvalue problems, which makes these two polynomial-type vector extrapolation methods very suitable for resonator modeling.

In what follows within this section the harmonic field components $V_\ell^{(j)}$ are calculated on a plane boundary with axial position z_0 within the laser cavity. The axial position can be arbitrary, as long as it is located in a homogeneous isotropic medium. Thus the fields are numerically sampled on a 2-dimensional grid (x_n, y_m) with $N \times M$ sampling points. Consequently there is $V_\ell^{(j)} \in \mathbb{C}^{N\times M}$. The elements of this 2-dimensional sampling grid can be rewritten in a vector with $O = N \times M$ elements so that there is $V_\ell^{(j)} \in \mathbb{C}^{O}$.

Minimal polynomial extrapolation (MPE)

Sidi [131] already mentioned that the exact dominant transversal eigenmode $W_\ell(x, y, z_0)$ is constructed via a minimal polynomial with k-degrees resulting in Eq. (3.46). In general, k would be very close to O, which would make the solution of Eq. (3.46) very inefficient. Therefore an approximate solution [131]

$$W_{\ell,s,k}^{\mathrm{MPE}} = \sum_{j=s}^{k} \beta_\ell^{(j)} V_\ell^{(j)} \tag{3.47}$$

can be formulated with $k << O$. Here, instead of $V_\ell^{(0)}$, $V_\ell^{(s)}$ with $0 \leq s < k$ is used as the starting condition for the construction of the dominant eigenmode, for further reduction of the required number of iteration steps k. The initial vector $V_\ell^{(s)}$ is obtained by a cycling process which will be discussed at the end of this section. In order to find the weighting factors $\beta_\ell^{(j)}$ in Eq. (3.47) the vector

$$u_\ell^{(j)} = V_\ell^{(j+1)} \exp\left[\mathrm{i}\phi_\ell^{(j)}\right] - V_\ell^{(j)} \tag{3.48}$$

and the matrix

$$U_\ell^{(j)} = [u_\ell^{(s)}|u_\ell^{(s+1)}|...|u_\ell^{(j)}] \in \mathbb{C}^{O\times(j+1-s)} \tag{3.49}$$

are defined. The phase shift $\phi_\ell^{(j)}$ can be calculated via the argument:

$$\phi_\ell^{(j)} = \arg\left[\frac{\left(V_\ell^{(j)}, \alpha^{(j)} V_\ell^{(j+1)}\right)}{\left(V_\ell^{(j)}, V_\ell^{(j)}\right)}\right] \tag{3.50}$$

with the Euclidean inner product $(a, b) = a^* b$, where * denotes the complex conjugate. The least-square solution $c_\ell = (c_\ell^{(s)}, c_\ell^{(s+1)}, ...c_\ell^{(k-1)})^{\mathrm{T}}$ of the linear system

$$U_\ell^{(k-1)} c_\ell = -u_\ell^{(k)} \tag{3.51}$$

can be used to calculate the weighting factors [131]

$$\beta_\ell^{(j)} = \frac{c_\ell^{(j)}}{\sum_{i=s}^{k} c_\ell^{(i)}} \tag{3.52}$$

with $c_\ell^{(k)} = 1$. It is not recommended to solve the linear system of Eq. (3.51) directly using the normal equation, due to the numerical instability of the solver caused by ill-conditioned $U_\ell^{(k-1)}$ for increasing k [131]. A numerically fast, stable and storage-wise more economical algorithm has been given by Sidi [131,132] using the QR-factorization $U_\ell^{(j)} = Q_\ell^{(j)} R_\ell^{(j)}$ with

$$Q_\ell^{(j)} = [q_\ell^{(s)}|q_\ell^{(s+1)}|...|q_\ell^{(j)}] \in \mathbb{C}^{O\times(j+1-s)} \tag{3.53}$$

and the upper triangular matrix $R_\ell^{(j)} \in \mathbb{C}^{(j+1-s)\times(j+1-s)}$

$$R_\ell^{(j)} = \begin{pmatrix} r_\ell^{(s,s)} & r_\ell^{(s,s+1)} & \cdots & r_\ell^{(s,j)} \\ 0 & r_\ell^{(s+1,s+1)} & \cdots & r_\ell^{(s+1,j)} \\ 0 & 0 & \ddots & \vdots \\ 0 & 0 & 0 & r_\ell^{(j,j)} \end{pmatrix}. \tag{3.54}$$

Table 3.1 – Efficient algorithm for MPE.

```
Step 0: Perform the first $f$ round trips including normalizations by
        $\boldsymbol{V}^{(s+1)} = \prod_f \left(\frac{1}{\alpha^{(s)}}\boldsymbol{\mathcal{R}}\right) \boldsymbol{V}^{(s)}$.
        Calculate $u_\ell^{(s)}$ according to Eq. (3.48).
        Calculate $r_\ell^{(s,s)} = \left(u_\ell^{(s)}, u_\ell^{(s)}\right)^{(1/2)}$ and $q_\ell^{(s)} = u_\ell^{(s)}/r_\ell^{(s,s)}$.
Step 1: For $j = s+1, s+2, ..., k$ do
            Perform $f$ round trip calculations including
            normalizations by $\boldsymbol{V}^{(j+1)} = \prod_f \left(\frac{1}{\alpha^{(j)}}\boldsymbol{\mathcal{R}}\right) \boldsymbol{V}^{(j)}$.
            Calculate $u_\ell^{(j)}$ according to Eq. (3.48).
            Compute $U_\ell^{(j)} = Q_\ell^{(j)} R_\ell^{(j)}$ by:
            Set $u_{\ell,s}^{(j)} = u_\ell^{(j)}$.
            For $b = s, s+1, ...j-1$ do
                Compute $r_\ell^{(b,j)} = (q_\ell^{(b)}, u_{\ell,b}^{(j)})$ and $u_{\ell,b+1}^{(j)} = u_{\ell,b}^{(j)} - r_\ell^{(b,j)} q_\ell^{(b)}$.
            End for $b$.
            Compute $r_\ell^{(j,j)} = \left(u_{\ell,j}^{(j)}, u_{\ell,j}^{(j)}\right)^{(1/2)}$ and $q_\ell^{(j)} = u_{\ell,j}^{(j)}/r_\ell^{(j,j)}$.
        End for $j$.
Step 2: Solve the linear system $R_\ell^{(k-1)} c_\ell = -r_\ell^{(k)}$
        with $r_\ell^{(k)} = \left(r_\ell^{(s,k)}, r_\ell^{(s+1,k)}, ..., r_\ell^{(k-1,k)}\right)^{\mathrm{T}}$
        ending up with $c_\ell = (c_\ell^{(s)}, c_\ell^{(s+1)}, ...c_\ell^{(k-1)})^{\mathrm{T}}$.
Step 3: Set $c_\ell^{(k)} = 1$ and calculate $\beta_\ell^{(j)}$ according to Eq. (3.52)
Step 4: Calculate $\xi_\ell = \left(\xi_\ell^{(s)}, \xi_\ell^{(1)}, ..., \xi_\ell^{(k-1)}\right)^{\mathrm{T}}$
        by $\xi_\ell^{(s)} = 1 - \beta_\ell^{(s)}$; $\xi_\ell^{(j)} = \xi^{(j-1)} - \beta_\ell^{(j)}$
Step 5: Calculate $W_{\ell,s,k}^{\mathrm{MPE}} = V_\ell^{(s)} + Q_\ell^{(k-1)} \left(R_\ell^{(k-1)} \xi_\ell\right)$.
```

Sidi [131, 132] suggested the modified Gram-Schmidt process (MGS) for efficient QR-factorization. In this case the efficient MPE algorithm [131, 132], given in Table 3.1 is obtained, which was adapted for resonator analysis.

Reduced rank extrapolation (RRE)

A drawback of the MPE algorithm is that, for $k < k_0$ iterations, the solution $W_{\ell,s,k}^{\mathrm{MPE}}$ does not always exist. Here k_0 represents the critical minimum number of required resonator round trip calculations. Details about k_0 can be found in [131, 132]. This limitation can be overcome by using the RRE algorithm, which always provides a solution $W_{\ell,s,k}^{\mathrm{RRE}}$, for any number of used iterations k. From the algorithm point of view steps 2-5 of the above given MPE algorithm are replaced by the steps given in Table 3.2 to obtain the RRE algorithm [131, 132].

Table 3.2 – Replaced Steps 2-5 for efficient RRE algorithm.

Step 2:	Solve the linear system $R_\ell^{(k)*} R_\ell^{(k)} c_\ell = e$ with $e = (1, 1..., 1)^{\mathrm{T}}$ and * representing the conjugate transpose matrix ending up with $c_\ell = (c_\ell^{(s)}, c_\ell^{(s+1)}, ...c_\ell^{(k)})^{\mathrm{T}}$
Step 3:	Calculate $\beta_\ell^{(j)}$ according to Eq. (3.52)
Step 4:	Calculate $\xi_\ell = \left(\xi_\ell^{(s)}, \xi_\ell^{(1)}, ..., \xi_\ell^{(k-1)}\right)^{\mathrm{T}}$ by $\xi_\ell^{(s)} = 1 - \beta_\ell^{(s)}$; $\xi_\ell^{(j)} = \xi^{(j-1)} - \beta_\ell^{(j)}$
Step 5:	Calculate $W_{\ell,s,k}^{\mathrm{RRE}} = V_\ell^{(s)} + Q_\ell^{(k-1)} \left(R_\ell^{(k-1)} \xi_\ell\right)$

Compared to the MPE, the RRE algorithm has a slightly increased numerical effort, because of the need to solve two triangular (lower and upper) linear systems in Step 2 of the RRE, instead of one upper triangular linear system for the MPE. Please note that both of the above described algorithms have to be applied on each harmonic field component $\ell = 1, 2$ separately. The coupling between the different polarization components and all involved nonlinear processes inside the resonator can be covered by the round trip operator $\boldsymbol{\mathcal{R}}$.

Cycling and multi round trip calculation

From the point of view of data storage and computational effort, the size of $Q_\ell^{(k-1)} \in \mathbb{C}^{O\times(k-s)}$ is most significant. Its size scales linearly with the number of required round trips $k-s$, independent of whether MPE or RRE is used. Therefore the total number of required round trips can be reduced by using the cycling method [131, 132]. Here the calculation of $W_{\ell,s,k}^{\mathrm{MPE}}$ or $W_{\ell,s,k}^{\mathrm{RRE}}$ is iteratively repeated by using the above given algorithms. Once the result $W_{\ell,s,k}^{\mathrm{RRE/MPE}}$ is obtained it is used as a new starting condition $V_\ell^{(s)} = W_{\ell,s,k}^{\mathrm{RRE/MPE}}$ for the next MPE or RRE cycle. The first cycle starts with $V_\ell^{(s)} = V_\ell^{(0)}$, which is typically a random phase distribution, to ensure that the starting field $V_\ell^{(0)} \in \boldsymbol{\mathcal{H}}$ does not entirely lie in $\boldsymbol{\mathcal{M}}^\perp$.

If $f = 1$, the term $\boldsymbol{V}^{(j+1)} = \prod_f \left(\frac{1}{\alpha^{(j)}}\boldsymbol{\mathcal{R}}\right) \boldsymbol{V}^{(j)}$ in the steps 0 and 1 of the MPE and RRE algorithms is simplified to the application of a single round trip calculation per iteration j given by Eq. (3.38). Furthermore the size of $Q_\ell^{(k-1)}$ and so the amount of storage can be decreased by increasing f and thus performing f round trip operations and normalization steps α per iteration j [131,132]. Thus in the following the case $f = 1$ is called single round trip MPE or RRE algorithm, whereas the case $f > 1$ is called multi round trip MPE or RRE algorithm.

Please note that the solution of Eq. (3.12) for nonlinear round trip operators is only unique for the case that a single dominant transversal resonator mode exists for the laser resonator setup. For multi-transversal-mode operation there is mode competition, which is not included in the resonator round trip formulation of Eq. (3.12). Thus in the case of mode competition caused by strong nonlinear gain the RRE or MPE algorithm as well as the iterative power method might converge to a solution which does not represent one of the actual resonator modes oscillating in the cavity. However please note that this fact is not caused by any shortcomings of the MPE or RRE algorithm, but simply a restriction of the problem formulation. A detailed discussion about the stability of single mode laser oscillation can be found in [105]. As shown in the outlook of this work (chapter 6) it is also possible to extend the problem formulation of Eq. (3.12) in a way that it also leads to unique solutions for multi-transversal-mode operations. A similar extension has been done [106, 107] for the scalar Fox and Li algorithm. Nevertheless this extension is beyond the scope of the major parts of this thesis.

Chapter 4

Simulation Concepts for Light Propagation in Laser Crystals

Up to now it was shown that the light propagation through different intracavity optical components is simulated by component operators $\boldsymbol{\mathcal{C}}$. These component operators are matrix operators which have either a diagonal or a non-diagonal matrix structure depending on whether polarization cross-talk effects are present or not. For the simulation of solid-state laser resonators it is of particular interest to model the light propagation through anisotropic crystals. These crystals are either used for polarization control of the light inside the cavity (e.g. Glan-Taylor prism polarizer [133], Quartz polarization rotator [20]) or for light amplification. Crystals which are typically used for polarization control have a homogeneous but anisotropic refractive index. Therefore in section 4.1 a rigorous non-diagonal component operator for the simulation of light propagation through linear, homogeneous and anisotropic media is introduced. Besides birefringence effects, this technique includes intra-crystal diffraction and interface refraction at crystal surfaces. Please note that the concepts given in section 4.1 were developed and published [134] together with my colleague Mr. Site Zhang.

Doped crystals which are used for light amplification inside the laser resonator are optically anisotropic due to natural [135,136] or stress-induced birefringence [17,137]. Furthermore these active crystals are typically optically inhomogeneous due to an inhomogeneous temperature distribution within the laser crystal. This temperature distribution causes, besides stress-induced birefringence, a deformation of the transversal resonator mode due to thermal lensing [15, 138]. Thus in section 4.2 a vectorial beam propagation method (vBPM) is introduced for the numerically efficient propagation of light through active media. In addition to the modeling of thermal lensing and birefringence, this non-diagonal vBPM component operator includes the calculation of light amplification and nonlinear gain saturation [139, 140].

4.1 Simulation of Crystals with Natural-Birefringence

In the literature there are a plenty of different simulation techniques available describing the light propagation through linear, homogeneous and anisotropic media. However all of these techniques are limited in their applicability, because they require certain types of incident fields [141–146] (typically plane waves or Gaussian beams), uniaxial anisotropy [147–151] and/or crystal orientations [152, 153] where the crystal optic axis must be parallel to the propagation direction of incident light.

In the following an angular spectrum of plane waves approach is introduced for propagating general monochromatic electromagnetic fields through arbitrarily oriented bi- and uniaxial anisotropic crystals. Please note that the following component operator is a generalization of the work carried out by Landry and Maldonado [154]. In [154] only the interaction of a single plane wave at a single plane interface between two anisotropic or one anisotropic and one isotropic media was discussed. In the following this method is extended to general incident fields, by combining their method with the angular spectrum of plane waves. The expressions in [154] are formulated in the plane of incidence, where it is possible to obtain a y-invariant case. All formulations are done in a general coordinate system, which is needed to deal with general incident beams. Furthermore it is shown that this angular spectrum of plane waves representation of light is very suitable to rigorously propagate the light further through linear and homogeneous crystals. Fig. 4.1 illustrates the task of the component operator $\boldsymbol{\mathcal{C}}_{\text{aniso}}$ for light propagation through a linear, homogeneous and anisotropic medium. Applied on the incident field $\boldsymbol{V}^{\text{in}}(\boldsymbol{r} \in \Gamma^{\text{in}})$ given on the plane boundary Γ^{in} in front of the front crystal surface the operator should calculate the harmonic field components $\boldsymbol{V}^{\text{out}}(\boldsymbol{r} \in \Gamma^{\text{out}})$ directly on the plane boundary Γ^{out} behind the rear crystal surface. Please note that inside the anisotropic medium it is more convenient to propagate not just the two electric field components E_x and E_y, but the three-dimensional field vector $(E_x, E_y, E_z)^{\text{T}}$, by using the following approach. However according to the definition that a subdomain is embedded between linear, isotropic and homogeneous media, the light is entering the anisotropic subdomain from the isotropic medium and is leaving the crystal into an isotropic medium, it is mathematically sufficient to formulate a unique input-output problem by

$$\begin{pmatrix} V_1^{\text{out}} \\ V_2^{\text{out}} \end{pmatrix} = \boldsymbol{\mathcal{C}}_{\text{aniso}} \begin{pmatrix} V_1^{\text{in}} \\ V_2^{\text{in}} \end{pmatrix} , \tag{4.1}$$

with $\boldsymbol{\mathcal{C}}_{\text{aniso}}$ being the 2×2 component operator matrix. In the calculation also the refraction effects at both crystal interfaces should be taken into account. Therefore the isotropic media in front of and behind the anisotropic crystal are described by the dielectric constants ϵ^{i} and ϵ^{t} respectively. In a sequential way the component operator has to deal with 1) refraction at the front surface, 2) field propagation inside the anisotropic medium and 3) refraction at the rear surface. The component operator for anisotropic media is mainly

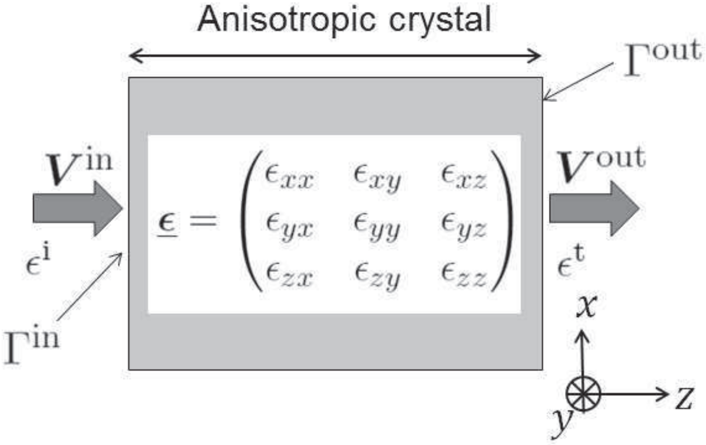

Figure 4.1 – Illustration of the simulation task for propagating light through an arbitrarily oriented anisotropic medium with dielectric tensor $\underline{\boldsymbol{\epsilon}}$. The anisotropic medium is embedded between two isotropic media with dielectric constants ϵ^{i} and ϵ^{t} respectively. Therefore for the unique representation of the incident field $V_\ell^{\mathrm{in}}(\boldsymbol{\rho}, z_{\mathrm{in}})$ and the transmitted field $V_\ell^{\mathrm{out}}(\boldsymbol{\rho}, z_{\mathrm{out}})$, only two field components $\ell = 1, 2$ are necessary.

based on the idea, that any incident field $V_\ell^{\mathrm{in}}(\boldsymbol{\rho}, z_{\mathrm{in}})$ in the isotropic medium ϵ^{i} can be decomposed by a Fourier Transformation ($\mathscr{F}$) into a set of plane waves using the angular spectrum of plane waves approach

$$A_\ell^{\mathrm{i}}(\boldsymbol{\kappa}) = \mathscr{F}\{V_\ell^{\mathrm{in}}(\boldsymbol{\rho}, z_{\mathrm{in}})\} = \frac{1}{2\pi} \iint_{-\infty}^{+\infty} V_\ell^{\mathrm{in}}(\boldsymbol{\rho}, z_{\mathrm{in}}) \exp(-\mathrm{i}\boldsymbol{\kappa} \cdot \boldsymbol{\rho}) \mathrm{d}x \mathrm{d}y \,, \tag{4.2}$$

where $A_\ell^{\mathrm{i}}(\boldsymbol{\kappa})$ denotes the angular spectrum of $V_\ell^{\mathrm{in}}(\boldsymbol{\rho}, z_{\mathrm{in}})$ with $\ell = 1, 2$. The inverse FT

$$V_\ell^{\mathrm{in}}(\boldsymbol{\rho}, z_{\mathrm{in}}) = \mathscr{F}^{-1}\{A_\ell^{\mathrm{i}}(\boldsymbol{\kappa})\} = \frac{1}{2\pi} \iint_{-\infty}^{+\infty} A_\ell^{\mathrm{i}}(\boldsymbol{\kappa}) \exp(\mathrm{i}\boldsymbol{\kappa} \cdot \boldsymbol{\rho}) \mathrm{d}k_x \mathrm{d}k_y \tag{4.3}$$

shows that a general incident field in the isotropic medium can be treated as a superposition of plane waves. Each plane wave is completely determined by its direction $\boldsymbol{\kappa} = (k_x, k_y)^{\mathrm{T}}$ and its amplitude $[A_1^{\mathrm{i}}(\boldsymbol{\kappa}), A_2^{\mathrm{i}}(\boldsymbol{\kappa})]^{\mathrm{T}}$. After this plane wave decomposition, each plane wave is propagated separately through the linear, anisotropic medium. Behind the anisotropic medium all propagated plane waves are superimposed in the rear space filled with the isotropic medium ϵ^{t}. Therefore an inverse FT can be used to get the desired solution:

$$V_\ell^{\mathrm{out}}(\boldsymbol{\rho}, z_{\mathrm{out}}) = \mathscr{F}^{-1}\{A_\ell^{\mathrm{t}}(\boldsymbol{\kappa})\} = \frac{1}{2\pi} \iint_{-\infty}^{+\infty} A_\ell^{\mathrm{t}}(\boldsymbol{\kappa}) \exp(\mathrm{i}\boldsymbol{\kappa} \cdot \boldsymbol{\rho}) \mathrm{d}k_x \mathrm{d}k_y \,. \tag{4.4}$$

Consequently to solve Eq. (4.4) the propagated angular spectrum $A_\ell^{\mathrm{t}}(\boldsymbol{\kappa})$ has to be known. Therefore in the following subsections the light refraction and propagation of the plane waves through the homogeneous, anisotropic media will be discussed to construct $A_\ell^{\mathrm{t}}(\boldsymbol{\kappa})$. In what follows the field components $[A_1^{\mathrm{i}}(\boldsymbol{\kappa}), A_2^{\mathrm{i}}(\boldsymbol{\kappa})]^{\mathrm{T}}$ of each plane wave with the direction

$\boldsymbol{\kappa}$ will be denoted as $(\mathcal{E}_x^{\mathrm{i}}, \mathcal{E}_y^{\mathrm{i}})^{\mathrm{T}}$ to keep their physical meaning in mind. For better readability the variable $\boldsymbol{\kappa}$ is skipped in the following.

Plane wave refraction at a plane interface from ϵ^{i} into $\underline{\boldsymbol{\epsilon}}$

A plane wave component from the incident field can be extracted in Eq. (4.2) and expressed in its vectorial form by

$$\boldsymbol{E}^{\mathrm{i}}(\boldsymbol{r}) = \boldsymbol{\mathcal{E}}^{\mathrm{i}} \exp(\mathrm{i}\boldsymbol{k}^{\mathrm{i}} \cdot \boldsymbol{r}) \,, \tag{4.5}$$

with $\boldsymbol{\mathcal{E}}^{\mathrm{i}} = (\mathcal{E}_x^{\mathrm{i}}, \mathcal{E}_y^{\mathrm{i}}, \mathcal{E}_z^{\mathrm{i}})^{\mathrm{T}}$ and $\boldsymbol{k}^{\mathrm{i}} = (k_x^{\mathrm{i}}, k_y^{\mathrm{i}}, k_z^{\mathrm{i}})^{\mathrm{T}}$. The z-component of $\boldsymbol{k}^{\mathrm{i}}$ and $\boldsymbol{\mathcal{E}}^{\mathrm{i}}$ can be obtained from $\boldsymbol{\kappa}^{\mathrm{i}} = (k_x^{\mathrm{i}}, k_y^{\mathrm{i}})^{\mathrm{T}}$ and $(\mathcal{E}_x^{\mathrm{i}}, \mathcal{E}_y^{\mathrm{i}})^{\mathrm{T}}$ by using the following relations

$$k_z^{\mathrm{i}} = \left[\epsilon^{\mathrm{i}} k_0^2 - {k_x^{\mathrm{i}}}^2 - {k_y^{\mathrm{i}}}^2\right]^{1/2} , \tag{4.6}$$

$$\mathcal{E}_z^{\mathrm{i}} = -\frac{k_x^{\mathrm{i}}\mathcal{E}_x^{\mathrm{i}} + k_y^{\mathrm{i}}\mathcal{E}_y^{\mathrm{i}}}{k_z^{\mathrm{i}}}, \tag{4.7}$$

with $k_0 = \omega_0/c$ as the wave number in vacuum. As discussed in [154], on the plane interface between isotropic and anisotropic media, an incident plane wave causes one reflected plane wave which has the form

$$\boldsymbol{E}^{\mathrm{r}}(\boldsymbol{r}) = \boldsymbol{\mathcal{E}}^{\mathrm{r}} \exp(\mathrm{i}\boldsymbol{k}^{\mathrm{r}} \cdot \boldsymbol{r}) \tag{4.8}$$

and two transmitted plane waves which can be written as

$$\boldsymbol{E}^{\mathrm{t}}(\boldsymbol{r}) = \alpha^{\mathrm{t}} \hat{\boldsymbol{\mathcal{E}}}_\alpha^{\mathrm{t}} \exp(\mathrm{i}\boldsymbol{k}_\alpha^{\mathrm{t}} \cdot \boldsymbol{r}) + \beta^{\mathrm{t}} \hat{\boldsymbol{\mathcal{E}}}_\beta^{\mathrm{t}} \exp(\mathrm{i}\boldsymbol{k}_\beta^{\mathrm{t}} \cdot \boldsymbol{r}) \,. \tag{4.9}$$

For a plane wave with a given wavevector in an anisotropic medium, its electric field vector direction is uniquely determined. As a consequence in Eq. (4.9), the complex electric field vector must be expressed as $\alpha^{\mathrm{t}}\hat{\boldsymbol{\mathcal{E}}}_\alpha^{\mathrm{t}}$, the product of magnitude α^{t} and normalized electric field eigenvector $\hat{\boldsymbol{\mathcal{E}}}_\alpha^{\mathrm{t}}$, and the same for $\beta^{\mathrm{t}}\hat{\boldsymbol{\mathcal{E}}}_\beta^{\mathrm{t}}$. In Eq. (4.8) and Eq. (4.9), the wavevectors $\boldsymbol{k}^{\mathrm{r}}$, $\boldsymbol{k}_\alpha^{\mathrm{t}}$ and $\boldsymbol{k}_\beta^{\mathrm{t}}$, as well as the electric field vectors $\boldsymbol{\mathcal{E}}^{\mathrm{r}}$, $\alpha^{\mathrm{t}}\hat{\boldsymbol{\mathcal{E}}}_\alpha^{\mathrm{t}}$ and $\beta^{\mathrm{t}}\hat{\boldsymbol{\mathcal{E}}}_\beta^{\mathrm{t}}$ are unknown. This unknown quantities can be calculated by the following sequence:

- **Step I** – determine the unknown wavevectors $\boldsymbol{k}^{\mathrm{r}}$, $\boldsymbol{k}_\alpha^{\mathrm{t}}$ and $\boldsymbol{k}_\beta^{\mathrm{t}}$ by using phase matching conditions at the plane interface;

- **Step II** – find out the electric field eigenvectors $\hat{\boldsymbol{\mathcal{E}}}_\alpha^{\mathrm{t}}$ and $\hat{\boldsymbol{\mathcal{E}}}_\beta^{\mathrm{t}}$ by solving the coupled wave equations in the form of an eigenvalue problem;

- **Step III** – apply boundary conditions to obtain the reflected electric field vector $\boldsymbol{\mathcal{E}}^{\mathrm{r}}$ as well as the magnitudes α^{t} and β^{t} of the transmitted plane waves.

The corresponding algorithm is summarized in Fig. 4.2, as an overview of the calculation process, while the discussion in detail follows afterward.

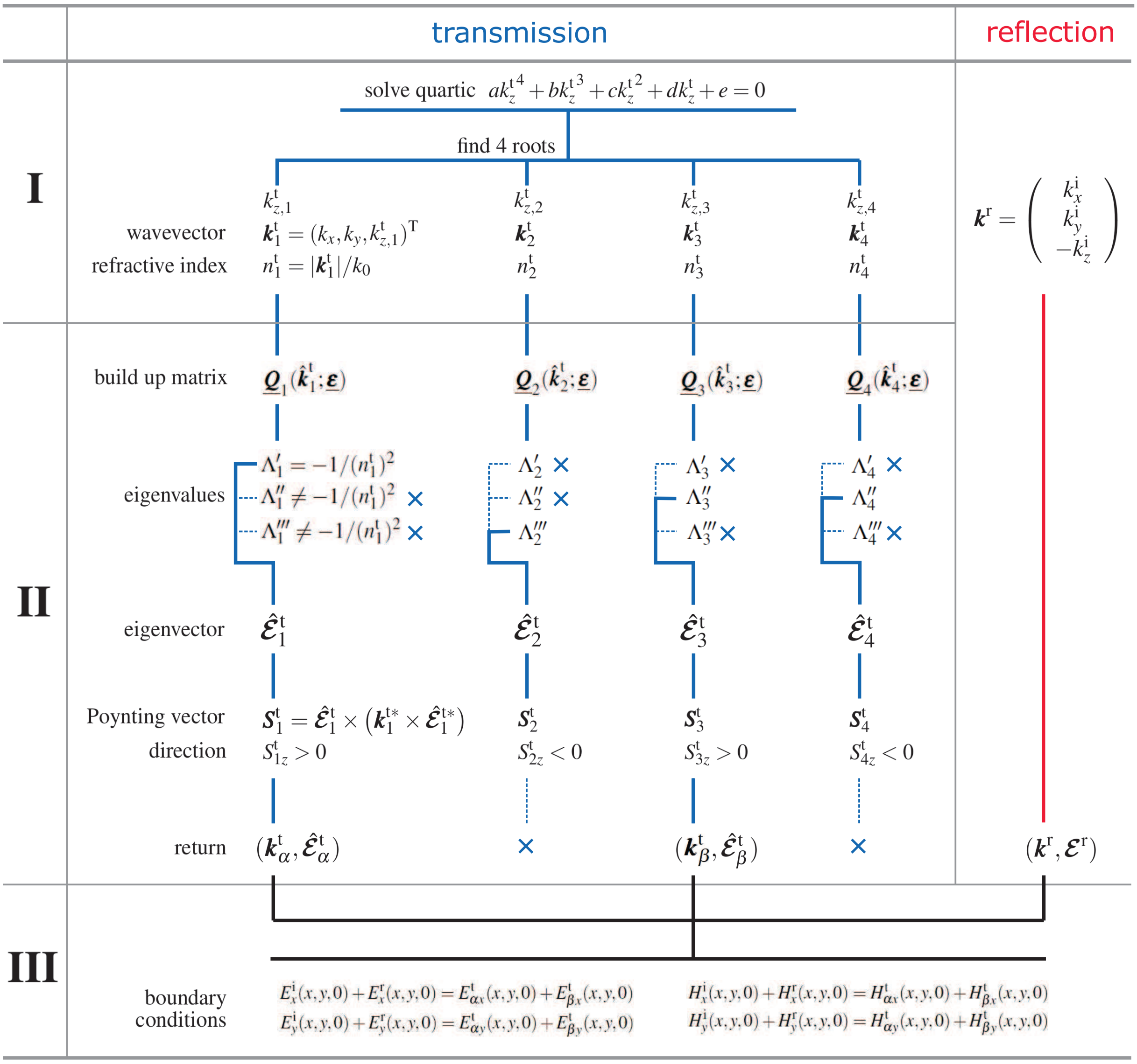

Figure 4.2 – Example workflow to solve the refraction problem at a plane interface from ϵ^i into $\underline{\boldsymbol{\epsilon}}$. The explicit process of **Step II** is shown. For example, with root $k^t_{z,1}$ from the quartic equation, a wavevector $\boldsymbol{k}^t_1$ and a refractive index n^t_1 is determined. Using $\boldsymbol{k}^t_1$ and $\underline{\boldsymbol{\epsilon}}$, a 3×3 matrix $\underline{\boldsymbol{Q}}_1$ is built up and three eigenvalues Λ'_1, Λ''_1 and Λ'''_1 are found. Amongst them only $\Lambda'_1=-1/(n^t_1)^2$ while the other two cases are terminated. The termination is denoted by the × symbol. Using the eigenvector $\hat{\boldsymbol{\mathcal{E}}}^t_1$ for Λ'_1, the time-averaged Poynting vector $\boldsymbol{S}^t_1$ is calculated. Because of $S^t_{1z}>0$ and $S^t_{3z}>0$, the two solution pairs $\boldsymbol{k}^t_\alpha:=\boldsymbol{k}^t_1$ and $\hat{\boldsymbol{\mathcal{E}}}^t_\alpha:=\hat{\boldsymbol{\mathcal{E}}}^t_1$ as well as $\boldsymbol{k}^t_\beta:=\boldsymbol{k}^t_3$ and $\hat{\boldsymbol{\mathcal{E}}}^t_\beta:=\hat{\boldsymbol{\mathcal{E}}}^t_3$ are returned. Otherwise this process is terminated, as shown for $\boldsymbol{S}^t_2$ and $\boldsymbol{S}^t_4$.

Calculation of unknown wavevectors (Step I)

To calculate the unknown wavevectors, the phase matching condition is used. Consequently the transverse components of the wavevectors $\boldsymbol{\kappa}$ on both sides of the interface must be equal, as is illustrated in Fig. 4.3. Therefore there is

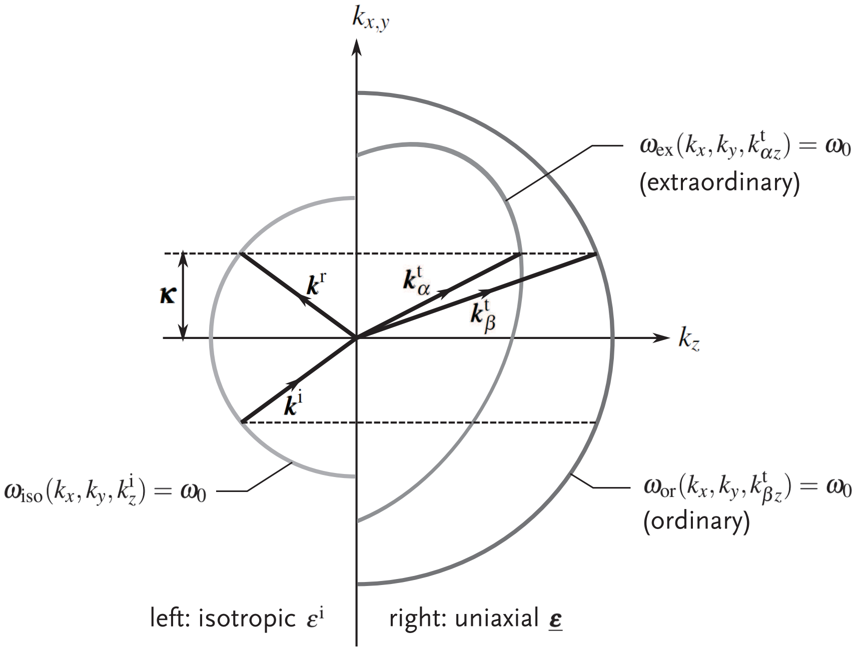

Figure 4.3 – Refraction at a plane interface between an isotropic medium (left) and an arbitrarily oriented uniaxial crystal (right). The dispersion relation of the isotropic medium appears as a semi-sphere on the left side; for the uniaxial crystal on the right side, its dispersion relations are presented as two surfaces, a partial ellipsoid for the extraordinary wave and a semi-sphere for the ordinary waves. Due to the phase matching condition at the interface, the transverse components $\boldsymbol{\kappa}$ of the wavevector $\boldsymbol{k}$ must be equal for the incident and the three resulting plane waves.

$$\boldsymbol{\kappa}^{\mathrm{i}} = \boldsymbol{\kappa}^{\mathrm{r}} = \boldsymbol{\kappa}^{\mathrm{t}} = (k_x, k_y)^{\mathrm{T}} \tag{4.10}$$

and only the z-components of the reflected and transmitted wavevectors need to be calculated. For the reflected plane wave there is $k_z^{\mathrm{r}} = -k_z^{\mathrm{i}}$ and for the transmitted plane waves, a quartic equation [155, 156], sometimes referred to as the Booker quartic [154], can be found in the form

$$a{k_z^{\mathrm{t}}}^4 + b{k_z^{\mathrm{t}}}^3 + c{k_z^{\mathrm{t}}}^2 + dk_z^{\mathrm{t}} + e = 0\,, \tag{4.11}$$

where a, b, c, d and e are coefficients dependent on k_x, k_y and $\underline{\boldsymbol{\epsilon}}$. Explicitly these coefficients are

$$\begin{aligned}
a =&\epsilon_{zz}\,,\\
b =&2(\epsilon_{xz}k_x + \epsilon_{yz}k_y)\,,\\
c =&(\epsilon_{xx}+\epsilon_{zz})k_x^2 + (\epsilon_{yy}+\epsilon_{zz})k_y^2 + k_0^2\left[\epsilon_{xz}^2 + \epsilon_{yz}^2 - \epsilon_{zz}(\epsilon_{xx}+\epsilon_{yy})\right]\,,\\
d =&2\left[\epsilon_{xz}k_x^3 + \epsilon_{yz}k_y^3 + \epsilon_{xz}k_xk_y^2 + \epsilon_{yz}k_x^2k_y + k_0^2k_x(\epsilon_{xy}\epsilon_{yz} - \epsilon_{xz}\epsilon_{yy}) + k_0^2k_y(\epsilon_{xy}\epsilon_{xz} - \epsilon_{xx}\epsilon_{yz})\right]\,,\\
e =&k_0^4(\epsilon_{xx}\epsilon_{yy}\epsilon_{zz} + 2\epsilon_{xz}\epsilon_{xy}\epsilon_{yz} - \epsilon_{xx}\epsilon_{yz}^2 - \epsilon_{yy}\epsilon_{xz}^2 - \epsilon_{zz}\epsilon_{xy}^2) + 2k_0^2k_xk_y(\epsilon_{xz}\epsilon_{yz} - \epsilon_{xy}\epsilon_{zz})\\
&+ k_0^2k_x^2(\epsilon_{xz}^2 - \epsilon_{xx}\epsilon_{zz} - \epsilon_{xx}\epsilon_{yy} + \epsilon_{xy}^2) + k_0^2k_y^2(\epsilon_{yz}^2 - \epsilon_{yy}\epsilon_{zz} - \epsilon_{xx}\epsilon_{yy} + \epsilon_{xy}^2)\\
&+ k_x^2k_y^2(\epsilon_{xx}+\epsilon_{yy}) + 2k_xk_y(k_x^2+k_y^2)\epsilon_{xy} + k_x^4\epsilon_{xx} + k_y^4\epsilon_{yy}\,.
\end{aligned} \tag{4.12}$$

Solving Eq. (4.11) in general yields four solutions $k_{z,j}^{\mathrm{t}}$ with $j = 1,2,3,4$. Consequently there are four wavevectors $\boldsymbol{k}_j^{\mathrm{t}} = (k_x, k_y, k_{z,j}^{\mathrm{t}})^{\mathrm{T}}$ and four refractive indices $n_j^{\mathrm{t}} = |\boldsymbol{k}_j^{\mathrm{t}}|/k_0$. As Yeh argued in [155], only two of the four wavevectors correspond to energy transmission into $+z$ direction. To pick them out, the time-averaged Poynting vector $\boldsymbol{S}_j^{\mathrm{t}}$ associated with a wavevector $\boldsymbol{k}_j^{\mathrm{t}}$ has to be known. For the calculation of $\boldsymbol{S}_j^{\mathrm{t}}$ the associated electric field vector needs to be calculated first.

Determination of electric field eigenvectors (Step II)

Following the treatment in [156] and using the plane wave ansatz $\boldsymbol{E}_j^{\mathrm{t}}(\boldsymbol{r}) = \boldsymbol{\mathcal{E}}_j^{\mathrm{t}}\exp(\mathrm{i}\boldsymbol{k}_j^{\mathrm{t}}\cdot\boldsymbol{r})$, the waveequations in a homogeneous anisotropic medium with the dielectric tensor $\underline{\boldsymbol{\epsilon}}$ can be formulated as an eigenvalue problem

$$\underline{\boldsymbol{Q}}_j\boldsymbol{\mathcal{E}}_j^{\mathrm{t}} = \Lambda_j\boldsymbol{\mathcal{E}}_j^{\mathrm{t}} \quad \text{and} \quad \Lambda_j \overset{!}{=} -\frac{1}{(n_j^{\mathrm{t}})^2}\,, \tag{4.13}$$

where

$$\underline{\boldsymbol{Q}}_j = \underline{\boldsymbol{\epsilon}}^{-1}\begin{pmatrix} -\hat{k}_y^2 - (\hat{k}_{z,j}^{\mathrm{t}})^2 & \hat{k}_x\hat{k}_y & \hat{k}_x\hat{k}_{z,j}^{\mathrm{t}} \\ \hat{k}_x\hat{k}_y & -\hat{k}_x^2 - (\hat{k}_{z,j}^{\mathrm{t}})^2 & \hat{k}_y\hat{k}_{z,j}^{\mathrm{t}} \\ \hat{k}_x\hat{k}_{z,j}^{\mathrm{t}} & \hat{k}_y\hat{k}_{z,j}^{\mathrm{t}} & -\hat{k}_x^2 - \hat{k}_y^2 \end{pmatrix} \tag{4.14}$$

and the normalized wavevector defined as $(\hat{k}_x, \hat{k}_y, \hat{k}_{z,j}^{\mathrm{t}})^{\mathrm{T}} = \hat{\boldsymbol{k}}_j^{\mathrm{t}} = \boldsymbol{k}_j^{\mathrm{t}}/|\boldsymbol{k}_j^{\mathrm{t}}|$. Please note that the four values of $\boldsymbol{k}_j^{\mathrm{t}}$ were previously calculated in **Step I** by solving Eq. (4.11). According to Eq. (4.13), $\boldsymbol{\mathcal{E}}_j^{\mathrm{t}}$ is an eigenvector of matrix $\underline{\boldsymbol{Q}}_j$ corresponding to the eigenvalue $-1/(n_j^{\mathrm{t}})^2$. Thus standard numerical eigenvalue solvers (as they are implemented e.g. in [157]) can be used for solving the eigenvalue problem given by Eq. (4.13). The resulting eigenvectors are normalized to $\hat{\boldsymbol{\mathcal{E}}}_j^{\mathrm{t}} = \boldsymbol{\mathcal{E}}_j^{\mathrm{t}}/|\boldsymbol{\mathcal{E}}_j^{\mathrm{t}}|$ as defined in Eq. (4.9). The resulting eigenvalues of the 3×3 matrix $\underline{\boldsymbol{Q}}_j$ are Λ_j', Λ_j'' and Λ_j'''. One of them equals zero and is therefore non-physical, while the other two non-zero values correspond to the two refractive indices of the crystal for the direction $\hat{\boldsymbol{k}}_j^{\mathrm{t}}$.

Then the time-averaged Poynting vector can be calculated by

$$\boldsymbol{S}_j^{\mathrm{t}} \sim \hat{\boldsymbol{\mathcal{E}}}_j^{\mathrm{t}} \times (\boldsymbol{k}_j^{\mathrm{t}*} \times \hat{\boldsymbol{\mathcal{E}}}_j^{\mathrm{t}*})\,, \tag{4.15}$$

where * represents the complex conjugate. It turns out that only two of the four plane waves have positive S_{jz}^{t} components. The two positive values can be now defined in Eq. (4.9) as $\boldsymbol{k}_\alpha^{\mathrm{t}}$ and $\hat{\boldsymbol{\mathcal{E}}}_\alpha^{\mathrm{t}}$, and $\boldsymbol{k}_\beta^{\mathrm{t}}$ and $\hat{\boldsymbol{\mathcal{E}}}_\beta^{\mathrm{t}}$ respectively. Please note that in Eq. (4.9) α^{t} and β^{t} still are unknown, as well as $\boldsymbol{\mathcal{E}}^{\mathrm{r}}$ in Eq. (4.8).

Application of boundary conditions (Step III)

In the last step the boundary conditions

$$\begin{aligned}
E_x^{\mathrm{i}}(x,y,0) + E_x^{\mathrm{r}}(x,y,0) &= E_{\alpha x}^{\mathrm{t}}(x,y,0) + E_{\beta x}^{\mathrm{t}}(x,y,0)\,,\\
E_y^{\mathrm{i}}(x,y,0) + E_y^{\mathrm{r}}(x,y,0) &= E_{\alpha y}^{\mathrm{t}}(x,y,0) + E_{\beta y}^{\mathrm{t}}(x,y,0)\,,\\
H_x^{\mathrm{i}}(x,y,0) + H_x^{\mathrm{r}}(x,y,0) &= H_{\alpha x}^{\mathrm{t}}(x,y,0) + H_{\beta x}^{\mathrm{t}}(x,y,0)\,,\\
H_y^{\mathrm{i}}(x,y,0) + H_y^{\mathrm{r}}(x,y,0) &= H_{\alpha y}^{\mathrm{t}}(x,y,0) + H_{\beta y}^{\mathrm{t}}(x,y,0)\,,
\end{aligned} \tag{4.16}$$

are to be applied at the interface where $z = 0$. For a plane wave, its magnetic field is related to the electric field via the following relation [30]

$$\boldsymbol{H}(\boldsymbol{r}) = \frac{1}{\omega\mu_0}\boldsymbol{k} \times \boldsymbol{E}(\boldsymbol{r})\,, \tag{4.17}$$

and finally Eq. (4.16) can be written in the matrix form

$$\underline{\boldsymbol{M}}\begin{pmatrix} \mathcal{E}_x^{\mathrm{r}} \\ \mathcal{E}_y^{\mathrm{r}} \\ \alpha^{\mathrm{t}} \\ \beta^{\mathrm{t}} \end{pmatrix} = \begin{pmatrix} \mathcal{E}_y^{\mathrm{i}} \\ \mathcal{E}_x^{\mathrm{i}} \\ \left(k_z^{\mathrm{i}} + \frac{k_x^2}{k_z^{\mathrm{i}}}\right)\mathcal{E}_x^{\mathrm{i}} + \frac{k_x k_y}{k_z^{\mathrm{i}}}\mathcal{E}_y^{\mathrm{i}} \\ \frac{k_x k_y}{k_z^{\mathrm{i}}}\mathcal{E}_x^{\mathrm{i}} + \left(k_z^{\mathrm{i}} + \frac{k_y^2}{k_z^{\mathrm{i}}}\right)\mathcal{E}_y^{\mathrm{i}} \end{pmatrix}, \tag{4.18}$$

with

$$\underline{\boldsymbol{M}} = \begin{pmatrix} 0 & -1 & \hat{\mathcal{E}}_{\alpha y}^{\mathrm{t}} & \hat{\mathcal{E}}_{\beta y}^{\mathrm{t}} \\ -1 & 0 & \hat{\mathcal{E}}_{\alpha x}^{\mathrm{t}} & \hat{\mathcal{E}}_{\beta x}^{\mathrm{t}} \\ k_z^{\mathrm{i}} + \frac{k_x^2}{k_z^{\mathrm{i}}} & \frac{k_x k_y}{k_z^{\mathrm{i}}} & k_{\alpha z}^{\mathrm{t}}\hat{\mathcal{E}}_{\alpha x}^{\mathrm{t}} - k_x\hat{\mathcal{E}}_{\alpha z}^{\mathrm{t}} & k_{\beta z}^{\mathrm{t}}\hat{\mathcal{E}}_{\beta x}^{\mathrm{t}} - k_x\hat{\mathcal{E}}_{\beta z}^{\mathrm{t}} \\ \frac{k_x k_y}{k_z^{\mathrm{i}}} & k_z^{\mathrm{i}} + \frac{k_y^2}{k_z^{\mathrm{i}}} & k_{\alpha z}^{\mathrm{t}}\hat{\mathcal{E}}_{\alpha y}^{\mathrm{t}} - k_y\hat{\mathcal{E}}_{\alpha z}^{\mathrm{t}} & k_{\beta z}^{\mathrm{t}}\hat{\mathcal{E}}_{\beta y}^{\mathrm{t}} - k_y\hat{\mathcal{E}}_{\beta z}^{\mathrm{t}} \end{pmatrix}. \tag{4.19}$$

Multiplying the inverse matrix $\underline{\boldsymbol{M}}^{-1}$ on both sides of Eq. (4.18) leads to

$$\begin{pmatrix} \mathcal{E}_x^{\mathrm{r}} \\ \mathcal{E}_y^{\mathrm{r}} \\ \alpha^{\mathrm{t}} \\ \beta^{\mathrm{t}} \end{pmatrix} = \underline{\boldsymbol{M}}^{-1} \begin{pmatrix} \mathcal{E}_y^{\mathrm{i}} \\ \mathcal{E}_x^{\mathrm{i}} \\ \left(k_z^{\mathrm{i}} + \frac{k_x^2}{k_z^{\mathrm{i}}} \mathcal{E}_x^{\mathrm{i}}\right) + \frac{k_x k_y}{k_z^{\mathrm{i}}} \mathcal{E}_y^{\mathrm{i}} \\ \frac{k_x k_y}{k_z^{\mathrm{i}}} \mathcal{E}_x^{\mathrm{i}} + \left(k_z^{\mathrm{i}} + \frac{k_y^2}{k_z^{\mathrm{i}}}\right) \mathcal{E}_y^{\mathrm{i}} \end{pmatrix} . \tag{4.20}$$

Now the unknown quantities $\mathcal{E}_x^{\mathrm{r}}$, $\mathcal{E}_y^{\mathrm{r}}$, α^{t} and β^{t} in Eq. (4.8) and Eq. (4.9) can be determined, since the right-hand side of Eq. (4.20) is known. In Eq. (4.19) $\underline{\boldsymbol{M}}$ is a non-diagonal matrix, and consequently its inverse $\underline{\boldsymbol{M}}^{-1}$ is also non-diagonal. Therefore polarization crosstalk between different electric field components may happen. As a result, the component operator $\boldsymbol{\mathcal{C}}_{\mathrm{aniso}}$ in Eq. (4.1) has a non-diagonal matrix structure.

Plane wave propagation inside anisotropic media

The propagation of a plane wave inside the anisotropic medium is completely governed by Eq. (4.9). Once the electric field vectors $\boldsymbol{\mathcal{E}}_\alpha^{\mathrm{t}} = \alpha^{\mathrm{t}} \hat{\boldsymbol{\mathcal{E}}}_\alpha^{\mathrm{t}}$ and $\boldsymbol{\mathcal{E}}_\beta^{\mathrm{t}} = \beta^{\mathrm{t}} \hat{\boldsymbol{\mathcal{E}}}_\beta^{\mathrm{t}}$ are known, the plane waves can be calculated at arbitrary positions inside the anisotropic medium. For a propagation over a distance $d = z_{\mathrm{out}} - z_{\mathrm{in}}$, $z = d$ is substituted in Eq. (4.9). By applying it to all the plane wave components, the angular spectrum of plane waves (SPW) operator in the anisotropic medium can be obtained

$$\begin{aligned} \boldsymbol{E}^{\mathrm{t}}(\boldsymbol{\rho}, d) &= \mathrm{FT}^{-1} \left\{ \boldsymbol{\mathcal{E}}_\alpha^{\mathrm{t}}(\boldsymbol{\kappa}, d) + \boldsymbol{\mathcal{E}}_\beta^{\mathrm{t}}(\boldsymbol{\kappa}, d) \right\} \\ &= \frac{1}{2\pi} \iint_{-\infty}^{+\infty} \left[\alpha^{\mathrm{t}}(\boldsymbol{\kappa}) \hat{\boldsymbol{\mathcal{E}}}_\alpha^{\mathrm{t}}(\boldsymbol{\kappa}) \exp(\mathrm{i} k_{\alpha z}^{\mathrm{t}} d) + \beta^{\mathrm{t}}(\boldsymbol{\kappa}) \hat{\boldsymbol{\mathcal{E}}}_\beta^{\mathrm{t}}(\boldsymbol{\kappa}) \exp(\mathrm{i} k_{\beta z}^{\mathrm{t}} d) \right] \exp(\mathrm{i} \boldsymbol{\kappa} \cdot \boldsymbol{\rho}) \mathrm{d}k_x \mathrm{d}k_y \end{aligned} \tag{4.21}$$

which describes the intra-crystal diffraction effects of general fields. As shown in Eq. (4.21), the angular spectrum for any $\boldsymbol{\kappa}$ consists of two parts. The propagation of these two parts follows different rules, i.e., multiplication with $\exp(\mathrm{i} k_{\alpha z}^{\mathrm{t}} d)$ or $\exp(\mathrm{i} k_{\beta z}^{\mathrm{t}} d)$. Therefore during the propagation in an anisotropic medium, the polarization state may change. Other existing propagation methods in isotropic media based on the angular spectrum of plane waves, like the Fresnel-integral, can also be extended to anisotropic cases in a similar way.

Plane wave refraction at a plane interface from $\underline{\epsilon}$ into ϵ^{t}

Finally the refraction at the rear surface must be calculated to obtain the transmitted field in the isotropic medium behind. The method is completely analogous to section 4.1. Thus in the following the expressions of the plane waves and the coefficients matrix are given briefly.

The incident, reflected and transmitted plane waves can be expressed as

$$\boldsymbol{E}^{\mathrm{i}}(\boldsymbol{r}) = \alpha^{\mathrm{i}}\hat{\boldsymbol{\mathcal{E}}}^{\mathrm{i}}_{\alpha}\exp(\mathrm{i}\boldsymbol{k}^{\mathrm{i}}_{\alpha}\cdot\boldsymbol{r}) + \beta^{\mathrm{i}}\hat{\boldsymbol{\mathcal{E}}}^{\mathrm{i}}_{\beta}\exp(\mathrm{i}\boldsymbol{k}^{\mathrm{i}}_{\beta}\cdot\boldsymbol{r})\,, \tag{4.22}$$

$$\boldsymbol{E}^{\mathrm{r}}(\boldsymbol{r}) = \alpha^{\mathrm{r}}\hat{\boldsymbol{\mathcal{E}}}^{\mathrm{r}}_{\alpha}\exp(\mathrm{i}\boldsymbol{k}^{\mathrm{r}}_{\alpha}\cdot\boldsymbol{r}) + \beta^{\mathrm{r}}\hat{\boldsymbol{\mathcal{E}}}^{\mathrm{r}}_{\beta}\exp(\mathrm{i}\boldsymbol{k}^{\mathrm{r}}_{\beta}\cdot\boldsymbol{r})\,, \tag{4.23}$$

$$\boldsymbol{E}^{\mathrm{t}}(\boldsymbol{r}) = \boldsymbol{\mathcal{E}}^{\mathrm{t}}\exp(\mathrm{i}\boldsymbol{k}^{\mathrm{t}}\cdot\boldsymbol{r})\,. \tag{4.24}$$

In this case, the incident and reflected plane waves are in the anisotropic medium. The two incident plane waves in Eq. (4.22) share the same transverse wavevector component $\boldsymbol{\kappa}$, and as a consequence there is only one transmitted plane wave in the isotropic medium ϵ^{t}. Following the procedure in section 4.1, first the unknown wavevectors are calculated. The transmitted wavevector is found as $\boldsymbol{k}^{\mathrm{t}} = (k_x, k_y, k^{\mathrm{t}}_z)^{\mathrm{T}}$ with $k^{\mathrm{t}}_z = \left[\epsilon^{\mathrm{t}}k_0^2 - k_x^2 - k_y^2\right]^{1/2}$. The reflected wavevectors $\boldsymbol{k}^{\mathrm{r}}_{\alpha}$ and $\boldsymbol{k}^{\mathrm{r}}_{\alpha}$ need to be calculated by using the quartic in Eq. (4.11). Then the associated electric field eigenvectors $\hat{\boldsymbol{\mathcal{E}}}^{\mathrm{r}}_{\alpha}$ and $\hat{\boldsymbol{\mathcal{E}}}^{\mathrm{r}}_{\beta}$ can be found by solving the eigenvalue-eigenvector problem in Eq. (4.13). Applying the boundary conditions yields four linear equations in a matrix form

$$\underline{\boldsymbol{N}}\begin{pmatrix}\alpha^{\mathrm{r}}\\ \beta^{\mathrm{r}}\\ \mathcal{E}^{\mathrm{t}}_x\\ \mathcal{E}^{\mathrm{t}}_y\end{pmatrix} = \begin{pmatrix}\alpha^{\mathrm{i}}\hat{\mathcal{E}}^{\mathrm{i}}_{\alpha y} + \beta^{\mathrm{i}}\hat{\mathcal{E}}^{\mathrm{i}}_{\beta y}\\ \alpha^{\mathrm{i}}\hat{\mathcal{E}}^{\mathrm{i}}_{\alpha x} + \beta^{\mathrm{i}}\hat{\mathcal{E}}^{\mathrm{i}}_{\beta x}\\ \alpha^{\mathrm{i}}(k^{\mathrm{i}}_{\alpha z}\hat{\mathcal{E}}^{\mathrm{i}}_{\alpha x} - k_x\hat{\mathcal{E}}^{\mathrm{i}}_{\alpha z}) + \beta^{\mathrm{i}}(k^{\mathrm{i}}_{\beta z}\hat{\mathcal{E}}^{\mathrm{i}}_{\beta x} - k_x\hat{\mathcal{E}}^{\mathrm{i}}_{\beta z})\\ \alpha^{\mathrm{i}}(k^{\mathrm{i}}_{\alpha z}\hat{\mathcal{E}}^{\mathrm{i}}_{\alpha y} - k_y\hat{\mathcal{E}}^{\mathrm{i}}_{\alpha z}) + \beta^{\mathrm{i}}(k^{\mathrm{i}}_{\beta z}\hat{\mathcal{E}}^{\mathrm{i}}_{\beta y} - k_y\hat{\mathcal{E}}^{\mathrm{i}}_{\beta z})\end{pmatrix}, \tag{4.25}$$

with the matrix

$$\underline{\boldsymbol{N}} = \begin{pmatrix}-\hat{\mathcal{E}}^{\mathrm{r}}_{\alpha y} & -\hat{\mathcal{E}}^{\mathrm{r}}_{\beta y} & 0 & 1\\ -\hat{\mathcal{E}}^{\mathrm{r}}_{\alpha x} & -\hat{\mathcal{E}}^{\mathrm{r}}_{\beta x} & 1 & 0\\ k_x\hat{\mathcal{E}}^{\mathrm{r}}_{\alpha z} - k^{\mathrm{r}}_{\alpha z}\hat{\mathcal{E}}^{\mathrm{r}}_{\alpha x} & k_x\hat{\mathcal{E}}^{\mathrm{r}}_{\beta z} - k^{\mathrm{r}}_{\beta z}\hat{\mathcal{E}}^{\mathrm{r}}_{\beta x} & k^{\mathrm{t}}_z + \frac{k_x^2}{k^{\mathrm{t}}_z} & \frac{k_x k_y}{k^{\mathrm{t}}_z}\\ k_y\hat{\mathcal{E}}^{\mathrm{r}}_{\alpha z} - k^{\mathrm{r}}_{\alpha z}\hat{\mathcal{E}}^{\mathrm{r}}_{\alpha y} & k_y\hat{\mathcal{E}}^{\mathrm{r}}_{\beta z} - k^{\mathrm{r}}_{\beta z}\hat{\mathcal{E}}^{\mathrm{r}}_{\beta y} & \frac{k_x k_y}{k^{\mathrm{t}}_z} & k^{\mathrm{t}}_z + \frac{k_y^2}{k^{\mathrm{t}}_z}\end{pmatrix}. \tag{4.26}$$

Multiplying $\underline{\boldsymbol{N}}^{-1}$ on both sides of Eq. (4.25) results in

$$\begin{pmatrix}\alpha^{\mathrm{r}}\\ \beta^{\mathrm{r}}\\ \mathcal{E}^{\mathrm{t}}_x\\ \mathcal{E}^{\mathrm{t}}_y\end{pmatrix} = \underline{\boldsymbol{N}}^{-1}\begin{pmatrix}\alpha^{\mathrm{i}}\hat{\mathcal{E}}^{\mathrm{i}}_{\alpha y} + \beta^{\mathrm{i}}\hat{\mathcal{E}}^{\mathrm{i}}_{\beta y}\\ \alpha^{\mathrm{i}}\hat{\mathcal{E}}^{\mathrm{i}}_{\alpha x} + \beta^{\mathrm{i}}\hat{\mathcal{E}}^{\mathrm{i}}_{\beta x}\\ \alpha^{\mathrm{i}}(k^{\mathrm{i}}_{\alpha z}\hat{\mathcal{E}}^{\mathrm{i}}_{\alpha x} - k_x\hat{\mathcal{E}}^{\mathrm{i}}_{\alpha z}) + \beta^{\mathrm{i}}(k^{\mathrm{i}}_{\beta z}\hat{\mathcal{E}}^{\mathrm{i}}_{\beta x} - k_x\hat{\mathcal{E}}^{\mathrm{i}}_{\beta z})\\ \alpha^{\mathrm{i}}(k^{\mathrm{i}}_{\alpha z}\hat{\mathcal{E}}^{\mathrm{i}}_{\alpha y} - k_y\hat{\mathcal{E}}^{\mathrm{i}}_{\alpha z}) + \beta^{\mathrm{i}}(k^{\mathrm{i}}_{\beta z}\hat{\mathcal{E}}^{\mathrm{i}}_{\beta y} - k_y\hat{\mathcal{E}}^{\mathrm{i}}_{\beta z})\end{pmatrix}. \tag{4.27}$$

The matrix multiplication in Eq. (4.27) ends up with the terms $(\mathcal{E}^{\mathrm{t}}_x, \mathcal{E}^{\mathrm{t}}_y)$ of the transmitted plane wave in the isotropic medium behind the crystal. Finally Eq. (4.4) can be used for constructing the output field $\boldsymbol{V}^{\mathrm{out}}$ behind the anisotropic crystal.

4.2 Simulation of Crystals with Thermal Lensing, Stress-Induced Birefringence and Nonlinear Gain Saturation

In the previous section a rigorous non-diagonal component operator for the simulation of light propagation through homogeneous, linear and anisotropic crystals was discussed. Such crystals are typically used in laser resonators for polarization control. However for the simulation of active laser crystals which amplify the light the above given model is not suitable, because it does not contain any gain process. Furthermore due to conversion of pump light into heat, typically there is a temperature profile in the crystal resulting in an optically inhomogeneous medium.

In literature there are plenty of different simulation techniques available for the calculation of light propagation through active laser crystals. There are geometrical optics based techniques [24–26, 140, 158], which, on the one hand, are typically numerically efficient but on the other hand do not include all physical relevant effects. In contrast direct solvers of Maxwell's equations (like FDTD [35, 159] or FEM [31, 160]) provide high simulation accuracy but suffer from high numerical effort. Furthermore there are simulation techniques customized for certain types of input fields (e.g. Gaussian beams [9, 71, 74, 161]) and/or for certain refractive index distributions within the crystal [71, 162, 163]. Beam propagation methods provide a good compromise between numerical effort and simulation accuracy. They are either based on a finite difference approach [46, 47, 164, 165] or on a split-step technique [10, 44, 45]. Split-step beam propagation methods have the advantage that they are based on the numerically efficient fast Fourier Transformation (FFT). Thus in this section a vectorial split-step beam propagation method (vBPM) for light propagation through active laser crystals is given. This component operator is based on the vectorial Helmholtz equation[1] describing light propagation through a weakly inhomogeneous, nonlinear and birefringent medium. The Helmholtz equation is solved by a vBPM which is based on the work of Thylen and Yevick [44]. It is extended by a novel semi-analytical approach for the numerically efficient inclusion of light amplification effects within the vBPM. In addition to the material model for light amplification it is shown how material models for stress-induced birefringence and thermal lensing are included in the non-diagonal component operator.

---

[1] Due to the modeling of light propagation by the vectorial Helmholtz equation this vBPM neglects refraction and depolarization effects at the front and end surfaces of the crystal (like most of the beam propagation methods). In principle this limitation might be overcome by developing an interface operator describing the light propagation through an interface, as it was done for the homogeneous crystal in the previous section.

Fundamentals of the vectorial beam propagation method

Light propagation through a weakly birefringent and nonlinear medium with weak refractive index inhomogeneities given by the dielectric tensor

$$\underline{\boldsymbol{\epsilon}}(\boldsymbol{r},\boldsymbol{V}) = \begin{pmatrix} \epsilon_{11}(\boldsymbol{r},\boldsymbol{V}) & \epsilon_{12}(\boldsymbol{r},\boldsymbol{V}) & \epsilon_{13}(\boldsymbol{r},\boldsymbol{V}) \\ \epsilon_{21}(\boldsymbol{r},\boldsymbol{V}) & \epsilon_{22}(\boldsymbol{r},\boldsymbol{V}) & \epsilon_{23}(\boldsymbol{r},\boldsymbol{V}) \\ \epsilon_{31}(\boldsymbol{r},\boldsymbol{V}) & \epsilon_{32}(\boldsymbol{r},\boldsymbol{V}) & \epsilon_{33}(\boldsymbol{r},\boldsymbol{V}) \end{pmatrix} \tag{4.28}$$

can be described by the Helmholtz equation in matrix form [44]:

$$\left(\underline{\boldsymbol{I}}\frac{\partial^2}{\partial z^2} - \underline{\boldsymbol{M}}^2\right)\begin{pmatrix} V_1 \\ V_2 \end{pmatrix} = 0 \tag{4.29}$$

with the identity matrix $\underline{\boldsymbol{I}}$ and the matrix

$$\underline{\boldsymbol{M}}^2 = -\begin{pmatrix} \nabla_\perp^2 + k_0^2\epsilon_{11}(\boldsymbol{r},\boldsymbol{V}) & k_0^2\epsilon_{12}(\boldsymbol{r},\boldsymbol{V}) \\ k_0^2\epsilon_{21}(\boldsymbol{r},\boldsymbol{V}) & \nabla_\perp^2 + k_0^2\epsilon_{22}(\boldsymbol{r},\boldsymbol{V}) \end{pmatrix}. \tag{4.30}$$

Here $\nabla_\perp^2 = (\frac{\partial^2}{\partial^2 x} + \frac{\partial^2}{\partial^2 y})$ is the transversal nabla operator, $\boldsymbol{r} = (x, y, z)^{\mathrm{T}}$ is the position vector and k_0 is the wavenumber in vacuum. Using the assumption of weak birefringence, nonlinearity and inhomogeneity effects in the active medium, the tensor components of $\underline{\boldsymbol{\epsilon}}(\boldsymbol{r},\boldsymbol{V})$ in Eq. (4.30) can be approximated by [44]

$$\epsilon_{\alpha\beta}(\boldsymbol{r},\boldsymbol{V}) = (n_0 + \tilde{n}_{\alpha\beta}(\boldsymbol{r},\boldsymbol{V}))^2 \approx n_0^2 + 2n_0\tilde{n}_{\alpha\beta}(\boldsymbol{r},\boldsymbol{V}) \tag{4.31}$$

with the indices $\alpha = 1, 2$ and $\beta = 1, 2$. n_0 is the complex linear, isotropic and homogeneous refractive index share of $\underline{\boldsymbol{\epsilon}}(\boldsymbol{r},\boldsymbol{V})$. $\tilde{n}_{\alpha\beta}(\boldsymbol{r},\boldsymbol{V})$ represents the complex nonlinear, anisotropic and inhomogeneous refractive index shares and can be splitted in

$$\tilde{n}_{\alpha\beta}(\boldsymbol{r},\boldsymbol{V}) = \Delta n_{\alpha\beta}^{\text{therm}}(\boldsymbol{r}) + \Delta n_{\alpha\beta}^{\text{birefring}}(\boldsymbol{r},\boldsymbol{V}) + \Delta n_{\alpha\beta}^{\text{gain}}(\boldsymbol{r},\boldsymbol{V}). \tag{4.32}$$

Here $\Delta n_{\alpha\beta}^{\text{therm}}(\boldsymbol{r})$, $\Delta n_{\alpha\beta}^{\text{birefring}}(\boldsymbol{r},\boldsymbol{V})$ and $\Delta n_{\alpha\beta}^{\text{gain}}(\boldsymbol{r},\boldsymbol{V})$ separately describe the effect of thermal lensing, stress-induced birefringence and nonlinear gain on the refractive index. The actual structure of these variables will be discussed in detail in the following subsections.

The Helmholtz equation given by Eq. (4.29) is solved in the following by a vBPM to calculate the light propagation through the active component. The complex amplitude $V_\ell(x, y, z_0 + L)$ of a harmonic field in a plane perpendicular to the optical axis, located at the axial position $z_0 + L$ at the end of the active component, can be calculated from the field $V_\ell(x, y, z_0)$ in front of the active component by:

$$\begin{pmatrix} V_1(z_0+L) \\ V_2(z_0+L) \end{pmatrix} = \prod_{s=1}^{S} \left[\boldsymbol{\mathcal{P}}_s^{\mathrm{SPW}} \left(\frac{\Delta z}{2}\right) \boldsymbol{\mathcal{C}}_s^{\mathrm{NL}} \left(z_0 + \left(s - \frac{1}{2}\right) \Delta z \right) \boldsymbol{\mathcal{P}}_s^{\mathrm{SPW}} \left(\frac{\Delta z}{2}\right) \right] \begin{pmatrix} V_1(z_0) \\ V_2(z_0) \end{pmatrix} \tag{4.33}$$

with the number of vBPM steps $S = L/\Delta z$. Here L represents the total propagation distance and Δz a single split-step distance. Please note that the (x, y) variable dependency of the field was skipped only for better readability. $\boldsymbol{\mathcal{P}}_s^{\mathrm{SPW}}$ is the angular spectrum of plane waves operator [103], given by the diagonal operator:

$$\boldsymbol{\mathcal{P}}_s^{\mathrm{SPW}} \left(\frac{\Delta z}{2}\right) = \begin{pmatrix} \mathcal{P}^{\mathrm{SPW}} & 0 \\ 0 & \mathcal{P}^{\mathrm{SPW}} \end{pmatrix} \tag{4.34}$$

with

$$\mathcal{P}^{\mathrm{SPW}} V_\ell(\boldsymbol{\rho}, z_0) = \mathscr{F}^{-1} \left\{ \mathscr{F} \left[V_\ell(\boldsymbol{\rho}, z_0) \right] \exp \left[\mathrm{i} k_z \frac{\Delta z}{2} \right] \right\}. \tag{4.35}$$

Here $\mathscr{F}$ is the Fourier transformation with the conjugate variables $\boldsymbol{\rho} = (x, y)^{\mathrm{T}}$ and $\boldsymbol{\kappa} = (k_x, k_y)^{\mathrm{T}}$. Furthermore there is $k_z = \left(k^2 - k_x^2 - k_y^2\right)^{(1/2)}$ with the wavenumber $k = \frac{2\pi}{\lambda} n_0$ and the vacuum wavelength λ. Fig. 4.4 illustrates the split-step vBPM given by Eq. (4.33). The operator $\boldsymbol{\mathcal{C}}_s^{\mathrm{NL}} \left(z_0 + \left(s - \frac{1}{2}\right) \Delta z \right)$ on the right hand side of Eq. (4.33) describes the influence

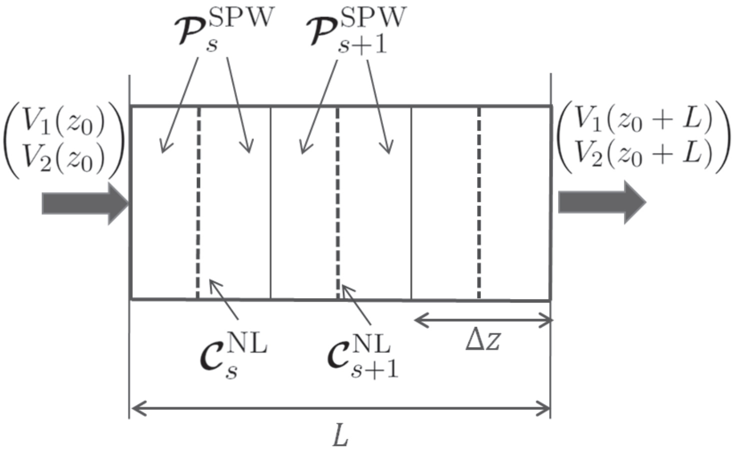

Figure 4.4 – Schematic illustration of the symmetrized vBPM for light propagation through an active laser medium: the component is subdivided into segments of width Δz. Within a segment only linear effects, like diffraction or linear absorption, are included in the angular spectrum of plane waves operators $\boldsymbol{\mathcal{P}}_s^{\mathrm{SPW}}$. The effect of nonlinearity is introduced by the nonlinear operators $\boldsymbol{\mathcal{C}}_s^{\mathrm{NL}}$ in the center of the segments (represented by dashed lines).

of the nonlinear, inhomogeneous and birefringence terms of the active component and is modeled by the non-diagonal operator:

$$\boldsymbol{\mathcal{C}}_s^{\mathrm{NL}}\left(z_0+\left(s-\frac{1}{2}\right)\Delta z\right)=\begin{pmatrix}\mathcal{C}_{11,s}^{\mathrm{NL}} & \mathcal{C}_{12,s}^{\mathrm{NL}}\\ \mathcal{C}_{21,s}^{\mathrm{NL}} & \mathcal{C}_{22,s}^{\mathrm{NL}}\end{pmatrix} \tag{4.36}$$

with

$$\mathcal{C}_{\alpha\beta,s}^{\mathrm{NL}}=\exp\left(\mathrm{i}\frac{2\pi}{\lambda}\int_{z_0+(s-1)\Delta z}^{z_0+s\Delta z}\tilde{n}_{\alpha\beta}(z',\boldsymbol{V})\mathrm{d}z'\right) \tag{4.37}$$

for $\alpha=1,2$ and $\beta=1,2$. $\tilde{n}_{\alpha\beta}(z',\boldsymbol{V})$ can be interpreted locally as the nonlinear, anisotropic and inhomogeneous contribution of the active component's refractive index and is equal to the expression given by Eq. (4.32). For better readability the (x,y) dependency was skipped in the notation. Consequently the integral on the right hand side of Eq. (4.37) describes the optical path length introduced to rays propagating parallel to the optical axis due to this residual refractive index. The contribution of gain can be separated by substituting Eq. (4.32) into Eq. (4.37) resulting in:

$$\mathcal{C}_{\alpha\beta,s}^{\mathrm{NL}}=\mathcal{C}_{\alpha\beta,s}^{\mathrm{gain}}\cdot\mathcal{C}_{\alpha\beta,s}^{\mathrm{t+b}} \tag{4.38}$$

with

$$\mathcal{C}_{\alpha\beta,s}^{\mathrm{gain}}=\exp\left(\mathrm{i}\frac{2\pi}{\lambda}\int_{z_0+(s-1)\Delta z}^{z_0+s\Delta z}\Delta n_{\alpha\beta}^{\mathrm{gain}}(z',\boldsymbol{V})\mathrm{d}z'\right) \tag{4.39}$$

and with

$$\mathcal{C}_{\alpha\beta,s}^{\mathrm{t+b}}=\exp\left[\mathrm{i}\frac{2\pi}{\lambda}\int_{z_0+(s-1)\Delta z}^{z_0+s\Delta z}\Big(\Delta n_{\alpha\beta}^{\mathrm{therm}}(z')+\Delta n_{\alpha\beta}^{\mathrm{birefring}}(z',\boldsymbol{V})\Big)\mathrm{d}z'\right]. \tag{4.40}$$

For small slab sizes Δz the integral in Eq. (4.40) can be approximately solved numerically, ending up with the nonlinear operator

$$\mathcal{C}_{\alpha\beta,s}^{\mathrm{t+b}}\approx\exp\left\{\mathrm{i}\frac{2\Delta z\pi}{\lambda}\left[\Delta n_{\alpha\beta}^{\mathrm{therm}}\left(z_0+\left(s-\frac{1}{2}\right)\Delta z\right)+\Delta n_{\alpha\beta}^{\mathrm{birefring}}\left(z_0+\left(s-\frac{1}{2}\right)\Delta z,\boldsymbol{V}\right)\right]\right\}. \tag{4.41}$$

In principle also the integral in Eq. (4.39) can be approximated in the same way as Eq. (4.41). However, especially for large small-signal gain or strong nonlinear gain saturation inside the active medium, this approximation would require a very small vBPM step size Δz which would increase the computational effort. That is why in the following subsection a novel semi-analytical solution of the integral in Eq. (4.39) is introduced, ending up with a larger acceptable step size Δz and consequently a more numerically efficient vBPM.

To avoid aliasing effects within the vBPM due to propagation of the electric field to the edge of the computational window in a transverse plane (x, y) an absorbing boundary condition must be introduced. The absorber function, which is applied on both field components after each nonlinear operation $\boldsymbol{\mathcal{C}}_s^{\mathrm{NL}}$, is given in Eq. (3) of Jaijonmaa's work [166]. For the realistic simulation of light propagation through the active laser medium by the vBPM, the effects of thermal lensing, birefringence and gain saturation have to be included by the corresponding terms in Eqs. (4.39) and (4.41). The structure of these terms is discussed in the following subsections.

Inclusion of gain by rate equations

In section 2.4 it was shown that the cw light amplification of a global plane wave within an active medium can be described by the Lambert-Beer law (Eq. (2.68)) and a quasi-stationary solution of the rate equation system. In the section above it was also shown that the integral on the right hand side of Eq. (4.39) describes the optical path length introduced to rays propagating parallel to the optical axis. These rays can be interpreted locally as plane waves. Thus the Lambert-Beer law approximately describes the cw light amplification of these local plane waves. For the interpretation of the complex value $\Delta n_{\alpha\beta}^{\mathrm{gain}}(\boldsymbol{r}, \boldsymbol{V})$ in Eq. (4.39), the Lambert-Beer law given by Eq. (2.68) can be formally solved by

$$I(z_0 + \Delta z) = I(z_0) \exp\left(\int_{z_0}^{z_0+\Delta z} g(z')\mathrm{d}z' \right) \tag{4.42}$$

which has a structure equal to that of Eq. (4.39). Consequently if polarization cross-talk by the light amplification effect itself is neglected, the gain coefficient g in Eq. (4.42) is related to $\Delta n_{\alpha\beta}^{\mathrm{gain}}(\boldsymbol{r}, \boldsymbol{V})$ in Eq. (4.39) by:

$$\mathrm{i}\frac{2\pi}{\lambda} 2\Delta n_{\alpha\beta}^{\mathrm{gain}}(\boldsymbol{r}, \boldsymbol{V}) = g \tag{4.43}$$

for $\alpha = \beta$ and $\Delta n_{\alpha\beta}^{\mathrm{gain}}(\boldsymbol{r}, \boldsymbol{V}) = 0$ for $\alpha \neq \beta$. However of course polarization cross-talk due to stress-induced birefringence is separately included by the term $\Delta n_{\alpha\beta}^{\mathrm{birefring}}$. Please note that the additional factor 2 on the left hand side of Eq. (4.43) is due to the fact that Eq. (4.39) is formulated for fields V_ℓ and Eq. (4.42) is formulated for intensities I. Fields and intensities are related with each other through Eq. (2.69). The gain coefficient g in Eq. (4.43) depends on the energy level diagram of the active medium and its corresponding system of rate equations. Corresponding analytical expressions for g are given in section

2.4 and in appendix B. For example in the case of a 4-level-energy-diagram Eq. (2.76) is substituted in Eq. (4.43) resulting in:

$$\Delta n_{\alpha\beta}^{\mathrm{gain}}(\boldsymbol{r},\boldsymbol{V}) \approx \frac{\lambda}{\mathrm{i}4\pi}\frac{g_0}{1+\frac{I}{I_{\mathrm{s}}^{\mathrm{L}}}}. \tag{4.44}$$

for $\alpha = \beta$ with the small-signal gain

$$g_0 = \eta_{\mathrm{p}}\sigma_{12}N\frac{I_{\mathrm{p}}}{I_{\mathrm{s}}^{\mathrm{p}}} \tag{4.45}$$

and the saturation intensity $I_{\mathrm{s}}^{\mathrm{L}}$. In principle now Eq. (4.44) can be substituted into the operator given by Eq. (4.39) which can be solved approximately in the same way as Eq. (4.41). However to ensure a fixed operator accuracy this approximated numerical integration requires a decreasing vBPM step size Δz for an increasing small-signal gain g_0 and for a decreasing saturation intensity I_{s}. Therefore in the following a semi-analytical solution of the integral given in Eq. (4.39) is suggested. This semi-analytical solution in principle works for any step size Δz as long as the small signal gain g_0 can be assumed to be z invariant within this step. Consequently, this semi-analytical vBPM operator is not limited in its accuracy by the integration over the nonlinear gain saturation factor $\Delta n_{\alpha\beta}^{\mathrm{gain}}$ anymore. Only thermal lensing, birefringence and diffraction effects are finally limiting the maximum step size of the vBPM for a given operator accuracy.

The operator given by Eq. (4.39) can be expressed by the two first-order differential equations

$$\frac{\mathrm{d}V_\ell}{\mathrm{d}z} = \frac{1}{2}\frac{g_0}{1+\left(|V_1|^2+|V_2|^2\right)/V_{\mathrm{sat}}^2}V_\ell \quad , \quad \ell = 1,2 \tag{4.46}$$

with

$$V_{\mathrm{sat}}^2 = \frac{I_{\mathrm{s}}^{\mathrm{L}}}{\mathrm{Re}(n_0)\frac{\epsilon_0}{2}c} \tag{4.47}$$

where $\Delta n_{\alpha\beta}^{\mathrm{gain}}(\boldsymbol{r},\boldsymbol{V})$ was substituted by the expression given in Eq. (4.44). As shown in appendix C, the exact solution of Eq. (4.46) is

$$V_\ell(z_0+\Delta z) = \left[\frac{V_{\mathrm{sat}}^2}{|V_1(z_0)|^2+|V_2(z_0)|^2}W\left(\frac{1}{V_{\mathrm{sat}}^2}\exp\left(g_0\Delta z + c_1\right)\right)\right]^{(1/2)} V_\ell(z_0) \quad , \quad \ell = 1,2 \tag{4.48}$$

with

$$c_1 = \ln\left(|V_1(z_0)|^2+|V_2(z_0)|^2\right) + \left(\frac{|V_1(z_0)|^2+|V_2(z_0)|^2}{V_{\mathrm{sat}}^2}\right). \tag{4.49}$$

Please note that there is no explicit analytical expression for the LambertW function, which is implicitly defined by $a = W(a)\exp\left[W(a)\right]$ [167]. Nevertheless there are several math libraries available which can calculate $W(a)$ numerically (see e.g. [183]). However these math libraries are typically limited in their applicability for larger g_0 and/or small V_{sat}^2.

Especially the exponential dependency of Eq. (4.48) on g_0 is crucial. The argument of W in Eq. (4.48) might exceed the maximum possible value which can be expressed by a number in the floating-point format. In the examples which are shown in section 5.3, this was the case and it was not possible to apply any math library directly on Eq. (4.48). However, especially for large g_0 and/or small V_{sat}^2, a semi-analytical inclusion of the non-linear gain is essential to increase the vBPM step-size Δz. Fortunately there is an approximate explicit expression for $W(a)$ which is particularly suitable for large arguments a [167, 168]:

$$W(a) \approx \ln(a) - \ln\ln(a) + \frac{\ln\ln(a)}{\ln(a)}. \tag{4.50}$$

Please note that for the calculation of the intensity I of the resonator mode the intensities of the forward and backward propagating waves I^+ and I^- must be taken into account for stable or unstable standing wave cavities using the equation:

$$I = I^+ + I^-. \tag{4.51}$$

Here the assumption that several slightly different axial modes oscillate with the same transversal mode in the resonator is used [71, 83]. Since the intensity minima of different axial modes are located at different axial positions, spatial hole burning can be neglected. This assumption is reasonable for several realistic solid-state lasers. Furthermore the axial modes are incoherent to each other, due to their slightly different wavelengths. Consequently it is suitable to model only one axial mode to represent all oscillating axial modes in the cavity and neglect the interference between the counterpropagating waves in Eq. (4.51). If the resonator round trip operator is built up according to Eq. (3.7), two vBPM propagation operators given by Eq. (4.33) are required. One vBPM operator is used to propagate the light in $+z$ direction ending up with the intensity distribution $I^+(x, y, z)$ within the active medium volume. The distribution is stored in order to calculate Eq. (4.51) in the second vBPM operator, which describes light propagation in reverse direction. Then the second vBPM operator calculates and stores $I^-(x, y, z)$. Now again the forward propagation can be performed using $I^-(x, y, z)$ of the previous step, ending up with a new $I^+(x, y, z)$. This procedure can be repeated iteratively till a convergence of the round trip operator result is reached. Expressions of g and the resulting semi-analytical formulation of the vBPM for other energy-level-diagrams in the stationary case can be found in a similar way.

Inclusion of thermal lensing

An inhomogeneous temperature distribution $T(x, y, z)$ within the volume of a solid-state active medium induces thermal dispersion and birefringence [17,169,182]. The temperature distribution is brought about by the generation of heat $Q(x, y, z)$ due to non-radiative relaxation processes in an inhomogeneous pumped active medium, in combination with heat flow to the outer periphery due to cooling [83]. Due to the cw operation of the laser, it will be assumed in the following that the inhomogeneous temperature distribution is constant over time. In literature there is a huge variety of possibilities for how the 3D temperature distribution $T(x, y, z)$ in a solid-state active medium can be obtained. In principle these techniques can be classified into simulation and experimental measurement techniques and their useful application depends on the concrete situation of the resonator setup, pump distribution, active medium material and so on. Interested readers are referred to [5, 170–172] for different simulation approaches and to [173, 174] for experimental measurement techniques.

Once the stationary temperature distribution is obtained from one of the above given approaches, thermal dispersion and consequently thermal lensing, which is also sometimes called thermal beam distortion, can be calculated using vBPM. If an isotropic thermal dispersion is assumed, the term $\Delta n_{\alpha\beta}^{\text{therm}}(\boldsymbol{r})$ in Eq. (4.32) can be calculated from the temperature distribution by a Taylor series:

$$\Delta n_{\alpha\beta}^{\text{therm}}(\boldsymbol{r}) = \begin{cases} \frac{\mathrm{d}n}{\mathrm{d}T}(T - T_0) + \frac{1}{2}\frac{\mathrm{d}^2 n}{\mathrm{d}T^2}(T - T_0)^2 + \ldots & \text{for } \alpha = \beta \\ 0 & \text{else} \end{cases} \tag{4.52}$$

where T_0 should be chosen close to the average operation temperature of the active medium. The thermal coefficients $\frac{\mathrm{d}n}{\mathrm{d}T}, \frac{\mathrm{d}^2 n}{\mathrm{d}T^2}, \ldots$ can be fitted from experimental measurements of the refractive index for different temperatures. For Nd:YAG the coefficient $\frac{\mathrm{d}n}{\mathrm{d}T}$ is around $7.3 \times 10^{-6} 1/°K$ for $T_0 = 40°C$ [175]. Please note that in Eq. (4.52) the refractive index share due to thermal lensing is not a function of the resonator mode $\boldsymbol{V}$ because a linear material response is assumed. In principle it is also possible to get $\Delta n_{\alpha\beta}^{\text{therm}}(\boldsymbol{r})$ directly by measurements. Direct measurement techniques for the determination of the thermal lenses are described e.g. in [15, 176].

Inclusion of stress-induced birefringence

Besides isotropic thermal dispersion, an inhomogeneous temperature distribution results in anisotropic mechanical stress in solid-state active media. Due to the photoelastic effect this stress induces birefringence which can be described according to [16] by an indicatrix

$$(B_{xx}^0 + \Delta B_{xx})x^2 + (B_{yy}^0 + \Delta B_{yy})y^2 + (B_{zz}^0 + \Delta B_{zz})z^2 + 2\Delta B_{xy}xy + 2\Delta B_{xz}xz + 2\Delta B_{yz}yz = 1 \tag{4.53}$$

with the principal coordinate system axes x, y, z and the relative dielectric impermeabilities $B^0_{xx}, B^0_{yy}, B^0_{zz}$ of the unperturbed active medium's indicatrix. The changes of the relative dielectric impermeability tensor

$$\Delta B_{ij} = \sum_{kl} p_{ijkl} \hat{\epsilon}_{kl} \ , \tag{4.54}$$

with the indices $i, j, k, l = 1, 2, 3$, are caused by the strain tensor $\hat{\epsilon}_{kl}$ and the photoelastic fourth-rank tensor p_{ijkl}. Depending on the temperature profile, the strain tensor can be obtained from analytical formulas [16, 172] or from a finite-element analysis [18, 178]. Please note that for the calculation of Eq. (4.54) the strain tensor and the photoelastic tensor must be in the same crystal coordinate system given by the crystal cut direction [16]. If necessary, the tensors have to be transformed into the desired coordinate system using coordinate rotations [16]. In this work the changes of the relative dielectric impermeability tensor are calculated by the photoelastic tensor. Furthermore it is possible to calculate the photoelastic tensor by

$$p_{ijkl} = \sum_{mn} q_{ijmn} C_{mnkl} \tag{4.55}$$

from the piezo-optic tensor q_{ijmn} and the elasticity tensor C_{klmn}. Tabulated tensor data for many crystals can be found in [179, 180]. Please note that in the literature given above the tensor data were measured for temperature regions which might be different from the operation temperature region of the actual active medium. In this case the photoelastic tensor or the piezo-optic tensor could be measured e.g. by interferometry [181]. Before the contribution of $n^{\text{birefring}}_{\alpha\beta}(\boldsymbol{r}, \boldsymbol{V})$ on the nonlinear vBPM step given by the operator $\boldsymbol{\mathcal{C}}^{\text{NL}}_s\left(z_0 + \left(s - \frac{1}{2}\right)\Delta z\right)$ in Eq. (4.36) and Eq. (4.37) is derived, please note that the operator $\boldsymbol{\mathcal{C}}^{\text{NL}}_s\left(z_0 + \left(s - \frac{1}{2}\right)\Delta z\right)$ can be interpreted locally as a multiplication of the incident field with a polarization and position-dependent optical path length. This optical path length is obtained by adding up the optical paths of rays propagating parallel to the optical axis within one vBPM slab with thickness Δz. As illustrated in Fig. 4.5 different optical path lengths for different positions $\boldsymbol{\rho} = (x, y)^{\text{T}}$ in the initial transversal plane $z_0 + (s-1)\Delta z$ are obtained due to the inhomogeneous $\tilde{n}_{\alpha\beta}(z', \boldsymbol{V})$ distribution. To include the polarization dependency of the optical path length due to birefringence, each ray carries the local electric field vector $(V_1(\boldsymbol{r}), V_2(\boldsymbol{r}))^{\text{T}}$. For small slab thicknesses Δz it is allowed to assume that the direction of the rays does not change within a single nonlinear vBPM step. Consequently all rays, which can also be interpreted locally as plane waves, propagate in the normalized direction $\hat{\boldsymbol{u}} = (0, 0, 1)^T$ and for each ray there are principal axes of the indicatrix given by Eq. (4.53). Therefore the eigenvalue problem [16]

$$\begin{pmatrix} B^0_{xx} + \Delta B_{xx} & \Delta B_{xy} \\ \Delta B_{yx} & B^0_{yy} + \Delta B_{yy} \end{pmatrix} \begin{pmatrix} V_1(\boldsymbol{r}) \\ V_2(\boldsymbol{r}) \end{pmatrix} = \frac{1}{n^2} \begin{pmatrix} V_1(\boldsymbol{r}) \\ V_2(\boldsymbol{r}) \end{pmatrix} \tag{4.56}$$

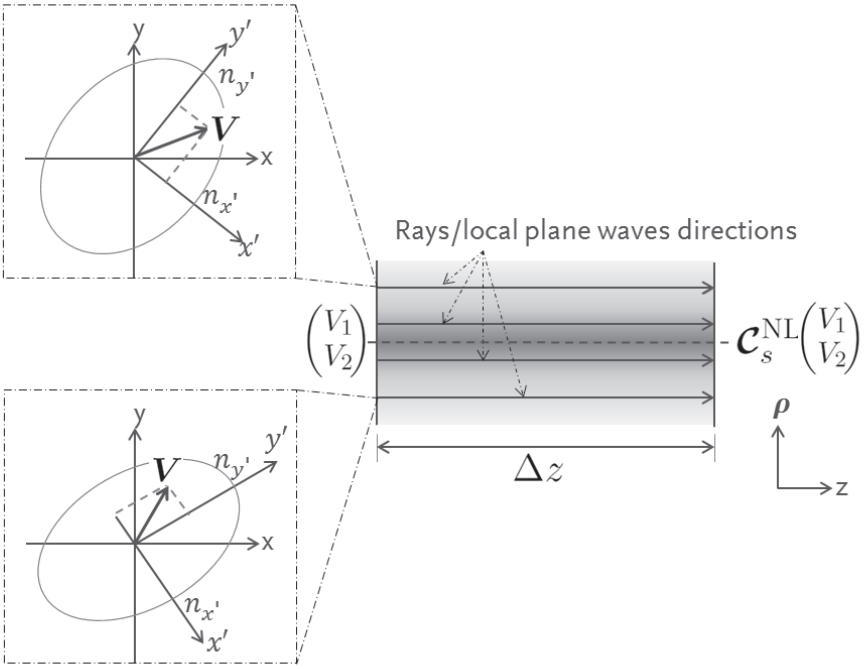

Figure 4.5 – Physical interpretation of a single nonlinear vBPM operation $\boldsymbol{\mathcal{C}}_s^{\mathrm{NL}}$ within a single slab with thickness Δz: the result of the operation is obtained by mapping the complex optical path length (OPL) introduced by the complex refractive index modulation within the slab onto the initial field distribution $(V_1, V_2)^{\mathrm{T}}$, which is sampled on a transversal grid $\boldsymbol{\rho}_n$. Due to the small slab thickness and a paraxial initial field, the OPL can be evaluated along rays propagating parallel to the optical axis. Each transversal grid point is the origin of a ray/local plane wave with a certain polarization vector $\boldsymbol{V}$ in the transversal x-y-plane. Due to the stress-induced birefringence, the OPL for each ray/local plane wave has to be evaluated for the two orthogonal polarization components parallel to the principal axes α' and β'. Due to the position-dependent nature of the electric permittivity tensor of the active medium, for each ray another orientation and shape of the indicatrix must be considered in the OPL analysis. In the left part of the figure two example indicatrices for different rays with different polarization vectors $\boldsymbol{V}$ are given.

has to be solved, ending up with the two eigenvalues $1/n_{x'}^2$ and $1/n_{y'}^2$. The directions of the two orthogonal axes in the $x-y$-plane are given by the eigenvectors $\boldsymbol{V}_{x'}$ and $\boldsymbol{V}_{y'}$. Before the optical path length of each ray is evaluated in the nonlinear vBPM step, it is convenient to project the polarization vector in the x-y-coordinate system onto the principal x'-y'-coordinate system. So the nonlinear vBPM operator given by Eqs. (4.36) and (4.37) can be rewritten as:

$$\boldsymbol{\mathcal{C}}_s^{\mathrm{NL}} = \left(\boldsymbol{\mathcal{C}}_s^{\mathrm{Proj}}\right)^{-1} \begin{pmatrix} \mathcal{C}_{11,s}^{\mathrm{NL}} & 0 \\ 0 & \mathcal{C}_{22,s}^{\mathrm{NL}} \end{pmatrix} \boldsymbol{\mathcal{C}}_s^{\mathrm{Proj}} \tag{4.57}$$

with

$$\mathcal{C}_{\alpha'\alpha',s}^{\mathrm{NL}} = \exp\left(\mathrm{i}\frac{2\pi}{\lambda}\int_{z_0+(s-1)\Delta z}^{z_0+s\Delta z} \tilde{n}_{\alpha'\alpha'}(z', \boldsymbol{V})\mathrm{d}z'\right), \tag{4.58}$$

for $\alpha' = 1, 2$, and the polarization vector projection operator

$$\boldsymbol{\mathcal{C}}_s^{\text{Proj}} \begin{pmatrix} V_1(\boldsymbol{\rho}) \\ V_2(\boldsymbol{\rho}) \end{pmatrix} = \frac{\begin{pmatrix} V_1(\boldsymbol{\rho}) \\ V_2(\boldsymbol{\rho}) \end{pmatrix} \cdot \boldsymbol{V}_{x'}(\boldsymbol{\rho})}{|\boldsymbol{V}_{x'}(\boldsymbol{\rho})|} \boldsymbol{V}_{x'}(\boldsymbol{\rho}) + \frac{\begin{pmatrix} V_1(\boldsymbol{\rho}) \\ V_2(\boldsymbol{\rho}) \end{pmatrix} \cdot \boldsymbol{V}_{y'}(\boldsymbol{\rho})}{|\boldsymbol{V}_{y'}(\boldsymbol{\rho})|} \boldsymbol{V}_{y'}(\boldsymbol{\rho}) \tag{4.59}$$

per position $\boldsymbol{\rho} = (x, y)^{\mathrm{T}}$ in the transversal plane in front of slab s. After the nonlinear vBPM step, the inverse projection operator $\left(\boldsymbol{\mathcal{C}}_s^{\text{Proj}}\right)^{-1}$ projects the polarization vector back into the original x-y-coordinate system. Finally there is

$$\tilde{n}_{\alpha'\beta'}(z', \boldsymbol{V}) = \Delta n_{\alpha'\beta'}^{\text{therm}}(\boldsymbol{r}) + \Delta n_{\alpha'\beta'}^{\text{birefring}}(\boldsymbol{r}, \boldsymbol{V}) + \Delta n_{\alpha'\beta'}^{\text{gain}}(\boldsymbol{r}, \boldsymbol{V}). \tag{4.60}$$

Due to the assumption of an isotropic behavior of the thermal lensing and nonlinear gain effects, the terms $n_{\alpha'\beta'}^{\text{therm}}$ and $\Delta n_{\alpha'\beta'}^{\text{gain}}$ are equal to the corresponding terms in the x-y-coordinate system given by Eq. (4.52) and Eq. (4.44). If a dielectric active crystal is assumed which has an isotropic behavior in the absence of stress, there is $B_{xx}^0 = B_{yy}^0 = B^0$ and $\Delta B_{xy} = \Delta B_{yx}$. In this case the eigenvalue problem given by Eq. (4.56) has the two solutions [16]:

$$1/n_{x'}^2 = B^0 + \frac{1}{2}(\Delta B_{xx} + \Delta B_{yy}) + \frac{1}{2}\left[(\Delta B_{xx} - \Delta B_{yy})^2 + 4\Delta B_{xy}^2\right]^{1/2} \tag{4.61}$$

and

$$1/n_{y'}^2 = B^0 + \frac{1}{2}(\Delta B_{xx} + \Delta B_{yy}) - \frac{1}{2}\left[(\Delta B_{xx} - \Delta B_{yy})^2 + 4\Delta B_{xy}^2\right]^{1/2}. \tag{4.62}$$

Consequently $\Delta n_{\alpha'\beta'}^{\text{birefring}}(\boldsymbol{r}, \boldsymbol{V})$ can be expressed by [16]:

$$\Delta n_{\alpha'\beta'}^{\text{birefring}}(\boldsymbol{r}, \boldsymbol{V}) = \begin{cases} -\frac{n_0^3}{2}(\frac{1}{n_{x'}^2} - B^0) \text{ for } \alpha' = \beta' = 1 \\ -\frac{n_0^3}{2}(\frac{1}{n_{y'}^2} - B^0) \text{ for } \alpha' = \beta' = 2 \\ 0 \text{ else} \end{cases} \tag{4.63}$$

Chapter 5

Applications and Numerical Examples

In the previous chapters a generalized Fox-Li algorithm was introduced for the fully vectorial and flexible analysis of cw solid-state laser resonators. In this chapter several different examples are given to demonstrate the novel theoretical concepts. The concepts were implemented in the commercial field tracing software VirtualLab [177]. Furthermore the accuracy of the concepts is proven by the simulation of a real-world laser resonator and the comparison between published experimental and simulation results. Finally the techniques are applied in section 5.3 to improve the beam quality and output power of a cw Nd:YAG laser suffering from thermal lensing, stress-induced birefringence and nonlinear gain saturation.

5.1 Simulation of Resonator with Brewster Window

The first example is used to demonstrate the influence of different round trip operator structures on the solution of Eq. (3.12) according to Fig. 3.6 in the absence of an active medium. Therefore in a first step a diagonal round trip operator is used for the resonator simulation. After that polarization cross-talk effects are included in the simulation, ending up with a non-diagonal round trip operator. Fig. 5.1 gives the example resonator setup to be investigated. It is a resonator with plane mirrors (M1 and M2) including a 3 mm thick Brewster window (BW). The BW is made of fused silica (refractive index $n = 1.4574$ @ 632.8 nm) and is placed under a tilt angle of 55.544 degrees with respect to the optical axis z inside the cavity. Also a Galileo's telescope (GT) is used for beam expansion inside the resonator. It is built by a negative lens with two concave spherical surfaces with radius of curvature $r = 52.02$ mm each and a central thickness of 3 mm. The positive lens is made by two convex spherical surfaces with radius of curvature $r = 102.6$ mm each and central thickness of 3 mm. Both lenses are made of N-BK7 ($n = 1.5155$ @ 632.8 nm),

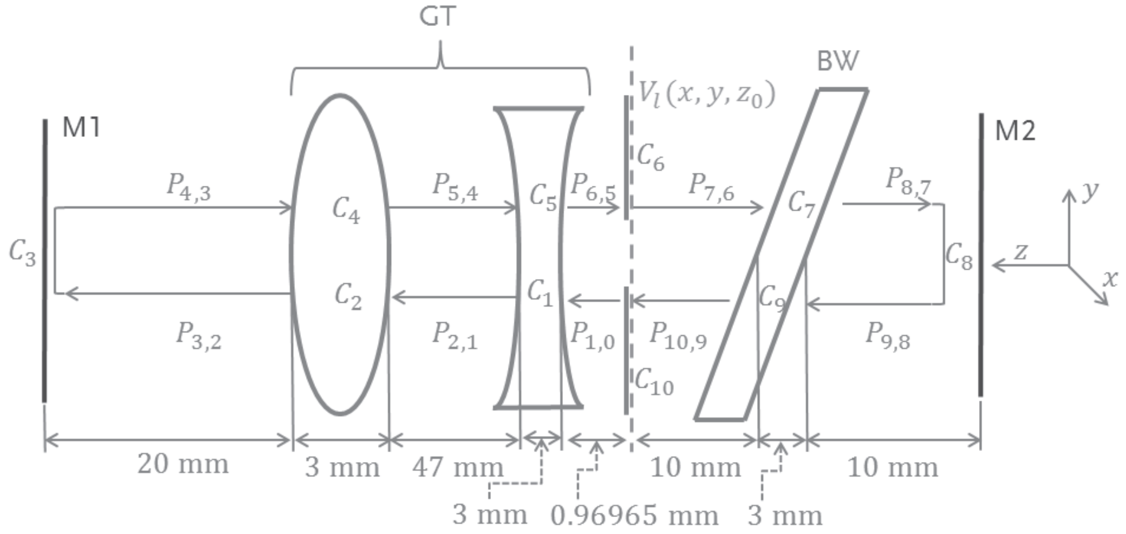

Figure 5.1 – Resonator with plane mirrors M1 and M2, Brewster window (BW) and intra-cavity Galileo's telescope (GT). Round trip operator consists of different component operators in forward ($\mathcal{C}_1$ to $\mathcal{C}_3$, $\mathcal{C}_9$ to $\mathcal{C}_{10}$) and backward ($\mathcal{C}_4$ to $\mathcal{C}_8$) direction and free-space propagation operators between the optical components ($\mathcal{P}_{1,0}$ to $\mathcal{P}_{10,9}$) to calculate the transversal dominant eigenmode $V_\ell(x, y, z_0)$ in the plane of the telescope aperture (denoted by dashed line).

so that the telescope expands the beam diameter by a factor of around 2. It is assumed that the axial mode inside the cavity has a wavelength of 632.8 nm. Mirror M1 and M2 have a circular aperture with a 4 mm diameter. Mirror M1 has a reflectance of $R = 1$. The outcoupling Mirror M2 has a reflectance $R = 0.95$. Furthermore, in the target plane $z = z_0$ there is a circular aperture with a 1 mm diameter in front of the negative telescope lens, where the transversal resonator eigenmode $V_\ell(x, y, z_0)$ is calculated.

Different component operators are used for the different subdomains of the resonators. In practice component and free-space propagation operators which give a good compromise between numerical effort and simulation accuracy are chosen. To illustrate the difference between diagonal and non-diagonal round trip operators, the resonator analysis is performed twice, using two different component operators for the Brewster window. The remaining operators per component ($\mathcal{C}_1$ to $\mathcal{C}_{10}$) are unchanged for both analyses. They are given in Table 5.1.

In the first analysis the component operator of the BW is the diagonal Jones matrix given by Eq. (3.19). Consequently there is a diagonal round trip operator which neglects polarization cross-talk effects. In the second analysis, a combination of the SPW operator given by Eq. (2.30) and (2.31) (for the propagation inside the homogeneous glass) and the rigorous interface operator discussed on page 40ff. for the simulation of the Fresnel losses at both interfaces of the Brewster window is applied. It is important to note that in the second analysis cross-talk between the E_x and E_y field components is included. This means that for the second analysis the round trip operator is non-diagonal.

Table 5.1 – Component operators used in different domains of the resonator setup given in Fig. 5.1. The corresponding equations or references for the component operators are given in brackets.

Component operator	Simulation technique used
$\boldsymbol{\mathcal{C}}_1$	Collins Integral [48–50]
$\boldsymbol{\mathcal{C}}_2$	Collins Integral [48–50]
$\boldsymbol{\mathcal{C}}_3$	TEA (Eq. (3.25))
$\boldsymbol{\mathcal{C}}_4$	Collins Integral [48–50]
$\boldsymbol{\mathcal{C}}_5$	Collins Integral [48–50]
$\boldsymbol{\mathcal{C}}_6$	TEA (Eq. (3.25))
$\boldsymbol{\mathcal{C}}_7$	Interface Op. (see page 40ff.) or Jones Matrix (Eq. (3.19))
$\boldsymbol{\mathcal{C}}_8$	TEA (Eq. (3.25))
$\boldsymbol{\mathcal{C}}_9$	Interface Op. (see page 40ff.) or Jones Matrix (Eq. (3.19))
$\boldsymbol{\mathcal{C}}_{10}$	TEA (Eq. (3.25))

In the field tracing based round trip operator concept given by Eq. (3.7) it is also possible to combine the simulation of several subdomains of the resonator by a single propagation technique. Due to the paraxiality of the telescope (formally described by the operators $\boldsymbol{\mathcal{C}}_2\boldsymbol{\mathcal{P}}_{2,1}\boldsymbol{\mathcal{C}}_1\boldsymbol{\mathcal{P}}_{1,0}$ and $\boldsymbol{\mathcal{P}}_{6,5}\boldsymbol{\mathcal{C}}_5\boldsymbol{\mathcal{P}}_{5,4}\boldsymbol{\mathcal{C}}_4$) the Collins integral [48–50] can be used to simulate the complete telescope within one step in each propagation direction. For the remaining free-space propagation operators ($\boldsymbol{\mathcal{P}}_{3,2}$, $\boldsymbol{\mathcal{P}}_{4,3}$ and $\boldsymbol{\mathcal{P}}_{7,6}$ to $\boldsymbol{\mathcal{P}}_{10,9}$) the SPW operator given by Eqs. (2.30) and (2.31) is used.

After the formulation of the round trip operator $\boldsymbol{\mathcal{R}}$ the corresponding eigenvalue problem given by Eq. (3.12) is solved using the iterative power method given by Eq. (3.38) including the normalization factor given by Eq. (3.43) due to the absence of an active medium. After each iteration the term $|\gamma_\ell^{(j)}|$ is calculated according to Eq. (3.41). The convergence of the iterative power method is monitored using the deviation term

$$\sigma_\ell^{(j)} := \frac{\iint \left| V_\ell^{(j)}(x,y,z_0) - V_\ell^{(j+1)}(x,y,z_0) \exp\left[\mathrm{i}\phi_\ell^{(j)} \right] \right|^2 \mathrm{d}x\mathrm{d}y}{\iint |V_\ell^{(j)}(x,y,z_0)|^2 \mathrm{d}x\mathrm{d}y} \tag{5.1}$$

between adjacent round trip iteration results $V_\ell^{(j)}(x,y,z_0)$ and $V_\ell^{(j+1)}(x,y,z_0)$ in the target plane (x,y,z_0) and with $\phi_\ell^{(j)}$ given by Eq. (3.50).

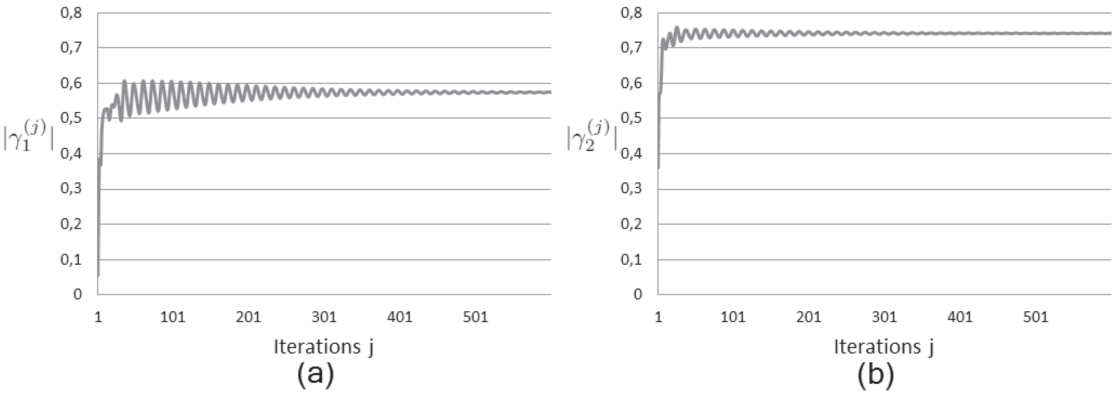

Figure 5.2 – Evolution of resonator round trip losses in terms of $|\gamma_\ell^{(j)}|$ for $E_x(= V_1)$ component (a) and $E_y(= V_2)$ component (b). Separate absolute eigenvalues are obtained for different polarization components, due to the diagonal resonator round trip operator used.

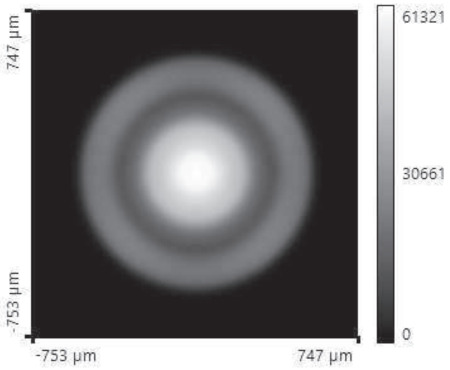

Figure 5.3 – Amplitude of the dominant transversal resonator eigenmode obtained after 600 iterations. The eigenmode is linearly polarized purely in E_y, due to the diagonal resonator round trip operator used. Its non-Gaussian shape is mainly caused by the intracavity aperture.

Brewster window modeled by diagonal Jones Matrix

At first the resonator analysis is performed by using the diagonal Jones matrix given by Eq. (3.19) to simulate the Brewster window. In this case the diagonal round trip operator results in a decoupling between the $E_x(= V_1)$ and $E_y(= V_2)$ components, ending up with two separate eigenvalue problems. Thus as shown in Fig. 5.2 the terms $|\gamma_\ell^{(j)}|$ converge to two different absolute eigenvalues $|\gamma_\ell| = \lim_{j\to\infty} |\gamma_\ell^{(j)}|$ for $\ell = 1, 2$. From the eigenvalues it can be seen that the E_x component experiences higher round trip losses than the E_y component. This results in an a linearly polarized dominant resonator eigenmode with component E_y only, given in Fig. 5.3. In Fig. 5.3 just the E_y field component is shown, because it has a 10^{86} times larger amplitude than the E_x component. The corresponding deviation $\sigma_2^{(j)}$ for the E_y component is given in logarithmic scaling in Fig. 5.4. It clearly shows the convergence of the eigenmode.

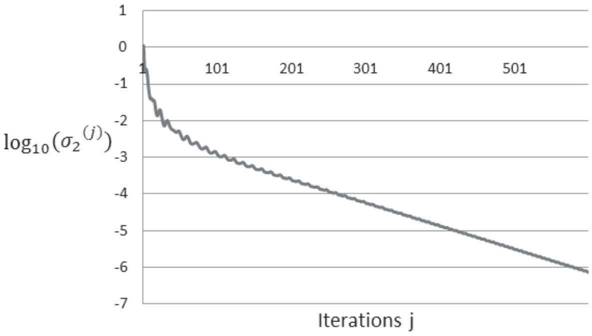

Figure 5.4 – Evolution of deviation $\sigma_2^{(j)}$ between adjacent iteration results for the E_y component obtained by the diagonal round trip operator. Only the deviation of the E_y component is shown, because its amplitude has a 10^{86} times larger amplitude than the E_x component. For better illustration, the vertical axis was scaled logarithmically.

Brewster window modeled by non-diagonal Interface Operator

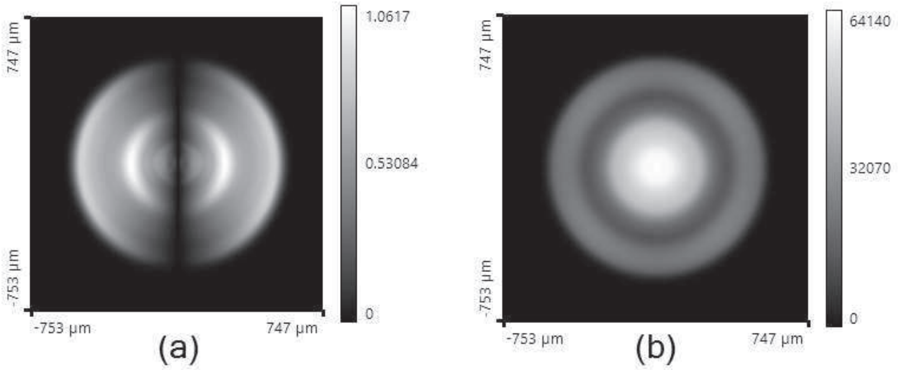

Figure 5.5 – Amplitude of the vectorial dominant transversal resonator eigenmode obtained after 400 iterations for its E_x component (a) and its E_y component (b). There is a different shape between both field components due to the application of the non-diagonal round trip operator, which includes polarization cross-talk.

In the case of the non-diagonal round trip operator the dominant resonator eigenmode obtained after 400 iterations is given in Fig. 5.5. Figs. 5.6 and 5.7 show the corresponding convergence of $|\gamma_\ell^{(j)}|$ and $\sigma_\ell^{(j)}$ for E_x and E_y components. In the beginning there are different round trip losses for the two polarization directions due to the different Fresnel reflection losses at the Brewster window, resulting in a strong decay of the power of the E_x component. Finally the laser will oscillate with almost linear E_y-polarized light, which is typically the case for intracavity Brewster window arrangements [71]. However, due to the cross-talk described in Eq. (3.12), the round trip losses in steady state for the E_x and E_y components are the same, so that a small E_x component will remain. In any case, the values of γ_ℓ for both polarization components in steady state have to be equal for non-diagonal round trip operators, due to polarization cross-talk. The physical interpretation can be directly concluded from the solution by the iterative power method: let's assume that there exists a set of coupled operator equations with different steady state solutions γ_ℓ. In this case there would be different round trip losses and/or phase shifts for the different polarization components, resulting in a change of power ratio and/or phase between the E_x and E_y components. Due to the polarization cross-talk this power and/or phase relation change would directly influence the non-diagonal operators, resulting in a changing round trip operator. Due to the changing round trip operator, the γ_ℓ of both components would also change. This change will go on till the round trip losses and phase shifts are equal for both polarization components. So coupled operator equations will always tend to steady state solutions with equal γ_ℓ for both polarization components. Only the eigenvalues γ_ℓ for both field components are equal. As shown in Fig. 5.5 the two polarization components representing the dominant eigenmode of the resonator can be significantly different for E_x and E_y. Please note again that even a polarization cross-talk as weak as the one that appears at a plane Brewster window is sufficient to couple the problem in Eq. (3.12).

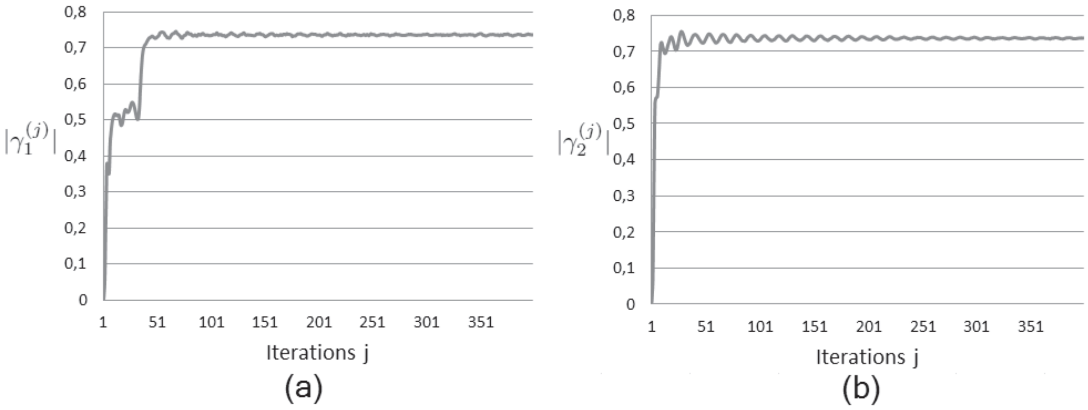

Figure 5.6 – Evolution of resonator round trip losses in terms of $|\gamma_\ell^{(j)}|$ for E_x component (a) and E_y component (b) in the case of the non-diagonal round trip operator. Due to the polarization cross-talk the round trip losses degenerate to the same value for both components in steady state.

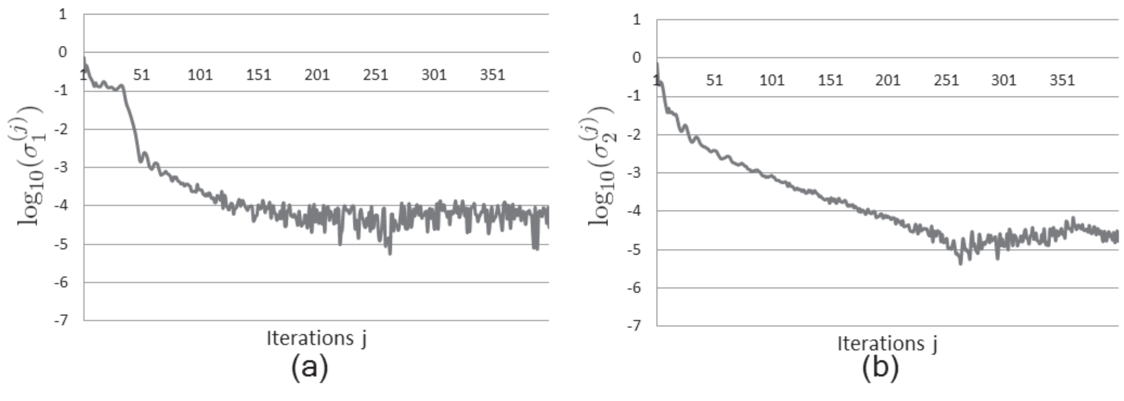

Figure 5.7 – Evolution of deviation $\sigma_\ell^{(j)}$ between adjacent iteration results for E_x component (a) and E_y component (b) in the case of the non-diagonal round trip operator. For better illustration, the vertical axes were scaled logarithmically.

The polarization cross-talk is also essential for explaining the non-monotonous decay of the deviation given in Fig. 5.7. Fox and Li [7, 8] showed that in the case of the scalar eigenvalue problem, the relative change between adjacent iteration results of the power method is decaying monotonous. For the vectorial case, this would mean that the deviation $\sigma_\ell^{(j)}$ always decays for an increasing number of iterations. However, as seen in Fig. 5.7 this is not the case for general vectorial coupled problems. The reason is that the iterative power method was started by an initial field with different random phases for the E_x and E_y components. Due to this fortuitousness of the polarization of the initial vectors, the different polarization components have a different size of the nonzero projection in the direction of the eigenmode associated with the dominant eigenvalue. So in the uncoupled case both initial components would need a different number of iterations to reach specific accuracy of the eigenmode. However, due to the component coupling, a change of one component directly influences the round trip operator of the other component, which consequently changes the component output. So the fluctuation of the deviation is caused by the adaption of the proximity to the solution of the different components. Anyway, as seen in Fig. 5.7, the overall tendency of the deviation is decaying so that the solution of the eigenvalue problem clearly converges to a deviation threshold of approximately 10^{-4}. Further iterations will not lead to a lower deviation than the deviation threshold. This is due to the limited numerical accuracy of the round trip operator. An increase of the round trip operator accuracy would decrease the deviation threshold, but also might increase the computational effort. Also the deviation threshold strongly depends on the simulation technique used. This can be clearly seen if the deviation evolution of the ideal Brewster window modeled by the Jones matrix is compared with the more realistic modeling by the interface operator. Obviously the accuracy of the round trip operator is mainly limited by the numerical accuracy of the interface operator. That is why there is no deviation threshold in Fig. 5.4.

In section 3.4 two vector extrapolation based eigenvalue solvers, namely the RRE and the MPE, were given. In contrast to the iterative power method they provide a faster convergence and by this a reduced number of required round trip operations. Thus the overall computational time can be decreased by the application of these advanced eigenvalue solvers. In the following this higher convergence velocity should be demonstrated by applying different variations of MPE and RRE on the resonator setup with non-diagonal round trip operator given above. Fig. 5.8 shows the convergence speed of cycled single round trip RRE and cycled single round trip MPE using 12 iterations per cycle, in comparison to the iterative power method. By using the vector extrapolation methods the required number of round trip operations could be decreased by 70 percent for the MPE and around 62 percent for the RRE, if a target deviation of 10^{-4} is assumed. As it was discussed above, a further decrease of the deviation clearly beyond the deviation threshold

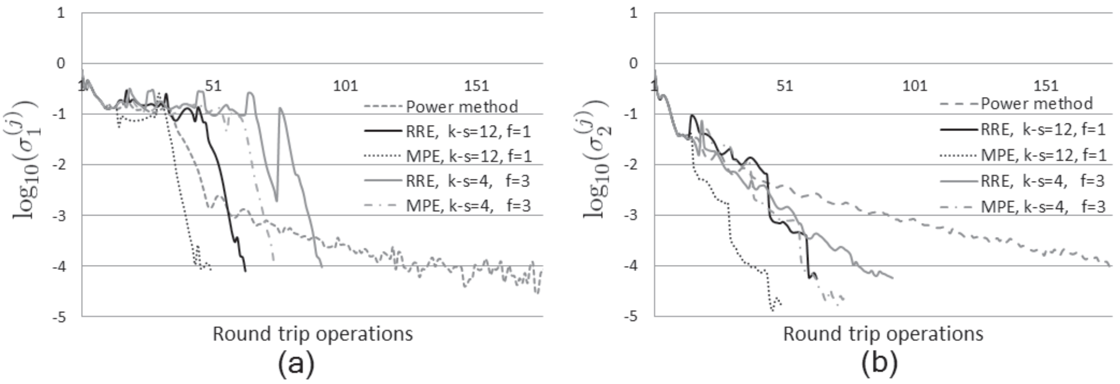

Figure 5.8 – Convergence velocity of different eigenvalue solvers for the coupled eigenvalue problem given by the resonator setup in Fig. 5.1. The evolution of the deviations $\sigma_\ell^{(j)}$ between adjacent iteration results for the coupled E_x(a) and E_y (b) components is shown. Please note that for better illustration, the vertical axes were scaled logarithmically. The target deviation of 10^{-4} for both field components is achieved after 51 round trip operations for the cycled single round trip MPE and after 75 round trip operations for the cycled multi round trip MPE. The RRE reaches the target deviation after 64 round trip operations for the cycled single round trip method and after 93 round trip operations for the cycled multi round trip method. In contrast, the iterative power method requires 170 round trip operations to achieve the same accuracy level.

of 10^{-4} is unfeasible, independently of the eigenvalue solver technique applied, due to the limited accuracy of the round trip operator used. An increase of the round trip operator accuracy would further decrease the minimum achievable deviation. Due to the efficient implementation of the RRE and MPE algorithms by the QR factorization, the computational time for calculating $W_{\ell,s,k}^{\mathrm{MPE}}$ or $W_{\ell,s,k}^{\mathrm{RRE}}$ from a set of iteration results $\boldsymbol{V}^{(j)}$ almost does not require any additional time. The major numerical effort has to be spent on the calculation of the resonator round trip operation $\boldsymbol{\mathcal{R}}$. Consequently a reduction of the required number of round trip operations by around 70 and 62 percent respectively, results in a similar reduction of the computational time.

If the cycled multi round trip method ($f > 1$) is used, only every f-th round trip operator result will be taken into account for the vector extrapolation method to calculate the starting condition for the next cycle. This technique decreases the size of $Q_\ell^{(k-1)}$, especially for fields V_ℓ with a high number of sampling points O. Fig. 5.8 shows the convergence behavior of the multi round trip vector extrapolation methods compared to the single round trip methods. For better comparison between the techniques, after each round trip and normalization operation the deviation was calculated according to Eq. (5.1). It can be seen that the memory advantage of the multi round trip vector extrapolation methods is dearly-bought by a decreased convergence velocity compared to the single round trip approaches. This decreased convergence velocity is caused by an increased error-proneness of the multi round trip vector extrapolation methods on the round trip operator errors due to the reduced number of fields used for the extrapolation step.

5.2 Generation of a Radially Polarized Laser Beam by Use of the Birefringence of a c-cut Nd:YVO4 Crystal

In 2006, Yonezawa et al. [184] introduced a laser resonator including an anisotropic c-cut Nd:YVO$_4$ crystal, for the generation of a radially polarized transversal resonator mode. The main idea is the induction of different optical paths between an extraordinary and an ordinary beam by the birefringence of the crystal. If the distance between a spherical and a plane cavity mirror is chosen correctly, the effective optical cavity length of the ordinary beam will be in the unstable region, whereas the optical cavity length of the extraordinary beam, which is radially polarized, is in the stable region. Consequently the resonator round trip losses, which are higher for the ordinary beam than for the extraordinary beam, will damp out the ordinary one. The corresponding resonator is given in Fig. 5.9 and Table 5.2.

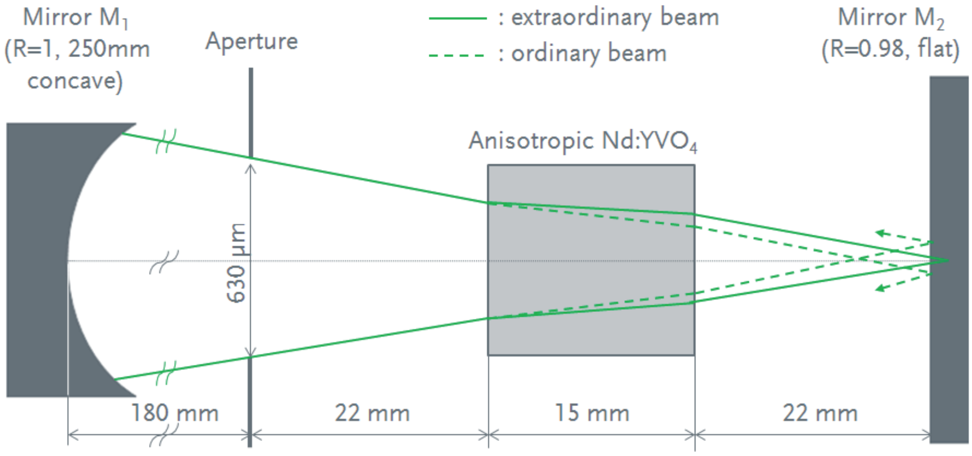

Figure 5.9 – Schematic of a laser resonator for generation of a radially polarized beam. It is shown that the ordinary and extraordinary beams take different optical paths in the Nd:YVO$_4$ rod because of the different refractive indices [184]. The values used for other parameters can be found in Table 5.2.

In their work Yonezawa et al. gave an experimental verification of the appearance of a radially polarized beam. In the following the above described generalized Fox-Li algorithm is applied to reproduce Yonezawa's experimental measurement results by a computer simulation. The round trip operator $\boldsymbol{\mathcal{R}}$ is described according to Eq. (3.7) by a sequence of component operators $\boldsymbol{\mathcal{C}}$ given in Table 5.3 and SPW operators given by Eqs. (2.30) and (2.31) for the free-space propagation $\boldsymbol{\mathcal{P}}$ between the components. For the simulation of the birefringence effects of the homogeneous, uniaxial Nd:YVO$_4$ crystal the rigorous com-

Table 5.2 – Other parameters used for the resonator setup given in Fig. 5.9. Most of the parameters are based on the description of the experiment performed by Yonezawa et al. [184]. For parameters which where not given explicitly in [184], useful suggestions were made.

Parameter	Value
Refractive index of Nd:YVO$_4$ for ordinary beam	1.9573
Refractive index of Nd:YVO$_4$ for extraordinary beam	2.1652
Nd:YVO$_4$ rod diameter	2 mm
Intracavity aperture diameter	0.630 mm
Refractive index of free space (air)	1.0003
Radius of curvature mirror M$_1$ (concave)	250 mm
Vacuum wavelength of resonator mode	1064 nm
Small signal gain g_0 (according to Eq. (5.3))	2
Gain saturation factor g_1 (according to Eq. (5.3))	$20\ \frac{\mathrm{V}^2}{\mathrm{m}^2}$

ponent operator introduced in section 4.1 is applied. The gain is simulated directly after the anisotropic operator $\boldsymbol{\mathcal{C}}_{\text{aniso}}$ by the thin-sheet gain approximation [140]

$$\boldsymbol{\mathcal{C}}_{\text{AM}} = \begin{pmatrix} \mathcal{C}_{\text{AM}} & 0 \\ 0 & \mathcal{C}_{\text{AM}} \end{pmatrix} \tag{5.2}$$

with

$$\mathcal{C}_{\text{AM}} V_\ell^{+/-} = \exp\left(\frac{g_0}{1 + g_1^{-1} \sum_{\ell=1,2} \left(|V_\ell^+|^2 + |V_\ell^-|^2 \right)} \right) V_\ell^{+/-} \tag{5.3}$$

where the variable dependency (x, y, z) of $V_\ell^{+/-}$ was skipped for a better readability. g_0 is the small signal gain and g_1 is a measurement of the gain saturation. V_ℓ^+ and V_ℓ^- represent the fields propagating in forward and backward direction, respectively. Please note that due to the dependency of $\mathcal{C}_{\text{AM}}$ on both field components given by the nominator of Eq. (5.3), the round trip operator $\boldsymbol{\mathcal{R}}$ is nonlinear. Furthermore the two field components in Eq. (3.12) are coupled by this nonlinearity as well as by the rigorous component operator for the simulation of the Nd:YVO$_4$ crystal.

Please note that in this numerical example an uniaxial anisotropic medium is simulated. However the techniques given in section 4.1 are not limited to uniaxial crystals, but can be also applied to more general anisotropic, homogeneous media, described by an arbitrary dielectric tensor. This example was just chosen due to the existence of a measured reference resonator mode in the literature and the practical relevance of Nd:YVO$_4$ crystals for solid state lasers.

Table 5.3 – Component operators used in different domains of the resonator given in Fig. 5.9. The corresponding equations for the component operators are given in brackets.

Component	Component operator used
Birefringence of Nd:YVO$_4$	$\mathcal{C}_{\text{aniso}}$ (Eqs. (4.1) – (4.27))
Gain of Nd:YVO$_4$	$\mathcal{C}_{\text{AM}}$ (Eq. (5.2))
Aperture	$\mathcal{C}_{\text{TEA}}$ (Eq. (3.25))
Mirrors M$_1$ and M$_2$	$\mathcal{C}_{\text{TEA}}$ (Eq. (3.25))

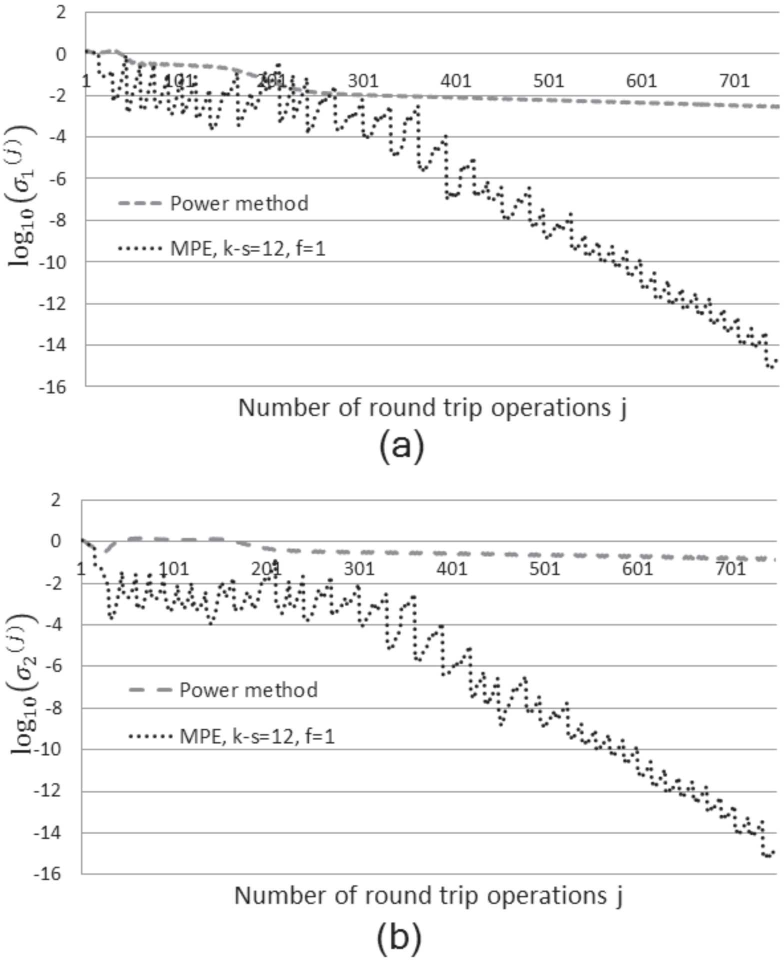

Figure 5.10 – Convergence velocity of MPE and iterative power method for the nonlinear eigenvalue problem describing the resonator in Fig. 5.9. The evolution of the deviation $\sigma_\ell^{(j)}$ between adjacent iteration results for the coupled E_x (a) and E_y (b) field components is shown. Please note that, for better illustration, the vertical axes were scaled logarithmically. This example clearly shows that the MPE algorithm has a much faster convergence velocity than the iterative power method.

Once the eigenvalue problem is formulated, it is solved by the MPE technique in cycled mode using 12 round trip iterations per cycle. The corresponding convergence of the

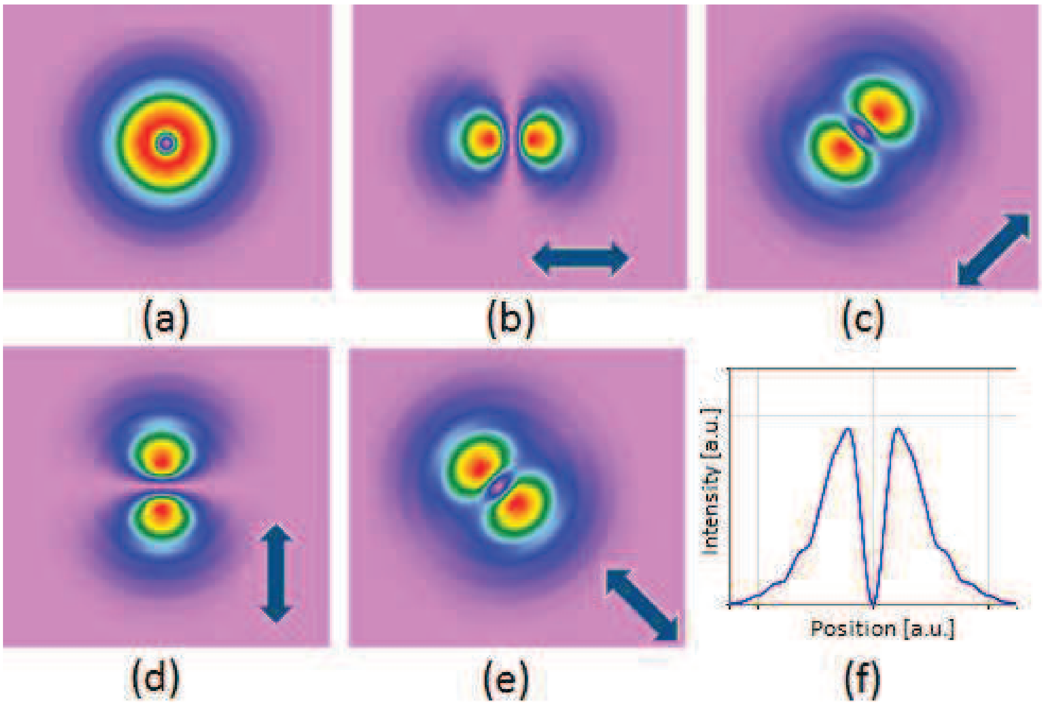

Figure 5.11 – Intensity distributions of the dominant transversal resonator mode in the plane of the outcoupling mirror M_2. (a) Overall intensity distribution. (b)-(e) Intensity distributions after the mode passes through a linear polarizer with different directions. The arrows indicate the directions of the polarizer. (f) Intensity profile along the vertical line intersecting the center of (a). All of the simulation results are in good agreement to measured results given by Yonezawa et al. [184].

algorithm in terms of deviation $\sigma_\ell^{(j)}$ is given in Fig. 5.10 in comparison to the iterative power method. The much faster convergence of the cycled MPE algorithm in comparison to the power method in terms of required round trip iterations can be clearly seen. The calculation was performed on a personal computer with Intel Core$^{\mathrm{TM}}$ i7-4700HQ (8 CPUs @ 2.40GHz). The calculation time per round trip was approximately 36 seconds if 559×559 plane waves in the angular spectrum of plane waves approach given by Eq. (4.2) were used. Consequently the computational grid in the spatial domain consisted also of 559×559 sampling points with an equidistant sampling pitch of 10 microns ×10 microns. The maximum RAM memory requirement during the calculation was approximately 1.3 Gigabyte. Please note that so far no effort was made by the author to accelerate the current code implementation of the algorithms.

The intensity of the dominant transversal resonator mode in the plane of the flat outcoupling mirror is given by Figs. 5.11a) and 5.11f). Its radial polarization is illustrated in Figs. 5.11b) — 5.11e), which show the simulation results of the mode propagation through a linear polarizer with varying direction. Here the Jones matrix according to Eq. (3.34) was used to simulate the effect of the linear polarizer. The shape and polarization properties of the dominant transversal resonator mode are in good agreement with the measured results given in Fig. 3 in [184].

Yonezawa et al. [184] also observed in their experiment that if the effective cavity length is reduced, the ordinary beam and the extraordinary beam are in the stable resonator region, ending up with an unpolarized TEM_{00}-like fundamental mode. Also these results can be reproduced by simulations, by reducing e.g. the distance between the spherical mirror and the aperture from 180 mm to 160 mm in Fig. 5.9. If the cycled MPE is applied again, after 120 round trip iterations a deviation of $\sigma_\ell^{(j)} < 10^{-7}$ is reached. The resulting eigenmode is given in Fig. 5.12 and directly shows a TEM_{00}-like mode. However it is E_x-polarized, which seems to be different to the observation by Yoneszawa et al. [184]. Nevertheless the simulation is indeed correct because of the fact that a monochromatic field is per definition always fully polarized according to Maxwell's equations [30], and thus the coupled eigenvalue problem given by Eq. (3.12) always converges to a polarized eigenmode due to the definition of the eigenvalue problem in terms of a monochromatic field. In addition please note that due to the radial symmetry of the resonator, the choice of the x-y transversal coordinate system is free. Consequently depending on the orientation of the choice of the coordinate orientation the polarization direction of the TEM_{00}-like transversal mode also changes. It is always polarized but the polarization could be along any radial direction. However due to unavoidable fluctuations in practice, the polarization direction may change from one radial direction to the other. That leads to the result that an unpolarized field is observed in the experiment by Yonezawa et al. [184]. Furthermore in Fig. 5.12b) a higher order E_y component is obtained due to the fact that in the resonator geometry the TEM_{00}-like E_x component does not completely fill the active medium volume. Consequently in the active medium regions far away from the optical axis there is still some inversion left, which will amplify the second dominant mode shape. In the experiment this mode shape will also be unpolarized due to the above given arguments. Yonezawa et al. [184] do not mention the appearance of this second dominant mode shape, which might have the following reasons:

1. With decreasing aperture diameter the strength of this second dominant mode decreases, because higher order mode losses are increased. The exact aperture size of the resonator used by Yonezawa et al. is not given in [184]. So it might be that in the experiment an aperture diameter smaller than in these simulations was used, and consequently no second order mode could be observed.

2. In this simulation a homogeneous pump light distribution was assumed, which is of course an approximation of the real experimental pump setup.

3. In Fig. 5.12 it can be seen that the maximum intensity of the TEM_{00}-like mode is much higher than the maximum intensity of the higher order mode. In the experiment it might be very difficult to detect the weak signal of the higher order mode.

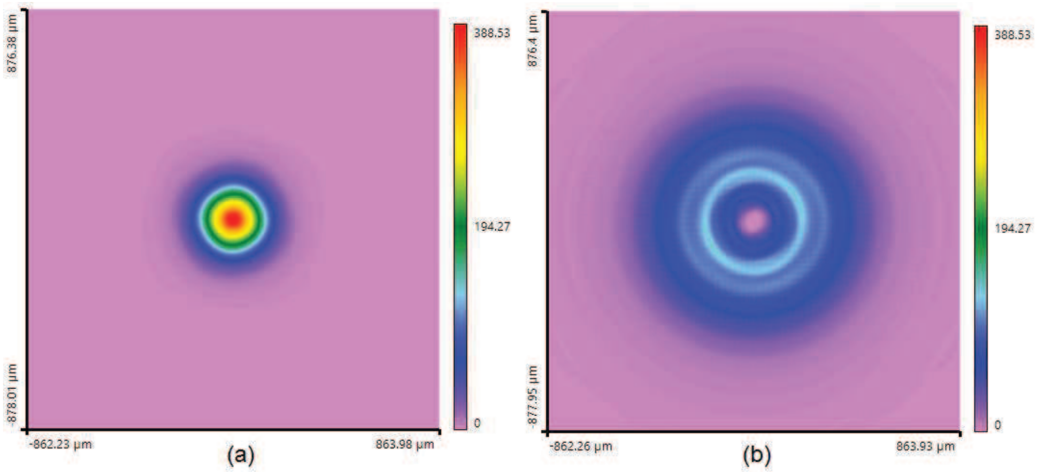

Figure 5.12 – Intensity distribution of the V_1 (a) and V_2 (b) components of the resonator setup given in Fig. 5.9 with reduced effective cavity length obtained by the MPE algorithm after 120 round trip iterations. The different transversal shapes are caused by nonlinear mode competition inside the active medium. Clearly the TEM_{00}-like mode in (a) has a larger amplitude than the higher order mode in (b).

In addition to the above given example another comparison between a simulation based on the generalized Fox-Li algorithm and an experimental measurement gave a good agreement between theory and experiment. Due to the limited number of pages of this thesis, the author decided to publish this conformity of experimental and simulation results of a laser resonator configuration with a discontinuous phase element for forming an azimuthally polarized resonator eigenmode in a separate peer-review article [185].

5.3 Optimization of Resonator with Thermal Lensing, Stress-induced Birefringence and Nonlinear Gain Saturation

In the previous chapters novel concepts for the calculation of the fully vectorial transversal eigenmode of a cw solid-state laser were introduced including nonlinear gain, birefringence and thermal lens effects. In the following these techniques will be applied exemplarily to improve the beam quality and the output power of the cw flash-lamp-pumped Nd:YAG laser given in Fig. 5.13. The laser resonator is a linear cavity consisting of two spherical mirrors M_1 and M_2 with focal lengths $f_{M1} = f_{M2} = 100$ mm. Mirror M_1 is the outcoupling mirror and has a reflectance $R_{M1} = 0.9$. It is desired that the beam quality M^2 emitted

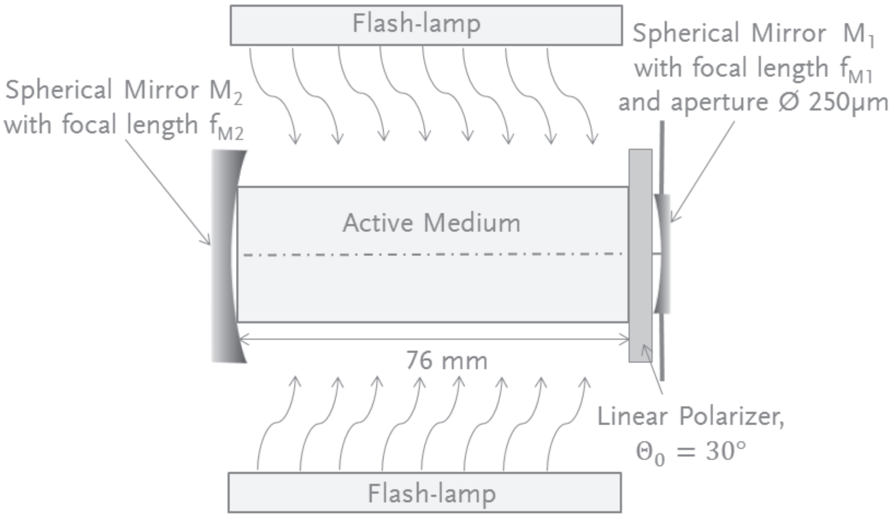

Figure 5.13 – Initial setup 1: solid state laser, consisting of two spherical mirrors M_1 and M_2, a linear polarizer and a flash-pumped Nd:YAG crystal. To suppress higher order modes, an aperture is placed in the plane of the outcoupling mirror M_1. The parameters of the Nd:YAG crystal are given in Table 5.4.

by the laser be close to 1 and that the laser operates only in a single transversal mode. Therefore the circular aperture diameter of mirror M_1 has to be chosen small enough to suppress higher order resonator modes. In this example the circular aperture of mirror M_1 should be 250 microns. All light outside of this aperture is perfectly blocked. Resonator mirror M_2 has a sufficiently large aperture size and a reflectance of $R_{M2} = 1$ to ensure that it is not introducing any additional resonator losses. It is desired that the emitted light is perfectly linearly polarized under an angle $\theta_0 = \arcsin(y/x) = 30°$. Therefore a linear wire-grid polarizer is placed directly in front of the outcoupling mirror. The polarizer is orientated under an angle of 30° generating the requested linear polarization direction. The thickness of the polarizer can be neglected, so that the length of the resonator is 76 mm. The active medium is a Nd:YAG crystal, with the same parameters and flash-pump as discussed in [16, 182]. The parameters of the active medium are given in Table 5.4. Please note that the pump efficiency is not equal to the pump quantum efficiency. The pump efficiency is the fraction of the electric power of the flash lamps which is converted into stimulated emission. It is calculated by the multiplication of the first three efficiencies given in Table 1 of [182]. The active medium and two flash-lamps are placed in a double-elliptical cylinder to ensure a high pump-transfer efficiency and a homogeneous pump distribution in the active medium [16, 182]. For simplicity, in the following it is assumed that the heat which is dissipated in the active medium is homogeneously distributed over the whole active medium and an annular cooling configuration is used. Also the pump power is homogeneously distributed over the whole Nd:YAG rod. Please note that these assumptions in principle are not necessary to apply the concepts described in the previous sections. However the assumptions are pretty realistic for the flash-lamp double-elliptical pump configuration, ending up with the following cylindrical temperature distribution within the active medium [182]

Table 5.4 – Parameters of the Nd:YAG active medium. If no extra citation is given for the parameter, its value was taken from Koechner [16, 182].

Parameter	Value
crystal orientation	[111]
crystal length L	76 mm
circular crystal rod diameter d	6.35 mm
linear refractive index $n_{\mathrm{Nd:YAG}}$ @ 1064 nm	1.82
total electric power of flash lamps P_{e}	12 kW
temperature in the rod center $T(0)$	114°C
temperature at the rod surface $T(0.5d)$	57°C
first order thermal dependence of refractive index $\mathrm{d}n/\mathrm{d}T$ [175]	7.3×10^{-6} 1/°C
average-lifetime at upper laser level $\tau = (1/\tau_{21} + 1/\tau'_{20})^{-1}$ [4]	230×10^{-6}s
cross-section σ_{12} [4]	2.8×10^{-19} cm^2
pump efficiency η_{pe}	3%
wavelength of resonator mode λ_{L}	1064 nm
energy difference between upper laser level and ground level $h\nu_{20}$ [4]	2.1147×10^{-19}J
thermal expansion α	7.9×10^{-6} 1/°C
thermal conductivity $\hat{k}$	0, 111W/(cm °C)
poisson ratio $\hat{\nu}$	0.3
photoelastic tensor coefficients p_{1111}	−0.029
photoelastic tensor coefficients p_{1122}	0.009
photoelastic tensor coefficients $p_{3232} = p_{2323} = p_{3223} = p_{2332}$	−0.0615

$$T(\boldsymbol{\rho}) = T(0) - \frac{|\boldsymbol{\rho}|^2}{(0.5d)^2}\,[T(0) - T(0.5d)] \tag{5.4}$$

with the temperature in the rod center $T(0)$ and at the rod surface $T(0.5d)$ given in Table 5.4. Plugging Eq. (5.4) into Eq. (4.52) and using the values for $\mathrm{d}n/\mathrm{d}T$ given in Table 5.4 results in a thermal lens of

$$\Delta n^{\mathrm{therm}}_{\alpha'\alpha'}(\boldsymbol{\rho}) = -41.277\ \mathrm{m}^{-2} \times |\boldsymbol{\rho}|^2. \tag{5.5}$$

Furthermore Eq. (5.4) can be used to solve the eigenvalue problem given by Eq. (4.56), ending up with azimuthally stress-induced birefringence [16]. Then the nonlinear operator in Eq. (4.57) has the form [83]:

$$\boldsymbol{\mathcal{C}}_s^{\mathrm{NL}} = \begin{pmatrix} \cos\theta & -\sin\theta \\ \sin\theta & \cos\theta \end{pmatrix} \begin{pmatrix} \mathcal{C}_{11,s}^{\mathrm{NL}} & 0 \\ 0 & \mathcal{C}_{22,s}^{\mathrm{NL}} \end{pmatrix} \begin{pmatrix} \cos\theta & \sin\theta \\ -\sin\theta & \cos\theta \end{pmatrix} \tag{5.6}$$

with the azimuthal angle θ and the contributions of the stress-induced birefringence on the refractive index:

$$\Delta n_{11}^{\mathrm{birefring}}(\boldsymbol{\rho}, \boldsymbol{V}) = \frac{-\alpha\nu n_{\mathrm{Nd:YAG}}^3 \left[T(0) - T(0.5d)\right]}{6(1-\nu)(0.5d)^2} \left(p_{1111} - p_{1122} + 4p_{3232}\right) |\boldsymbol{\rho}|^2 \tag{5.7}$$

and $\Delta n_{22}^{\mathrm{birefring}} = 0$.

Due to the broad spectrum of pump light emitted by the flash lamps, several pump levels are used to fill the upper laser level. Therefore the small-signal gain g_0 in Eq. (4.44) can be expressed by [4]

$$g_0 = \frac{\eta_{\mathrm{pe}} P_{\mathrm{e}} \tau \sigma_{12}}{\pi (0.5d)^2 L h \nu_{20}}. \tag{5.8}$$

To calculate the dominant eigenmode of the above given example resonator setup the eigenvalue problem given by Eq. (3.12) is solved using the minimal polynomial extrapolation method (MPE) and a random phase distribution as initial condition. The active medium was simulated by the vBPM given in section 4.2. Therefore the crystal was discretized in z-direction in 30 slabs. The mirrors were simulated by the TEA (Eq. (3.3)) and the linear polarizer by the Jones matrix according to Eq. (3.34). The E_x and E_y polarization components of the dominant transversal laser resonator mode in two different planes in the resonator are given in Fig. 5.14. The output power of the beam is 0.19 W. Furthermore the second-order momenta method [83] has been applied on the transversal mode to calculate the beam quality in the plane of the outcoupling mirror. It is $M_x^2 = M_y^2 = 2.8$ in x- and y-direction, respectively. If the transversal mode structure and power are analyzed at different positions in the laser cavity, it can be seen that there are significant depolarization losses at the linear polarizer and diffraction losses at the aperture of the outcoupling mirror. The corresponding values are given in Table 5.5.

In a next step the diffraction losses are improved by compensating the thermal lens of the active medium. Therefore the resonator setup is rearranged. The spherical outcoupling mirror is replaced by a plane mirror with reflectance $R = 0.9$ and in addition a Fourier lens in combination with an aspherical mirror is used as shown in Fig. 5.15. In principle this setup is a stable Fourier transform resonator [83]. To suppress the higher order resonator modes in an efficient way, a smaller mirror aperture is used. It's size is chosen to be equal to the 0-th order diameter of the Airy pattern which is obtained in the focal region of the

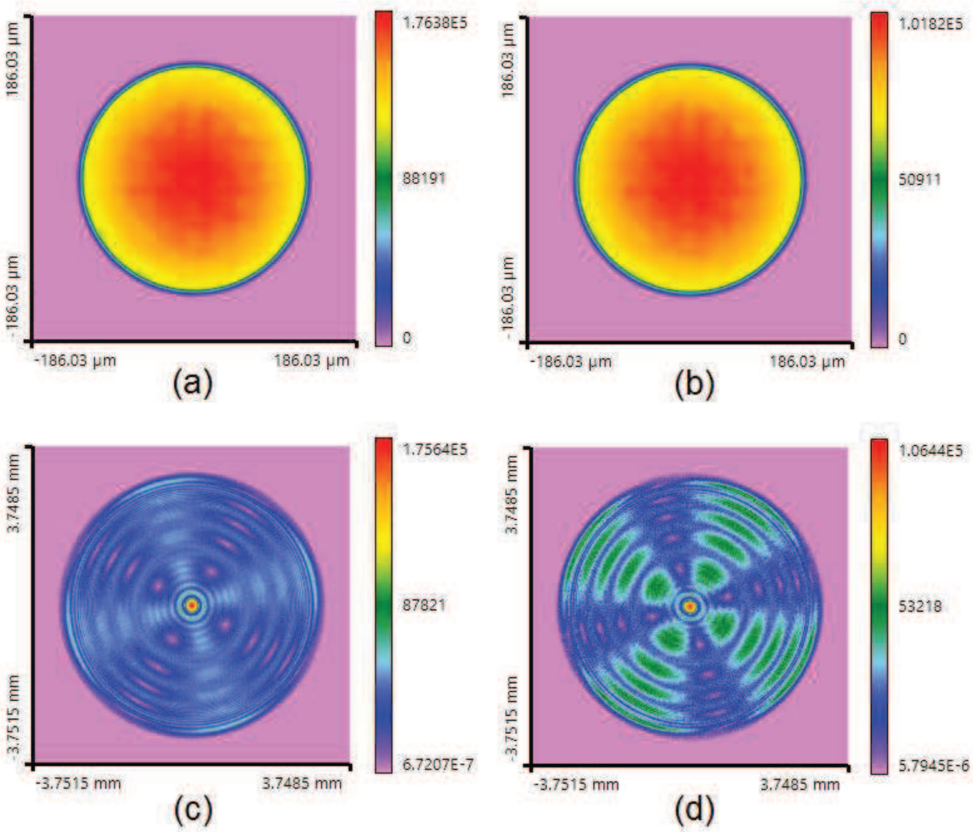

Figure 5.14 – Dominant transversal eigenmode of the laser resonator setup given in Fig. 5.13. The upper row shows the V_1 (a) and V_2 (b) field components of the mode in the plane of the outcoupling mirror M_1. The lower row shows the V_1 (c) and V_2 (d) field components of the mode in the transversal plane between the active medium and the linear polarizer. In both rows the propagation direction of the mode is towards the outcoupling mirror and the fundamental transversal eigenmode has a non-Gaussian shape due to birefringence, diffraction and thermal lensing effects.

Fourier lens, if the Fourier lens is illuminated by an ideal plane wave [83]. The aspherical mirror compensates the wavefront deformations caused by thermal lensing. Thus it can be interpreted as a static phase conjugating mirror for a specific resonator mode. For the design of the aspherical surface of the mirror the vBPM operator is used in the following steps, which are based on the ideas given in [186]:

1. A fundamental Gaussian beam with waist position in the outcoupling mirror plane is used as starting condition. The waist diameter is equal to the aperture diameter of the mirror M_1.

2. The vBPM operator and the other component and free-space operators mentioned below are applied to propagate the Gaussian beam to a plane in the desired aspherical mirror position z_0. Then the phase $\Phi(x, y, z_0)$ of the propagated field is calculated in this plane.

3. After that the phase of the field is conjugated: $\Phi(x, y, z_0) \rightarrow \Phi^*(x, y, z_0)$

Table 5.5 – Output power and beam quality of laser resonator setups 1-3. The depolarization loss and the diffraction loss are defined by the ratio of the beam power before and after the polarizer and mirror aperture, respectively.

Resonator setup	Maximum power in cavity	Depolarization loss	Diffraction losses at mirror M_2 aperture	Laser output power	Beam quality M_x^2, M_y^2 in the plane of M_2
Setup 1: w/o compensation	107.5 W	25.8%	97.6%	0.19 W	2.8 , 2.8
Setup 2: with thermal lens compensation	247.0 W	25.2%	40.9%	10.9 W	1.1 , 1.1
Setup 3: with thermal lens and birefringence compensation	779.7 W	0.7%	7.9%	71.4 W	1.3 , 1.2

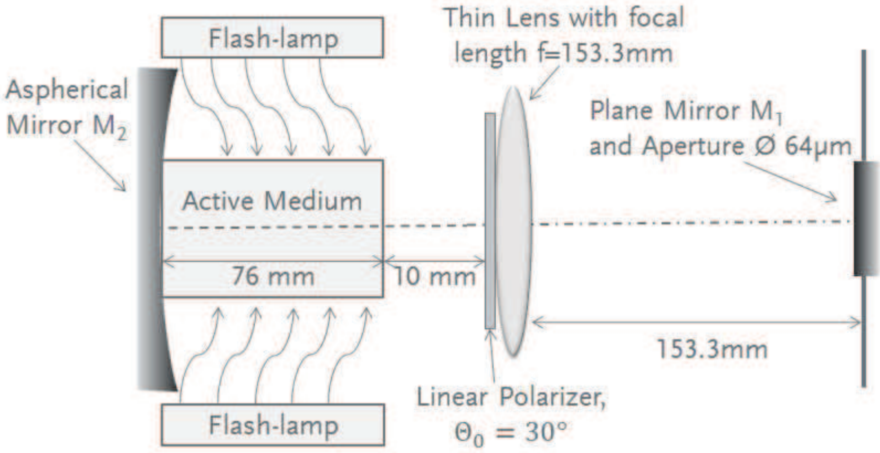

Figure 5.15 – Resonator setup 2 with thermal lens compensation: a stable Fourier transform resonator geometry is used to improve the beam quality and output power. To ensure that the thermal lens in the flash-pumped Nd:YAG laser is compensated an aspherical mirror was designed. The parameters of the Nd:YAG crystal are the same as in the initial setup.

4. Due to the fact that the beam in the resonator has to pass the active medium twice in a full round trip, the transmission function of the aspherical mirror must be $t(x, y, z_0) = \exp(\mathrm{i}2\Phi^*(x, y, z_0))$.

5. TEA is applied to calculate the height profile $h(x, y)$ of the mirror for the specific mode wavelength: $h(x, y) = [\lambda/(4\pi)]2\Phi^*(x, y, z_0)$.

Once the aspherical surface is designed, again the round trip operator concept in combination with the vBPM is applied to calculate the dominant resonator eigenmode. For the

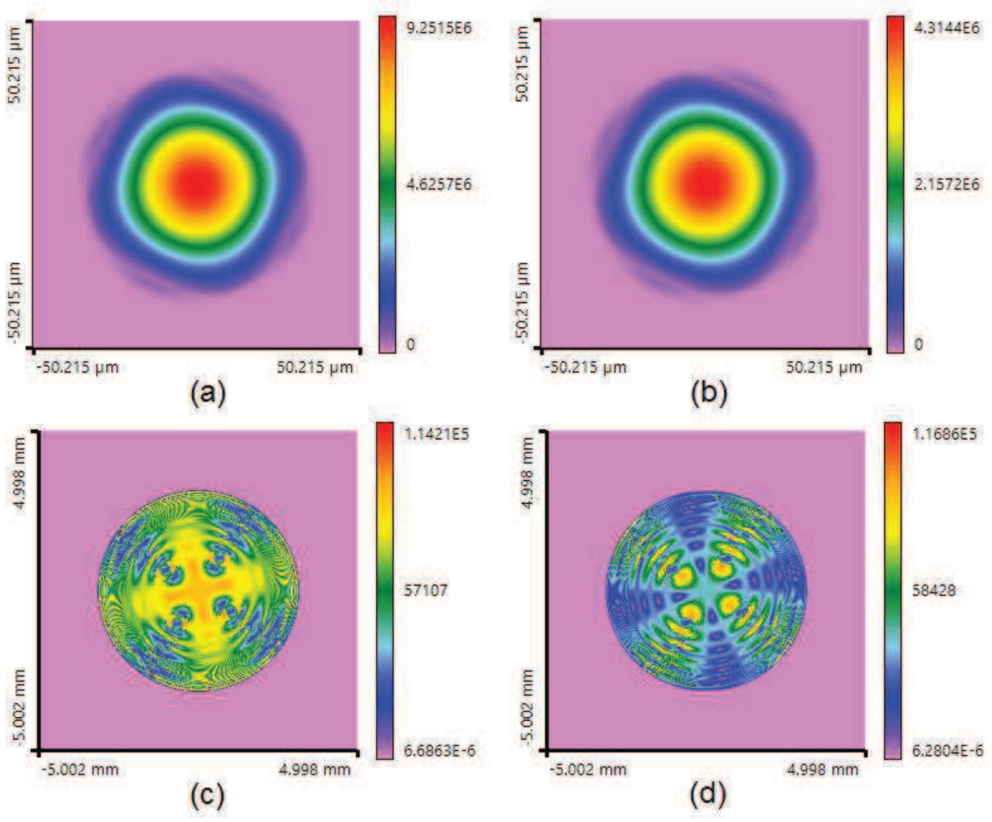

Figure 5.16 – Dominant transversal eigenmode of the laser resonator setup 2 given in Fig. 5.15. The upper row shows the V_1 (a) and V_2 (b) field components of the mode in the plane of the outcoupling mirror M_1. The lower row shows the V_1 (c) and V_2 (d) field components of the mode in the plane behind the active medium, next to the linear polarizer. In both rows the propagation direction of the mode is towards the outcoupling mirror.

free-space propagation the SPW operator given by Eqs.(2.30) and (2.31) is used. The thin Fourier lens, the plane mirror and the aspherical mirror are simulated by TEA (Eq. (3.3)). The polarizer is simulated again by the Jones matrix according to Eq. (3.34). Fig. 5.16 shows the dominant eigenmode at two different positions in the resonator. The output power of the beam could be improved to 10.9 W and the beam quality to $M_x^2 = M_y^2 = 1.1$. As shown in Table 5.5 the polarization losses are still pretty high. Consequently the resonator setup has to be modified further to reduce the polarization losses.

To that end a 90° quartz polarization rotator is used as described in [20] ending up with the resonator setup given in Fig. 5.17. The quartz rotator and the linear polarizer are simulated by Jones matrices (Eqs. (3.37) and (3.34)) and the lenses and mirrors by TEA (Eq. (3.3)). Again MPE is used to solve the eigenvalue problem. The corresponding transversal eigenmode is given in two different planes in Fig 5.18. Clearly the depolarization loss could be decreased by this resonator setup. The improved outcoupling power and beam quality of the laser are given in Table 5.5.

Due to the nonlinear gain saturation effects, it is expected that a change of the resonator round trip loss has an influence on output beam quality and power. Therefore the

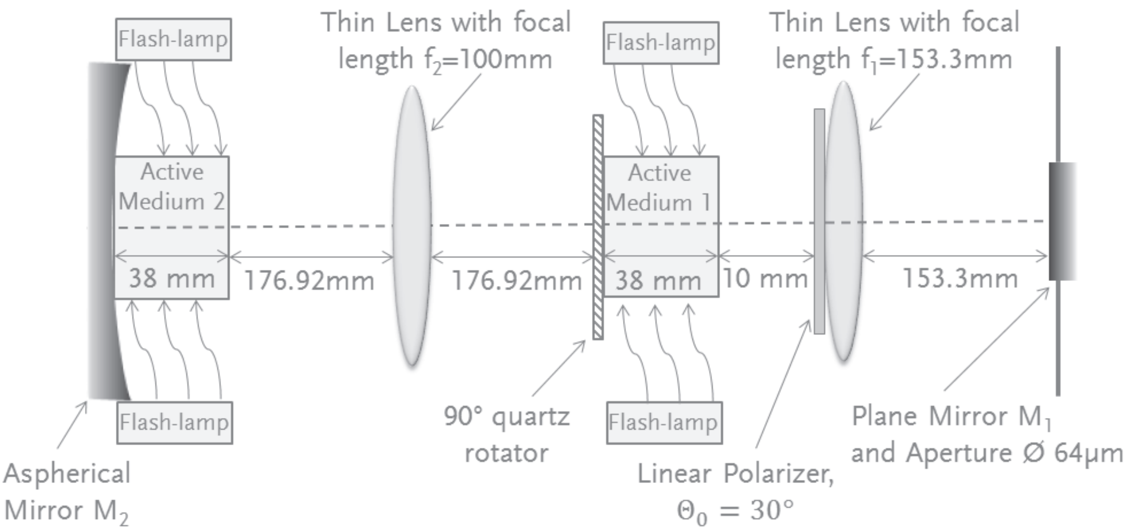

Figure 5.17 – Resonator setup 3 with thermal lens and birefringence compensation: a stable Fourier transform resonator geometry is used to improve the beam quality and output power. To ensure that the thermal lens in the flash-pumped Nd:YAG laser is compensated an aspherical mirror was designed. The initial Nd:YAG crystal is split into two rods with equal length and optical pump. Stress-induced birefringence is compensated by placing a 90° quartz polarization rotator and a thin lens between the two Nd:YAG crystals.

reflectance of the outcoupling mirror is varied between 0.3 and 0.99. The resulting values of the output beam power are given in Fig. 5.19. Two local maxima can be clearly seen. This is caused by the nonlinear behavior of the active medium. Furthermore this nonlinear gain saturation has an influence on the beam quality as shown in Fig. 5.20. For a homogeneous pump light distribution the transversal resonator mode will be more strongly amplified in regions far away from the optical axis than in its center. Thus the mode is spatially deformed during its propagation through the active medium. That is why the mode given in Fig. 5.20 b) obtained for $R = 0.4$ ($M_x^2 = 1.4, M_y^2 = 1.3$) has a poorer beam quality than the mode of Fig. 5.20 a) obtained for $R = 0.7$ ($M_x^2 = 1.3, M_y^2 = 1.2$). Consequently for setup 3, given above, the initial plane outcoupling mirror with $R = 0.9$ should be replaced by a mirror with $R = 0.7$ to improve the output power further. For $R = 0.7$ there is no significant change of the beam quality M^2 compared to the setup with $R = 0.9$.

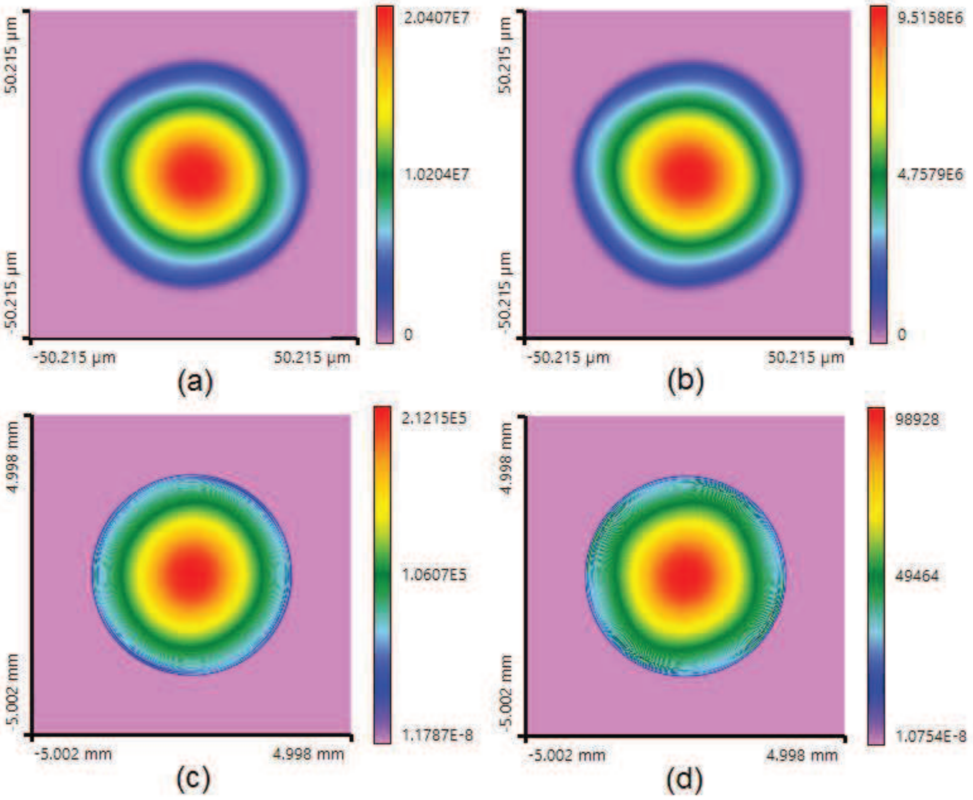

Figure 5.18 – Dominant transversal eigenmode of the laser resonator setup 3 given in Fig. 5.17. The upper row shows the V_1 (a) and V_2 (b) field components of the mode in the plane of the outcoupling mirror M_1. The lower row shows the V_1 (c) and V_2 (d) field components of the mode in the plane behind the active medium 1 next to the linear polarizer. In both rows the propagation direction of the mode is towards the outcoupling mirror.

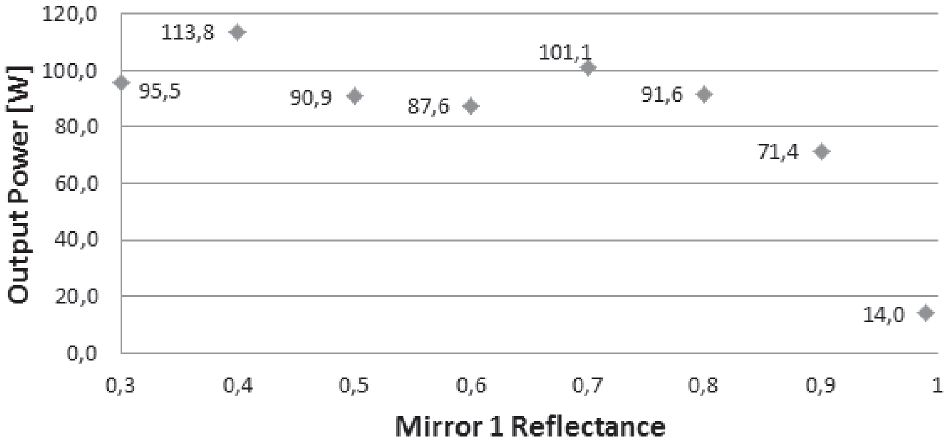

Figure 5.19 – Variation of the reflectance R of the outcoupling mirror M_1 used in the resonator setup 3. Due to nonlinear gain saturation effects, which are included in the vBPM simulation, the output beam power changes with the reflectance. Two local power maxima are obtained for $R = 0.4$ and $R = 0.7$, respectively. Thus replacing the initial plane outcoupling mirror with $R = 0.9$ by a mirror with $R = 0.7$ will further improve the beam output power.

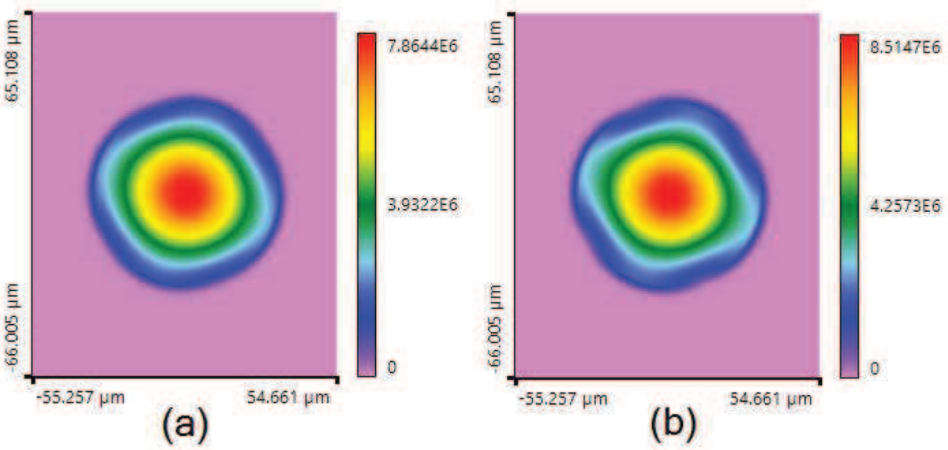

Figure 5.20 – E_x field components of the dominant transversal eigenmode for outcoupling mirror reflectance $R = 0.7$ (a) and $R = 0.4$ (b). Due to nonlinear gain saturation effects, the beam is slightly aberrated ending up with $M_x^2 = 1.3, M_y^2 = 1.2$ for a) and $M_x^2 = 1.4, M_y^2 = 1.3$ for b). Please note that the given field distributions are calculated in the aperture of the outcoupling mirror, where the light is linearly polarized. Thus the corresponding E_y field components have a similiar shape as the shown E_x components.

Chapter 6

Outlook

In this thesis it was shown that the eigenvalue problem given by Eq. (3.12) has to be solved for the calculation of the dominant transversal resonator mode of lasers oscillating in single transversal mode operation. In multi-transversal-mode operation all different transversal resonator modes experience amplification in the same active medium. This leads to the so called mode competition [71], where stimulated emission by one mode causes gain saturation not only for itself, but also for the other modes. This mode competition, which has an important influence on the power and shape of the transversal modes of a laser in multi-transversal-mode operation, is not included in the problem formulation of Eq. (3.12). Thus in the case of mode competition the solution of Eq. (3.12) might not represent one of the actual resonator modes oscillating in the cavity. However please note that this fact is not caused by any shortcomings of the eigenvalue solvers, but simply by a restriction of the problem formulation given by Eq. (3.12). In the following the problem formulation of Eq. (3.12) is extended in a way that allows mode competition to be included for the simulation of lasers in multi-transversal-mode operation. A similar extension has been done in [106, 107] for the scalar Fox and Li algorithm. Starting from the reasonable assumption that each transversal resonator mode is incoherent to each other [81], the total intensity of all modes inside a laser resonator can be written as an incoherent sum:

$$I_{\text{total}}^{+/-}(x,y,z) = \sum_i I_i^{+/-}(x,y,z) \tag{6.1}$$

with $I_i^{+/-}(x,y,z)$ being the intensity of a single transversal mode with index i propagating in positive (+) or negative (−) direction, respectively. The relation between $I_i^{+/-}(x,y,z)$ and the corresponding fully vectorial, electromagnetic field of the single mode $V_{\ell,i}^{+/-}(x,y,z)$ is given in paraxial approximation by Eq. (2.69). Again it is assumed that only a single axial mode is oscillating in the cavity. Due to the mutual incoherence of the transversal modes, the propagation of each resonator mode along the resonator round trip can be described by:

$$\begin{pmatrix} \gamma_{1,i} & 0 \\ 0 & \gamma_{2,i} \end{pmatrix} \begin{pmatrix} V_{1,i} \\ V_{2,i} \end{pmatrix} = \boldsymbol{\mathcal{R}}_i \left(\boldsymbol{V}_1, \boldsymbol{V}_2, ... \boldsymbol{V}_i \right) \begin{pmatrix} V_{1,i} \\ V_{2,i} \end{pmatrix} = \begin{pmatrix} \mathcal{R}_{11,i} & \mathcal{R}_{12,i} \\ \mathcal{R}_{21,i} & \mathcal{R}_{22,i} \end{pmatrix} \begin{pmatrix} V_{1,i} \\ V_{2,i} \end{pmatrix} . \tag{6.2}$$

Please note that Eq. (6.2) can be interpreted as a set of i eigenvalue problems. For each eigenvalue problem there can be a coupling between the $V_{1,i}$ and $V_{2,i}$ field components by a non-diagonal round trip operator $\boldsymbol{\mathcal{R}}_i$. Furthermore due to mode competition, there is also a nonlinear coupling between the different eigenvalue problems, ending up with a nonlinear round trip operator $\boldsymbol{\mathcal{R}}_i \left(\boldsymbol{V}_1, \boldsymbol{V}_2, ..., \boldsymbol{V}_i \right)$, depending on all field components $V_{\ell,i}(x, y, z)$ of all modes i. In the case of mode competition in a cw solid state laser with homogeneously broadened 4-level energy system the nonlinear gain saturation can be modeled approximately by

$$g \approx \frac{g_0}{1 + \frac{I^{+}_{\text{total}} + I^{-}_{\text{total}}}{I^{\text{L}}_{\text{s}}}} \sigma_{12} N \ , \tag{6.3}$$

which is similar to the expression given in Eq. (2.76), except for the fact that the intensity of a single mode was replaced by the incoherent sum of all mode intensities given by Eq. (6.1). For the light propagation through the active medium again a vBPM or a thin-sheet gain approximation as it was applied in section 5.2 can be formulated. Please also note that the simulation of mode competition is only useful if the active medium inside the resonator is included in the simulation. Thus following the same arguments as in section 3 $|\gamma_{1,i}|$ and $|\gamma_{2,i}|$ will be always 1. Please note that in future work the applicability of suitable eigenvalue solvers for the set of equations given by Eq. (6.2) has to be tested. For the scalar case the iterative power method was successfully applied in [106, 107]. So it might also be the first candidate for solving Eq. (6.2). Good techniques for solving Eq. (6.2) might be the MPE and RRE, which might give better convergence speeds compared to the iterative power method. However even if vector extrapolation methods are applied, the computational effort might be very high for laser resonators oscillating with plenty of different transversal modes. Consequently additional research should be done to accelerate the calculation time of a single round trip operation $\boldsymbol{\mathcal{R}}_i$. Nevertheless all comments of this chapter are recommendations for future research this thesis is definitely the basis for.

Chapter 7

Summary

For plenty of applications modern cw solid-state lasers should provide a high output beam power, good beam quality ($M^2 \approx 1$) and customized light polarization. Therefore nowadays plenty of different optical components are used inside the laser resonator to control its dominant transversal mode. Thus there is an enormous degree of design freedoms, requiring computer-aided design, tolerancing and analysis tools. The most fundamental of all of these tools is a flexible and fast simulation technique for the modeling of laser resonators. State-of-the-art simulation approaches given in literature are limited either by their low simulation accuracy, their high numerical effort and/or their limited scope of applicability to a few special resonator geometries and intracavity components. Even the well-known scalar Fox-Li algorithm is limited to the simulation of paraxial transversal modes of resonators consisting only of linear, isotropic and thin elements, due to its scalar approximation.

Thus in this work the Fox-Li algorithm was generalized to a fully vectorial approach using the concepts of field tracing. Therefore the resonator was subdivided in several subdomains. In each of the subdomains the light propagation was described by a fully vectorial harmonic field using approximative or rigorous solutions of Maxwell's equations. In principle any simulation technique known from literature which can be applied to propagate harmonic fields can be used. Between the subdomains rigorous or approximative diffraction integrals can be solved to propagate the light in free-space. This flexible combination of different techniques for the propagation in free-space and in the subdomains (also called component operators) ends up with a fully vectorial eigenvalue problem, which has to be solved to calculate the dominant transversal resonator mode of lasers oscillating in single transversal-mode operation. It was discussed in detail that the structure of the eigenvalue problem and its corresponding solution type depend on the approximation level used for the free-space propagation and component operators. On the one hand, if polarization cross-talk effects are neglected in the entire resonator, there is a decoupling between the field components of the resonator mode, ending up with two separate eigenvalue problems.

On the other hand if the simulation is done with a higher accuracy, meaning that polarization cross-talk effects are included at least in a single subdomain of the resonator, there is a coupled eigenvalue problem to be solved.

Furthermore it was shown that independently of its structure, the eigenvalue problem can be solved by the iterative power method. However as shown in two examples, this approach might suffer from low convergence velocity, resulting in a high numerical effort. Thus two vector extrapolation methods, namely the RRE and the MPE, were applied the first time in the context of laser resonator simulations to significantly improve the convergence velocity and the numerical effort.

Anisotropic intra-cavity crystals play a major role in manipulating the polarization state of light emitted by the laser. Therefore in this work a rigorous component operator for the propagation of light through anisotropic, homogeneous and linear media was introduced. It is based on the decomposition of a general harmonic field into a set of plane waves using the numerically efficient FFT. Each of the plane waves is propagated separately through the bi- or uniaxial crystal, including the refraction effects at the crystal interfaces. After the propagation of the plane waves through the crystal, they are superimposed again behind the crystal using the superposition principle formulated by an FFT algorithm. In addition an approximative component operator for the light propagation through inhomogeneous and birefringent active laser crystals was given. This approach is a FFT-based split-step vBPM, which enables the simulation of thermal lensing as well as stress-induced birefringent effects caused by the active medium. In a lot of solid-state lasers these two effects have negative influence on the resonator performance. Furthermore it was shown how different energy-level diagrams for different active media can be included in the vBPM to simulate nonlinear gain saturation effects. For strong nonlinear gain saturation effects, which dominate the numerical effort of the vBPM, a semi-analytical approach was given to further accelerate the simulation.

Finally several numerical examples were given, showing the application of the above given concepts. Therefore a cw Nd:YAG laser, suffering from thermal lensing, stress-induced birefringence and nonlinear gain saturation was improved in terms of output power, beam quality and depolarization losses. The reliability of the novel simulation techniques was demonstrated by comparing simulation and experimental results which are in good agreement to each other.

Appendix A

Scalar Field Approximation of Maxwell's Equations

The scalar Fox-Li algorithm discussed in section 2.3 is based on an approximated solution of Maxwell's equations using the concept of scalar fields. This approximation is the major constraint on the applicability of the round trip propagation integral kernel K^{Round} in Eq. (2.42) or the round trip propagation operator $\mathcal{R}$ in 2.46, respectively. In this appendix the approximations, which are necessary to introduce the concepts of scalar fields, are shown and their consequences for the simulation of different intracavity optical components are discussed.

Starting from Maxwell's equations given by Eqs. (2.1) – (2.4) the following equations for a single harmonic field defined by Eq. (2.14) can be obtained by using the assumption of linear and isotropic matter response [30]:

$$\nabla \times \boldsymbol{H}(\boldsymbol{r},\omega_0) = -\mathrm{i}\omega_0 \epsilon(\boldsymbol{r},\omega_0)\boldsymbol{E}(\boldsymbol{r},\omega_0), \tag{A.1}$$

$$\nabla \times \boldsymbol{E}(\boldsymbol{r},\omega_0) = \mathrm{i}\omega_0 \mu_0 \boldsymbol{H}(\boldsymbol{r},\omega_0), \tag{A.2}$$

$$\nabla \cdot (\epsilon(\boldsymbol{r},\omega_0)\boldsymbol{E}(\boldsymbol{r},\omega_0)) = 0, \tag{A.3}$$

$$\nabla \cdot \boldsymbol{H}(\boldsymbol{r},\omega_0) = 0. \tag{A.4}$$

With the help of the the vector identity $\nabla \times (\nabla \times \boldsymbol{E}) = \nabla(\nabla \cdot \boldsymbol{E}) - \nabla^2 \boldsymbol{E}$, Eq. (A.1) and Eq. (A.2) can be combined to

$$\nabla(\nabla \cdot \boldsymbol{E}(\boldsymbol{r},\omega_0)) - \nabla^2 \boldsymbol{E}(\boldsymbol{r},\omega_0) = \omega_0^2 \mu_0 \epsilon(\boldsymbol{r},\omega_0)\boldsymbol{E}(\boldsymbol{r},\omega_0). \tag{A.5}$$

Furthermore Eq. (A.3) can be rewritten to

$$\nabla \cdot \boldsymbol{E}(\boldsymbol{r}, \omega_0) = -\frac{\nabla \epsilon(\boldsymbol{r}, \omega_0) \cdot \boldsymbol{E}(\boldsymbol{r}, \omega_0)}{\epsilon(\boldsymbol{r}, \omega_0)} \tag{A.6}$$

Substituting Eq. (A.6) into Eq. (A.5) leads to

$$\nabla \left(-\frac{\nabla \epsilon(\boldsymbol{r}, \omega_0) \cdot \boldsymbol{E}(\boldsymbol{r}, \omega_0)}{\epsilon(\boldsymbol{r}, \omega_0)} \right) = \nabla^2 \boldsymbol{E}(\boldsymbol{r}, \omega_0) + \frac{\omega_0^2}{c_0^2} \epsilon_r(\boldsymbol{r}, \omega_0) \boldsymbol{E}(\boldsymbol{r}, \omega_0) \tag{A.7}$$

where the relation $\epsilon(\boldsymbol{r}, \omega_0) = \epsilon_0 \epsilon_r(\boldsymbol{r}, \omega_0)$ with the vacuum permittivity ϵ_0 and the relative permittivity $\epsilon_r(\boldsymbol{r}, \omega_0)$ was used. Now the scalar approximation can be introduced. Therefore it is assumed that the electric field can be described by a position independent 3-dimensional Jones vector $\boldsymbol{J} = (J_x, J_y, J_z)^{\mathrm{T}}$ and a scalar field $U(\boldsymbol{r}, \omega_0)$ describing the lateral properties of the electric field:

$$\boldsymbol{E}(\boldsymbol{r}, \omega_0) \approx U(\boldsymbol{r}, \omega_0) \boldsymbol{J} \tag{A.8}$$

Thus in the scalar approximation the polarization and the spatial properties of the electric field are separated. Furthermore to fulfill Eq. (A.8) the Jones vector components J_x, J_y and J_z must be independent to each other and consequently polarization cross talk effects are neglected. Substituting Eq. (A.8) in the right hand side of Eq. (A.7) leads to:

$$\nabla \left(-\frac{\nabla \epsilon(\boldsymbol{r}, \omega_0) \cdot \boldsymbol{E}(\boldsymbol{r}, \omega_0)}{\epsilon(\boldsymbol{r}, \omega_0)} \right) = \nabla^2 U(\boldsymbol{r}, \omega_0) \boldsymbol{J} + \frac{\omega_0^2}{c_0^2} \epsilon_r(\boldsymbol{r}, \omega_0) U(\boldsymbol{r}, \omega_0) \boldsymbol{J} \tag{A.9}$$

The independence of the Jones vector components with respect to each other is guaranteed if the left hand side of Eq. (A.9) is zero. Thus to apply the scalar Fox-Li algorithm, the resonator system has to fulfill the following condition:

$$\nabla \left(-\frac{\nabla \epsilon(\boldsymbol{r}, \omega_0) \cdot \boldsymbol{E}(\boldsymbol{r}, \omega_0)}{\epsilon(\boldsymbol{r}, \omega_0)} \right) \overset{!}{=} (0, 0, 0)^{\mathrm{T}}. \tag{A.10}$$

Here the intracavity components and geometries of the resonator mirrors are described by $\epsilon(\boldsymbol{r}, \omega_0)$ and the possible solutions of the transversal mode are given by $\boldsymbol{E}(\boldsymbol{r}, \omega_0)$. Please note that the notation in Eq. (A.10) represents three equations given by the three vector components. By the use of the chain rule the derivatives of the first component can be rewritten into:

$$\begin{aligned} &\left[(\partial_x^2 \epsilon_r) \epsilon_r E_x + (\partial_x \partial_y \epsilon_r) \epsilon_r E_y + (\partial_x \partial_z \epsilon_r) \epsilon_r E_z + (\partial_x \epsilon_r)^2 E_x + (\partial_x \epsilon_r)(\partial_y \epsilon_r) E_y + (\partial_x \epsilon_r)(\partial_z \epsilon_r) E_z\right] \\ &+ \left[(\partial_x \epsilon_r)(\partial_x E_x) + (\partial_y \epsilon_r)(\partial_x E_y) + (\partial_z \epsilon_r)(\partial_x E_z)\right] \overset{!}{=} 0 \end{aligned} \tag{A.11}$$

where the short notation $\partial_a = \frac{\partial}{\partial a}$ with $a = x, y, z$ was used for the derivatives. The resulting equations for the second and third vector component of Eq. (A.10) have a similar structure as Eq. (A.11). Thus Eq. (A.10) is approximately fulfilled if the optical setup of the resonator only consists of thin elements, meaning that $(\partial_a \partial_b \epsilon_r) \approx 0$ for $a, b = x, y, z$. In this case all terms of the sum inside the first square brackets in Eq. (A.11) (and the similarly structured equations for the second and third vector components) are approximately zero. However due to the terms of the sum inside the second square brackets, there must also be a restriction on paraxial fields propagating through the thin optical elements, so that $(\partial_b \epsilon_r)(\partial_a E_b) \approx 0$. Please note that strictly speaking the restriction to paraxial fields is also required due to the fact that for realistic transversal modes inside a laser resonator the independence of the Jones vector components with respect to each other in Eq. (A.8) can be only fulfilled for $J_z \approx 0$, due to the dependence of E_z on E_x and E_y given by Eq. (2.33). Consequently the scalar Fox-Li algorithm can only calculate paraxial transversal resonator modes in laser resonators made of thin elements. In this case Eq. (A.10) is fulfilled, and the light propagation inside the resonator is described by the scalar, inhomogeneous wave equation

$$\nabla^2 U(\boldsymbol{r}, \omega_0) + \frac{\omega_0^2}{c_0^2} \epsilon_r(\boldsymbol{r}, \omega_0) U(\boldsymbol{r}, \omega_0) = 0 \tag{A.12}$$

which was obtained from Eqs. (A.9) and (A.10).

Appendix B

Stationary Solution of Rate Equations for Various Laser Energy Systems

It was shown in section 2.4 that Maxwell's equations are connected to the rate equations by Lambert-Beer's law and the incorporation of the gain coefficient into the concept of complex refractive indices. Furthermore it was shown how the gain and pump absorption coefficients for the stationary solution of a system of rate equations which describes a 4-level energy diagram can be obtained. In this appendix the resulting gain and pump absorption coefficients for other important laser energy systems are given. Independently of the complexity of the modeled energy system in principle the following steps have to be done:

1. Formulation of the corresponding set of rate equations including all relevant energy transitions.
2. Application of steady-state conditions of rate equations ($\mathrm{d}N_j/\mathrm{d}t = 0 \;\; \forall j$).
3. Solution of rate equations system in steady-state leads to the population densities N_j of the energy levels $\mathscr{E}_j$.
4. Calculation of gain and pump absorption coefficients according to Eqs. (2.71) and (2.73).

In the following analytical solutions for the 3-level laser system, the direct-pumped 3-level laser, and the quasi 4-level laser system between two manifolds are given.

B.1 3-level laser system

For the 3-level energy diagram given in Fig. B.1 the steady-state population densities are given by [108]

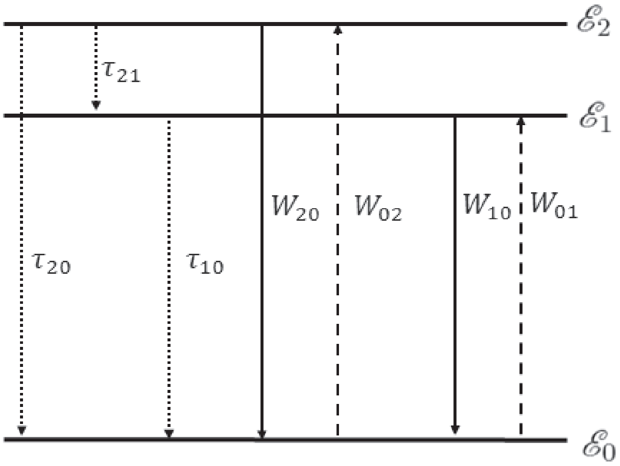

Figure B.1 – Relevant transitions of 3-level laser system: solid lines show energy transition due to stimulated emission, the dashed lines show photon absorption or non-optical pumping, and the dotted lines show non-radiative relaxation processes [108].

$$N_2 \approx 0 \ , \tag{B.1}$$

$$N_1 \approx \frac{\eta_\mathrm{p}\frac{I_\mathrm{p}}{I_\mathrm{s}^\mathrm{P}} + \frac{I_\mathrm{L}}{I_\mathrm{s}^\mathrm{L}}}{1 + 2\frac{I_\mathrm{L}}{I_\mathrm{s}^\mathrm{L}} + \eta_\mathrm{p}\frac{I_\mathrm{p}}{I_\mathrm{s}^\mathrm{P}}} N \ , \tag{B.2}$$

$$N_0 \approx \frac{1 + \frac{I_\mathrm{L}}{I_\mathrm{s}^\mathrm{L}}}{1 + 2\frac{I_\mathrm{L}}{I_\mathrm{s}^\mathrm{L}} + \eta_\mathrm{p}\frac{I_\mathrm{p}}{I_\mathrm{s}^\mathrm{P}}} N \ . \tag{B.3}$$

with different definitions of [108]

$$\frac{1}{\eta_\mathrm{p}} = 1 + \frac{\tau_{21}}{\tau'_{20}} \ , \tag{B.4}$$

$$N = N_2 + N_1 + N_0 \ , \tag{B.5}$$

$$I_\mathrm{s}^\mathrm{P} = \frac{h\nu_p}{\sigma_{02}\tau_\mathrm{em}} \ , \tag{B.6}$$

$$I_\mathrm{s}^\mathrm{L} = \frac{h\nu_L}{\sigma_{01}\tau_\mathrm{em}} \ . \tag{B.7}$$

and

$$\tau_\mathrm{em} = \tau'_{10} \ , \tag{B.8}$$

and where the approximations given by Eq. (2.66) and

$$\frac{\tau_{2i}}{\tau'_{10}} \approx 0 \ , \tag{B.9}$$

were used. Furthermore there is

$$f_0 = f_1 = f_2 = 1. \tag{B.10}$$

Plugging Eqs. (B.1) – (B.3) into Eqs. (2.71) and (2.73) lead to

$$g \approx \frac{\eta_{\mathrm{P}} \frac{I_{\mathrm{P}}}{I_{\mathrm{s}}^{\mathrm{P}}} - 1}{1 + 2\frac{I_{\mathrm{L}}}{I_{\mathrm{s}}^{\mathrm{L}}} + \eta_{\mathrm{P}} \frac{I_{\mathrm{P}}}{I_{\mathrm{s}}^{\mathrm{P}}}} \sigma_{01} N \ , \tag{B.11}$$

and

$$\alpha \approx \frac{1 + \frac{I_{\mathrm{L}}}{I_{\mathrm{s}}^{\mathrm{L}}}}{1 + 2\frac{I_{\mathrm{L}}}{I_{\mathrm{s}}^{\mathrm{L}}} + \eta_{\mathrm{P}} \frac{I_{\mathrm{P}}}{I_{\mathrm{s}}^{\mathrm{P}}}} \sigma_{02} N \ . \tag{B.12}$$

B.2 Direct-pumped 3-level laser system

For the direct-pumped 3-level energy diagram given in Fig. B.2 the steady-state population densities are given by [108]

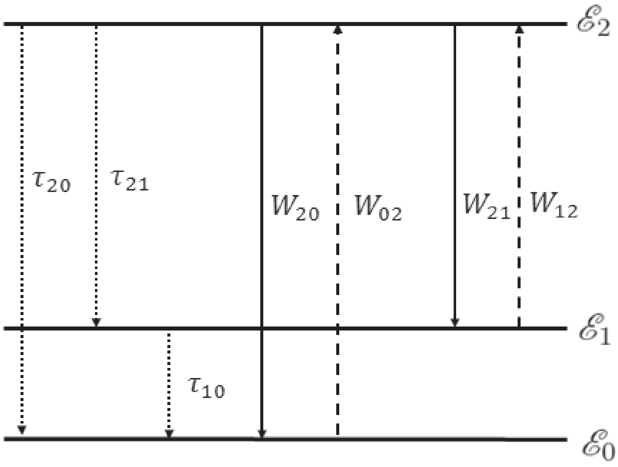

Figure B.2 – Relevant transitions of direct-pumped 3-level laser system: solid lines show energy transition due to stimulated emission, the dashed lines show photon absorption or non-optical pumping, and the dotted lines show non-radiative relaxation processes [108].

$$N_2 \approx \frac{\frac{I_{\mathrm{P}}}{I_{\mathrm{s}}^{\mathrm{P}}}}{1 + \frac{I_{\mathrm{L}}}{I_{\mathrm{s}}^{\mathrm{L}}} + 2\frac{I_{\mathrm{P}}}{I_{\mathrm{s}}^{\mathrm{P}}}} N \ , \tag{B.13}$$

$$N_1 \approx 0 \ , \tag{B.14}$$

$$N_0 \approx \frac{1 + \frac{I_{\mathrm{L}}}{I_{\mathrm{s}}^{\mathrm{L}}} + \frac{I_{\mathrm{p}}}{I_{\mathrm{s}}^{\mathrm{p}}}}{1 + \frac{I_{\mathrm{L}}}{I_{\mathrm{s}}^{\mathrm{L}}} + 2\frac{I_{\mathrm{p}}}{I_{\mathrm{s}}^{\mathrm{p}}}} N \ , \tag{B.15}$$

with the definitions of [108]

$$\frac{1}{\tau_{\mathrm{em}}} = \frac{1}{\tau_{21}} + \frac{1}{\tau_{20}'} \ , \tag{B.16}$$

$$I_{\mathrm{s}}^{\mathrm{p}} = \frac{h\nu_p}{\sigma_{02}\tau_{\mathrm{em}}} \ , \tag{B.17}$$

$$I_{\mathrm{s}}^{\mathrm{L}} = \frac{h\nu_L}{\sigma_{12}\tau_{\mathrm{em}}} \ . \tag{B.18}$$

and where the approximation given by Eq. (2.64) was used. Finally the gain coefficient is given by:

$$g \approx \frac{\frac{I_{\mathrm{p}}}{I_{\mathrm{s}}^{\mathrm{p}}}}{1 + \frac{I_{\mathrm{L}}}{I_{\mathrm{s}}^{\mathrm{L}}} + 2\frac{I_{\mathrm{p}}}{I_{\mathrm{s}}^{\mathrm{p}}}} \sigma_{12} N \ , \tag{B.19}$$

and the absorption coefficient for the pump beam by:

$$\alpha \approx \frac{1 + \frac{I_{\mathrm{L}}}{I_{\mathrm{s}}^{\mathrm{L}}}}{1 + \frac{I_{\mathrm{L}}}{I_{\mathrm{s}}^{\mathrm{L}}} + 2\frac{I_{\mathrm{p}}}{I_{\mathrm{s}}^{\mathrm{p}}}} \sigma_{03} N \ . \tag{B.20}$$

B.3 Quasi 4-level laser system between two manifolds

For the quasi 4-level energy diagram between two manifolds given in Fig. B.3 the steady-state population densities are given without any approximation by [108]

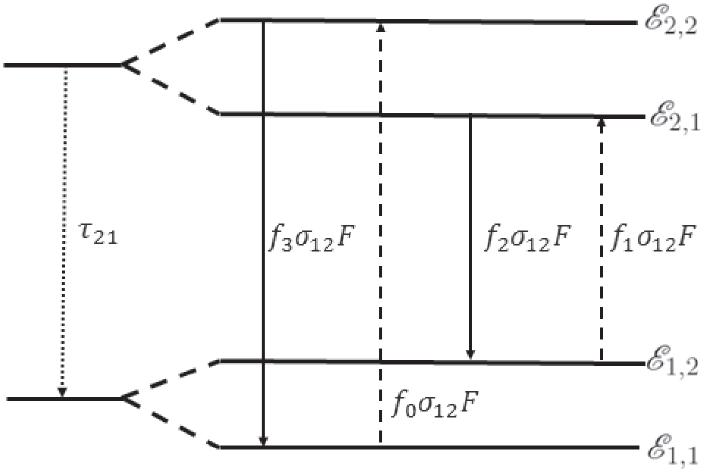

Figure B.3 – Relevant transitions of quasi 4-level laser system between two manifolds: solid lines show energy transition due to stimulated emission, the dashed lines show photon absorption or non-optical pumping, and the dotted lines show non-radiative relaxation processes [108].

$$N_2 = \frac{\frac{f_1}{f_2}\frac{I_\mathrm{L}}{I_\mathrm{s}^\mathrm{L}} + \frac{I_\mathrm{p}}{I_\mathrm{s}^\mathrm{p}}}{1 + \left(1 + \frac{f_1}{f_2}\right)\frac{I_\mathrm{L}}{I_\mathrm{s}^\mathrm{L}} + \left(1 + \frac{f_3}{f_0}\right)\frac{I_\mathrm{p}}{I_\mathrm{s}^\mathrm{p}}} N \ . \tag{B.21}$$

$$N_1 = \frac{1 + \frac{I_\mathrm{L}}{I_\mathrm{s}^\mathrm{L}} + \frac{f_3}{f_0}\frac{I_\mathrm{p}}{I_\mathrm{s}^\mathrm{p}}}{1 + \left(1 + \frac{f_1}{f_2}\right)\frac{I_\mathrm{L}}{I_\mathrm{s}^\mathrm{L}} + \left(1 + \frac{f_3}{f_0}\right)\frac{I_\mathrm{p}}{I_\mathrm{s}^\mathrm{p}}} N \ . \tag{B.22}$$

with the different definitions

$$\tau_\mathrm{em} = \tau_{21} \ , \tag{B.23}$$

$$N = N_1 + N_2 \ , \tag{B.24}$$

$$I_\mathrm{s}^\mathrm{p} = \frac{h\nu_p}{f_0 \sigma_{12} \tau_\mathrm{em}} \ , \tag{B.25}$$

and

$$I_\mathrm{s}^\mathrm{L} = \frac{h\nu_L}{f_1 \sigma_{12} \tau_\mathrm{em}} \ . \tag{B.26}$$

Please note that in contrast to the previous energy level diagrams, the degeneration and strong coupling of the $\mathscr{E}_{1,1}$ and $\mathscr{E}_{1,2}$ as well as of the $\mathscr{E}_{2,1}$ and $\mathscr{E}_{2,2}$ energy states in this quasi 4-level energy diagram result in different fractional populations f_j, which are typically calculated by Boltzmann's statistics [4]. Finally the gain coefficient is given by:

$$g = f_2\sigma_{12}N_2 - f_1\sigma_{12}N_1 = \frac{\left(\frac{f_2}{f_1} - \frac{f_3}{f_0}\right)\frac{I_\mathrm{p}}{I_\mathrm{s}^\mathrm{p}} - 1}{1 + \left(1 + \frac{f_1}{f_2}\right)\frac{I_\mathrm{L}}{I_\mathrm{s}^\mathrm{L}} + \left(1 + \frac{f_3}{f_0}\right)\frac{I_\mathrm{p}}{I_\mathrm{s}^\mathrm{p}}} f_1\sigma_{12}N \ . \tag{B.27}$$

and the absorption coefficient for the pump beam by:

$$\alpha = f_0\sigma_{12}N_1 - f_3\sigma_{12}N_2 = \frac{1 + \left(1 - \frac{f_1 f_3}{f_2 f_0}\right)\frac{I_\mathrm{L}}{I_\mathrm{s}^\mathrm{L}}}{1 + \left(1 + \frac{f_1}{f_2}\right)\frac{I_\mathrm{L}}{I_\mathrm{s}^\mathrm{L}} + \left(1 + \frac{f_3}{f_0}\right)\frac{I_\mathrm{p}}{I_\mathrm{s}^\mathrm{p}}} f_0\sigma_{12}N \ . \tag{B.28}$$

Appendix C

Derivation of Semi-Analytical Inclusion of Nonlinear Gain in vBPM

In the following Eq. (4.48) will be derived. Starting from the two coupled differential equations given in Eq. (4.46), there is:

$$\frac{\mathrm{d}|V_\ell|^2}{\mathrm{d}z} = \frac{g_0}{1 + \left(|V_1|^2 + |V_2|^2\right)/V_{\mathrm{sat}}^2}|V_\ell|^2 \quad , \quad \ell = 1, 2. \tag{C.1}$$

Adding of both equations leads to

$$\frac{\mathrm{d}\left(|V_1|^2 + |V_2|^2\right)}{\mathrm{d}z} = \frac{g_0\left(|V_1|^2 + |V_2|^2\right)}{1 + \left(|V_1|^2 + |V_2|^2\right)/V_{\mathrm{sat}}^2} \tag{C.2}$$

which has the exact solution

$$|V_1(z_0 + \Delta z)|^2 + |V_2(z_0 + \Delta z)|^2 = V_{\mathrm{sat}}^2 W\left(\frac{\exp(g_0\Delta z + c_1)}{V_{\mathrm{sat}}^2}\right). \tag{C.3}$$

for g_0 being Δz invariant. Here $W(a)$ is the LambertW function (also called product logarithm) which can be defined by $a = W(a)\exp\left[W(a)\right]$ [167]. c_1 is a constant, depending on the initial value of the differential equation at $\Delta z = 0$. It can be written as:

$$c_1 = \ln\left(|V_1(z_0)|^2 + |V_2(z_0)|^2\right) + \left(\frac{|V_1(z_0)|^2 + |V_2(z_0)|^2}{V_{\mathrm{sat}}^2}\right) \tag{C.4}$$

with ln being the natural logarithm in the base e. In the next step the two terms on the left hand side of Eq. (C.3) are separated. Please note that the polarization of the electric field is maintained within the operator given by Eq. (4.39). Consequently there is:

$$|V_\ell(z_0 + \Delta z))|^2 = \frac{|V_\ell(z_0)|^2}{|V_1(z_0)|^2 + |V_2(z_0)|^2}V_{\mathrm{sat}}^2 W\left(\frac{\exp(g_0\Delta z + c_1)}{V_{\mathrm{sat}}^2}\right) \quad , \quad \ell = 1, 2. \tag{C.5}$$

In addition to the real-valued gain g, an additional phase shift $\mathrm{i}g'$ is introduced in reality by the active medium. Typically this additional phase shift only depends on the angular frequency ω_0 of the field oscillating in the resonator cavity. In a first approximation there is no dependence on the position, ending up with a constant phase shift for each wavelength [71]. Consequently in a single nonlinear $\mathcal{C}^{\mathrm{gain}}_{\alpha\beta,s}$ step the wavefront of the field does not change it's shape. In this case Eq. (C.5) can be rewritten to

$$V_\ell(z_0+\Delta z) = \frac{V_\ell(z_0)}{\left(|V_1(z_0)|^2+|V_2(z_0)|^2\right)^{1/2}} \left[V_{\mathrm{sat}}^2 W\left(\frac{\exp(g_0\Delta z + c_1)}{V_{\mathrm{sat}}^2}\right)\right]^{(1/2)} \quad , \quad \ell = 1,2. \tag{C.6}$$

In this work the constant phase shift is neglected, meaning that $\mathrm{i}g' = 0$, because just the calculation of the transversal mode profile of the laser is of interest. In this case Eq. (4.48) is valid. As discussed in chapter 3.1, in principle it is also possible to analyze the axial modes of the laser resonator by the calculation of the eigenvalue's phase term ϕ_ℓ. Then the inclusion of the phase shift would be important for all wavelengths except for the center wavelength of the spectral gain profile, where the phase shift is zero anyway [71].

Bibliography

[1] R. Poprawe, *Taylored Light 2: Laser Application Technology (RWTH Edition)* (Springer, 2011).

[2] C. E. Webb and J. D. C. Jones, *Handbook of Laser Technology and Applications - Volume 3: Applications* (Inst. of Physics Pub., 2004).

[3] P. C. Mehta and V. V. Rampal, *Lasers and Holography* (World Scientific, 1993).

[4] O. Svelto, *Principles of Lasers* (Springer, 2010).

[5] W. Koechner, *Solid-State Laser Engineering* (Springer, 2006).

[6] R. Iffländer, *Solid-State Lasers for Materials Processing: Fundamental Relations and Technical Realizations* (Springer, 2012).

[7] A. G. Fox and T. Li, "Resonant modes in a maser interferometer," Bell Syst. Tech. J. **40**(2), 453–488 (1961).

[8] A. G. Fox and T. Li, "Modes in a maser interferometer with curved and tilted mirrors," Proc. IEEE **51**(1), 80–89 (1964).

[9] A. E. Siegman and E. A. Sziklas, "Mode calculations in unstable resonators with flowing saturable gain. 1: Hermite-Gaussian expansion," Appl. Opt. **13**(12), 2775–2792 (1974).

[10] E. A. Sziklas and A. E. Siegman, "Mode calculations in unstable resonators with flowing saturable gain. 2: fast Fourier transform method," Appl. Opt. **14**(8), 1874–1889 (1975).

[11] P. A. M. Dirac, "The quantum theory of the emission and absorption of radiation," Proc. R. Soc. Lond. A **114**(767), 243–265 (1927).

[12] W. Heitler, *The Quantum Theory of Radiation* (Oxford University Press, 1953).

[13] H. Haken, *Laser Theory* (Springer, 2012).

[14] K. Altmann, "Contradiction within wave optics and its solution within a particle picture," Opt. Exp. **23**(3), 3731–3750 (2015).

[15] W. Koechner, "Thermal lensing in a Nd:YAG laser rod," Appl. Opt. **9**(11), 2548–2553 (1970).

[16] W. Koechner and D. K. Rice, "Effect of birefringence on the performance of linearly polarized YAG:Nd lasers," IEEE J. Quantum Electron. **6**(9), 557–566 (1970).

[17] J. D. Foster and L. M. Osterink, "Thermal effects in a Nd: YAG laser," Appl. Opt. **41**(9), 3656–3663 (1970).

[18] M. Schmid, R. Weber, T. Graf, M. Roos, and H. P. Weber, "Numerical simulation and analytical description of thermally induced birefringence in laser rods," IEEE J. Quantum Electron. **36**(5), 620–626 (2000).

[19] W. C. Scott and M. de Wit, "Birefringence compensation and TEM_{00} mode enhancement in a Nd:YAG laser," Appl. Phys. Lett. **18**(1), 3–4 (1971).

[20] Q. Lü, N. Kugler, H. Weber, S. Dong, N. Müller, and U. Wittrock, "A novel approach for compensation of birefringence in cylindrical Nd:YAG rods," Opt. Quant. Electron. **28**(1), 57–69 (1996).

[21] J. R. Leger, D. Chen, and Z. Wang, "Diffractive optical element for mode shaping of a Nd:YAG laser," Opt. Lett. **19**(2), 108–110 (1994).

[22] J. Sherman, "Thermal compensation of a cw-pumped Nd:YAG laser," Appl. Opt. **37**(33), 7789–7796 (1998).

[23] M. Born and E. Wolf, *Principles of Optics: Electromagnetic Theory of Propagation, Interference and Diffraction of Light* (Cambridge University, 1999).

[24] J. M. Eggleston, T. J. Kane, K. Kuhn, J. Unternahrer, and R. L. Byer, "The slab geometry laser - part I: theory," IEEE J. Quantum Electron. **20**(3), 289–301 (1984).

[25] R. J. Gelinas, S. K. Doss, and R. G. Nelson, "3-D TECATE/BREW: Thermal, stress, and birefringent ray-tracing codes for solid-state laser design," Lawrence Livermore National Lab, technical report UCRL-ID-115123 (1994).

[26] M. Rehak and J. M. Di Nicola, "COMBINE: An integrated opto-mechanical tool for laser performance modeling," Proc. SPIE **9345**, 93450K (2015).

[27] A. Sharma, D. V. Kumar, and A. K. Ghatak, "Tracing rays through graded-index media: a new method," Appl. Opt. **21**(6), 984–987 (1982).

[28] V. Magni, G. Valentini, and S. De Silvestri, “Recent developments in laser resonator design,” Opt. Quant. Electron. **23**(9), 1105–1134 (1991).

[29] S. De Silvestri, P. Laporta, and V. Magni, “Rod thermal lensing effects in solid-state laser ring resonators,” Opt. Commun. **65**(5), 373–376 (1988).

[30] B. E. A. Saleh and M. C. Teich *Fundamentals of Photonics* (Wiley, 2007).

[31] P. Torres and A. M. Guzman, “Complex finite-element method applied to the analysis of optical waveguide amplifiers,” J. Lightw. Technol. **15**(3), 546–550 (1997).

[32] A. Bossavit, “A rationale for edge-elements in 3D fields computations,” IEEE T. Magn. **24**(1), 74–79 (1988).

[33] X. Wei, H. P. Urbach, and A. J. H. Wachters, “Finite element model for three-dimensional optical scattering problems,“ J. Opt. Soc. Am. A **24**(3), 866–881 (2007).

[34] M. Okoniewski, M. Mrozowski, and M. A. Stuchly, “Simple treatment of multiterm dispersion in FDTD,” IEEE Microwave Guid. Wave Lett. **7**(5), 121–123 (1997).

[35] A. S. Nagra and R. A. York, “FDTD analysis of wave propagation in nonlinear absorbing and gain media,” IEEE Trans. Antennas Propag. **46**(3), 334–340 (1998).

[36] K. S. Yee, “Numerical solution of initial boundary value problems involving Maxwell’s equations in isotropic media,” IEEE T. Antenn. Propag. **14**(3), 302–307 (1966).

[37] J. P. Bérenger, “A perfectly matched layer for the absorption of electromagnetic waves”, J. Comput. Phys. **114**(2), 185–200 (1994).

[38] A. Taflove and S. Hagness, *Computational Electrodynamics: The Finite-Difference Time-Domain Method* (Artech House, 2000).

[39] M. G. Moharam, E. B. Grann, D. A. Pommet, and T. K. Gaylord, “Formulation for stable and efficient implementation of the rigorous coupled-wave analysis of binary gratings,” J. Opt. Soc. Am. A **12**(5), 1068–1076 (1995).

[40] P. Lalanne and E. Silberstein, “Fourier-modal methods applied to waveguide computational problems,” Opt. Lett. **25**(15), 1092–1094 (2000).

[41] E. Silberstein, P. Lalanne, J. P. Hugonin, and Q. Cao, “On the use of grating theory in integrated optics,” J. Opt. Soc. Am. A **18**(11), 2865–2875 (2001).

[42] J. P. Hugonin and P. Lalanne, “Perfectly matched layers as nonlinear coordinate transforms: a generalized formalization,” J. Opt. Soc. Am. A **22**(9), 1844–1849 (2005).

[43] M. D. Feit and J. A. Fleck, “Light propagation in graded-index optical fibers,” Appl. Opt. **17**(24), 3990–3998 (1978).

[44] L. Thylen and D. Yevick, “Beam propagation method in anisotropic media,” Appl. Opt. **21**(15), 2751–2754 (1982).

[45] J. A. Fleck and M. D. Feit, “Beam propagation in uniaxial anisotropic media,” J. Opt. Soc. Am. **73**(7), 920–926 (1983).

[46] H. Shu and M. Bass, “Three-dimensional computer model for simulating realistic solid-state lasers,” Appl. Opt. **46**(23), 5687–5697 (2007).

[47] H. Shu, Y. Chen, M. Bass, J. F. Monjardin, and J. Deile, “Numerical modeling of alkali vapor lasers,” Opt. Exp. **19**(21), 19875–19885 (2011).

[48] S. A. Collins, JR., “Lens-system diffraction integral written in terms of matrix optics,” J. Opt. Soc. Am. **60**(9), 1168–1177 (1970).

[49] J. P. Taché, “Derivation of ABCD law for Laguerre-Gaussian beams,” Appl. Opt. **26**(14), 2698–2700 (1987).

[50] A. Belafhal and L. Dalil-Essakali, “Collins formula and propagation of Bessel-modulated Gaussian light beams through an ABCD optical system,” Opt. Commun. **177**(1), 181–188 (2000).

[51] F. Wyrowski and M. Kuhn, “Introduction to field tracing,” J. Mod. Opt. **58**(5-6), 449–466 (2011).

[52] M. Kuhn, F. Wyrowski, and C. Hellmann, “Non-sequential optical field tracing,” in *Advanced Finite Element Methods and Applications - Lecture Notes in Applied and Computational Mechanics*, T. Apel and O. Steinbach, eds. (Springer, 2013).

[53] A. E. Siegman, “How to (maybe) measure laser beam quality,” in *Diode Pumped Solid State Lasers: Applications and Issues*, OSA Trends in Optics and Photonics (Optical Society of America 1998), paper MQ1.

[54] K. D. Kirkham and C. B. Roundy, “Current technology of beam profile measurement,” in *Laser Beam Shaping - Theory and Techniques*, F. M. Dickey, ed. (Taylor & Francis Inc, 2014).

[55] Y.-Z. Huang, W.-H. Guo, and Q.-M. Wang, “Analysis and numerical simulation of eigenmode characteristics for semiconductor lasers with an equilateral triangle microresonator,” IEEE J. Quantum Electron. **37**(1), 100–107 (2001).

[56] P. Nyakas, “Full-vectorial three-dimensional finite element optical simulation of vertical-cavity surface-emitting lasers,” J. Lightw. Technol. **25**(9), 2427–2434 (2007).

[57] A. Christ, N. Kuster, M. Streiff, A. Witzig, and W. Fichtner, “Correction of the numerical reflection coefficient of the finite-difference time-domain method for efficient simulation of vertical-cavity surface-emitting lasers,” J. Opt. Soc. Am. B **20**(7), 1401–1408 (2003).

[58] M. Streiff, A. Witzig, M. Pfeiffer, P. Royo, and W. Fichtner, “A comprehensive VCSEL device simulator,” IEEE J. Sel. Topics Quantum Electron. **9**(3), 879–891 (2003).

[59] J. Pomplun, S. Burger, F. Schmidt, A. Schliwa, D. Bimberg, A. Pietrzak, H. Wenzel, and G. Erbert, “Finite element simulation of the optical modes of semiconductor lasers,” Phys. Status Solidi B **247**(4), 846–853 (2010).

[60] K. Altmann, C. Pflaum, and D. Seider, “Three-dimensional finite element computation of laser cavity eigenmodes,” Appl. Opt. **43**(9), 1892–1901 (2004).

[61] L. Bergstein and H. Schachter, “Resonant modes of optic interferometer cavities. I. Plane-parallel end reflectors,” J. Opt. Soc. Am. **54**(7), 887–903 (1964).

[62] L. Bergstein and H. Schachter, “Resonant modes of optic cavities of small Fresnel numbers,” J. Opt. Soc. Am. **55**(10), 1226–1231 (1965).

[63] D. Burak and R. Binder, “Cold-cavity vectorial eigenmodes of VCSEL’s,” IEEE J. Quantum Electron. **33**(7), 1205–1215 (1997).

[64] Q. Deng and D. G. Deppe, “Self-consistent calculation of the lasing eigenmode of the dielectrically apertured Fabry-Perot microcavity with idealized or distributed Bragg reflectors,” IEEE J. Quantum Electron. **33**(12), 2319–2326 (1997).

[65] B. Demeulenaere, P. Bienstman, B. Dhoedt, and R. G. Baets, “Detailed study of AlAs-oxidized apertures in VCSEL cavities for optimized modal performance,” IEEE J. Quantum Electron. **35**(3), 358–367 (1999).

[66] P. Bienstman, B. Demeulenaere, B. Dhoedt, and R. Baets, “Simulation results of transverse-optical confinement in airpost, regrown, and oxidized vertical-cavity surface-emitting laser structures,” J. Opt. Soc. Am. B **16**(11), 2055–2059 (1999).

[67] G. P. Bava, P. Debernardi, and L. Fratta, “Three-dimensional model for vectorial fields in vertical-cavity surface-emitting lasers,” Phys. Rev. A **63**(2), 023816 (2001).

[68] H. Kogelnik, “Imaging of optical modesResonators with internal lenses,” Bell Syst. Tech. J. **44**(3), 455–494 (1965).

[69] H. Kogelnik and T. Li, “Laser beams and resonators,” Appl. Opt. **5**(10), 1550–1567 (1966).

[70] P. Baues, “The connection of geometrical optics with the propagation of Gaussian beams and the theory of optical resonators,” Opto-electronics **1**(2), 103–118 (1969).

[71] A. E. Siegman, *Lasers* (University Science Books, 1986).

[72] C. N. Kurtz and W. Streifer, “Guided waves in inhomogeneous focusing media, part I: formulation, solution for quadratic inhomogeneity,” IEEE Trans. Microw. Theory Techn. **17**(1), 11–15 (1969).

[73] W. J. Firth, “Propagation of laser beams through inhomogeneous media,” Opt. Commun. **22**(2), 226–230 (1977).

[74] H. Kogelnik, “On the propagation of Gaussian beams of light through lenslike media including those with a loss or gain,” Appl. Opt. **4**(12), 1562–1569 (1965).

[75] A. E. Siegman, “Nonorthogonal optical modes and resonators,” in *Optical Resonators - Science and Engineering*, R. Kossowski, M. Jelinek, and J. Novak, eds. (Kluwer Academic Publishers, 1998).

[76] A. E. Siegman, “Laser beams and resonators: The 1960s,” IEEE J. Quantum Electron. **6**(6), 1380–1388 (2000).

[77] T. Y. Fan and R. L. Byer, “Diode laser-pumped solid-state lasers,” IEEE J. Quantum Electron. **24**(6), 895–912 (1988).

[78] D. G. Hall, R. J. Smith., and R. R. Rice. “Pump-size effects in Nd:YAG lasers,” Appl. Opt. **19**(18), 3041–3043 (1980).

[79] L. W. Casperson, “Laser power calculations: sources of error,” Appl. Opt. **19**(3), 422–431 (1980).

[80] P. F. Moulton, “An investigation of the Co:MgF2 laser system,” IEEE J. Quantum Electron. **21**(10), 1582–1588 (1985).

[81] M. Wohlmuth, C. Pflaum, K. Altmann, M. Paster, and C. Hahn, “Dynamic multimode analysis of Q-switched solid state laser cavities,” Opt. Exp. **17**(20), 17303–17316 (2009).

[82] J. Junghans, M. Keller, and H. Weber, “Laser resonators with polarizing elements - eigenstates and eigenvalues of polarization,” Appl. Opt. **13**(12), 2793–2798 (1974).

[83] N. Hodgson and H. Weber, *Optical Resonators: Fundamentals, Advanced Concepts, Applications* (Springer Science, 2005).

[84] W. M. Doyle and M. B. White, “Properties of an anisotropic Fabry-Perot resonator,” J. Opt. Soc. Am. **55**(10), 1221–1225 (1965).

[85] R. C. Jones, “A new calculus for the treatment of optical systems. IV.,” J. Opt. Soc. Am. **32**(8), 486–493 (1942).

[86] T. Graupeter, R. Hartmann, and C. Pflaum, “Calculations of eigenpolarization in Nd:YAG laser rods due to thermally induced birefringence,” IEEE J. Quantum Electron. **50**(12), 1035–1043 (2014).

[87] P. Vahimaa and J. Turunen, “Finite-elementary-source model for partially coherent radiation,” Opt. Exp. **14**(4), 1376-1381 (2006).

[88] J. Tervo, J. Turunen, P. Vahimaa, and F. Wyrowski, “Shifted-elementary-mode representation for partially coherent vectorial fields,” J. Opt. Soc. Am. A **27**(9), 2004–2014 (2010).

[89] H. Schimmel and F. Wyrowski, “Using diffuser technology for illumination systems,” Proc. SPIE **5962**, 59621C (2005).

[90] D. Asoubar, C. Hellmann, H. Schweitzer, M. Kuhn, and F. Wyrowski, “Customized homogenization and shaping of LED light by micro cells arrays,” Proc. SPIE **9383**, 93831B (2015).

[91] F. Wyrowski, C. Hellmann, R. Krieg, and H. Schweitzer, “Modeling the propagation of ultrashort pulses through optical systems, Proc. SPIE **7589**, 75890O (2010).

[92] S. Veetil, H. Schimmel, and F. Wyrowski, “Simulation of multibeam imaging in three-dimensional space and time with a diffractive optical element illuminated with a femtosecond pulse, J. Opt. Soc. Am. B **24**(10), 2580–2583 (2007).

[93] S. Veetil, H. Schimmel, F. Wyrowski, and C. Vijayan, “Wave optical modelling of focusing of an ultra short pulse,” J. Mod. Opt. **53**(15), 2187–2194 (2006).

[94] S. Veetil, C. Vijayan, D. Sharma, H. Schimmel, and F. Wyrowski, “Diffraction induced space-time splitting effects in ultra-short pulse propagation,” J. Mod. Opt. **53**(13), 1819–1828 (2006).

[95] S. Veetil, K. Viswanathan, C. Vijayan, and F. Wyrowski, “Spectral and temporal evolutions of ultrashort pulses diffracted through a slit near phase singularities, Appl. Phys. Lett. **89**(4), 041119 (2006).

[96] S. Zhang, D. Asoubar, R. Kammel, S. Nolte, and F. Wyrowski, “Analysis of pulse front tilt in simultaneous spatial and temporal focusing,” J. Opt. Soc. Am. A **31**(11), 2437–2446 (2014).

[97] L. G. Gouy, “Sur une propriete nouvelle des ondes lumineuses,” Compt. Rendue Acad. Sci. Paris **110**, 1251–1253 (1890).

[98] A. Rubinowicz, “On the anomalous propagation of phase in the focus,” Phys. Rev. **54**(11), 931–936 (1938).

[99] R. W. Boyd, “Intuitive explanation of the phase anomaly of focused light beams,” J. Opt. Soc. Am. **70**(7), 877–880 (1980).

[100] F. Wyrowski and C. Hellmann, “Geometrical optics reloaded,” Proc. DGAO, (2015).

[101] H. S. Green and E. Wolf, “A scalar representation of electromagnetic fields,” Proc. Phys. Soc. A **66**(12), 1129–1137 (1953).

[102] C. D. Meyer, *Matrix Analysis and Applied Linear Algebra* (Society for Industrial and Applied Mathematics, 2001).

[103] L. Mandel and E. Wolf, *Optical Coherence and Quantum Optics* (Cambridge University Press, 1995).

[104] U. D. Zeitner and F. Wyrowski, “Design of unstable laser resonators with user-defined mode shape,” IEEE J. Quantum Electron. **37**(12), 1594–1599 (2001).

[105] N. N. Elkin and A. P. Napartovich, “Numerical study of the stability of single-mode lasing in a Fabry-Perot resonator with an active medium,” Appl. Math. Model. **18**(9), 513–521 (1994).

[106] T. F. Johnston, M. W. Sasnett, J. Doumont, and A. E. Siegman, “Laser beam quality versus aperture size in a cw argon-ion laser,” Opt. Lett. **17**(3), 198–200 (1992).

[107] H.-C. Eckstein and U. D. Zeitner, “Modeling electro-optical characteristics of broad area semiconductor lasers based on a quasi-stationary multimode analysis,” Opt. Express **21**(20), 23231–23240 (2013).

[108] Y. Sato and T. Taira, “Saturation factors of pump absorption in solid-state lasers,” IEEE J. Quantum Electron. **40**(3), 270–280 (2004).

[109] S. S. Brody, “Instrument to measure fluorescence lifetimes in the millimicrosecond region,” Rev. Sci. Instrum. **28**(12), 1021–1026 (1957).

[110] J. R. Lakowicz, *Principles of Fluorescence Spectroscopy* (Springer, 2007).

[111] R. W. Boyd, *Nonlinear Optics* (Academic Press, 2008).

[112] D. Asoubar, S. Zhang, F. Wyrowski, and M. Kuhn, “Parabasal field decomposition and its applications to non-paraxial propagation,” Opt. Exp. **20**(21), 23502–23517 (2012).

[113] D. Asoubar, S. Zhang, F. Wyrowski, and M. Kuhn, “Efficient semi-analytical propagation techniques for electromagnetic fields,” J. Opt. Soc. Am. A **31**(3), 591–602 (2014).

[114] S. Zhang, D. Asoubar, C. Hellmann, and F. Wyrowski, “Propagation of electromagnetic fields between non-parallel planes: a fully vectorial formulation and an efficient implementation,” Appl. Opt. (submitted for publication) (2015).

[115] W. Goodman, *Introduction to Fourier optics* (McGraw-Hill, 1968).

[116] H. Zhong, S. Zhang, and F. Wyrowski, “Parabasal thin-element approximation approach for the analysis of microstructured interfaces and freeform surfaces,” J. Opt. Soc. Am. A **32**(1), 124–129 (2015).

[117] J. W. Cooley and J. W. Tukey, “An algorithm for the machine calculation of complex Fourier series,” Math. Comput. **19**(90), 297–301 (1965).

[118] J. A. C. Veerman, J. J. Rusch, and H. P. Urbach, “Calculation of the Rayleigh-Sommerfeld diffraction integral by exact integration of the fast oscillating factor,” J. Opt. Soc. Am. A **22**(4), 636–646 (2005).

[119] S. Zhang, H. Zhong, D. Asoubar, F. Wyrowski, and M. Kuhn, “Tilt operator for electromagnetic fields and its application to propagation through plane interfaces,” Proc. SPIE **8550**, 85503I (2012).

[120] S. Zhang, D. Asoubar, F. Wyrowski, and M. Kuhn, “Efficient and rigorous propagation of harmonic fields through plane interfaces,” Proc. SPIE **8429**, 84290J (2012).

[121] J. H. Wilkinson, *The Algebraic Eigenvalue Problem* (Clarendon Press, 1988).

[122] W. Streifer, “Optical resonator modes-rectangular reflectors of spherical curvature,” J. Opt. Soc. Am. **55**(7), 868–877 (1965).

[123] W. Streifer, “On the integral equation for Fabry-Perot interferometer modes,” Phys. Lett. **18**(2), 118–119 (1965).

[124] A. E. Siegman and H. Y. Miller, “Unstable Optical Resonator Loss Calculations Using the Prony Method,” Appl. Opt. **9**(12), 2729–2736 (1970).

[125] W. D. Murphy and M. L. Bernabe, “Numerical procedures for solving nonsymmetric eigenvalue problems associated with optical resonators,” Appl. Opt. **20**(15), 2358–2365 (1978).

[126] M. Kuhn, F. Wyrowski, C. Hellmann, and T. Schöning, “Simulation, eigenmode analysis and tolerancing for stable laser resonators,” Proc. SPIE **7721**, 77210W (2010).

[127] H.-C. Eckstein, “Modenkontrolle in Halbleiterlasern durch monolithisch integrierte mikrooptische Elemente,” PHD Thesis, Friedrich-Schiller-University Jena (2014).

[128] M. D. Feit and J. A. Fleck, “Spectral approach to optical resonator theory,” Appl. Opt. **20**(16), 2843–2851 (1981).

[129] G. W. Stewart, “On the powers of a matrix with perturbations,” Numerische Mathematik **96**(2), 363–376 (2003).

[130] S. Eastman and D. Estep, “A power method for nonlinear operators,” Appl. Anal. **86**(10), 1303–1314 (2007).

[131] A. Sidi, “Vector extrapolation methods with applications to solution of large systems of equations and to PageRank computations,” Computers and Mathematics with Applications **56**(1), 1–24 (2008).

[132] A. Sidi, “Efficient implementation of minimal polynomial and reduced rank extrapolation methods,” J. Comput. Appl. Math. **36**(3), 305–337 (1991).

[133] S. Mondal, S. P. Singh, K. Hussain, A. Choubey, B. N. Upadhyay, and P. K. Datta , “Efficient depolarization-loss-compensation of solid state lasers using only a Glan-Taylor polarizer,” Opt. Laser Technol. **45**, 154–159 (2013).

[134] D. Asoubar, S. Zhang, and F. Wyrowski, “Simulation of birefringence effects on the dominant transversal laser resonator mode caused by anisotropic crystals,” Opt. Exp. **23**(11), 13848–13865 (2015).

[135] T. Taira, A. Mukai, Y. Nozawa, and T. Kobayashi, “Single-mode oscillation of laser-diode-pumped Nd:YVO$_4$ microchip lasers,” Opt. Lett. **16**(24), 1955–1957 (1991).

[136] D. S. Kliger and J. W. Lewis, *Polarized Light in Optics and Spectroscopy* (Elsevier, 1990).

[137] L. Yan and C. H. Lee, “Thermal effects in end-pumped Nd:phosphate glasses,” J. Appl. Phys. **75**(3), 1286–1292 (1994).

[138] T. Kimura and K. Otsuka, “Thermal effects of a continuously pumped Nd^{3+}:YAG laser,” IEEE J. Quantum Electron. **7**(8), 403–407 (1971).

[139] W. W. Rigrod, “Saturation effects in high gain lasers,” Appl. Phys. **36**(8), 2487–2490 (1965).

[140] A. G. Fox and T. Li, “Effects of gain saturation on the oscillating modes of optical masers,” IEEE J. Quantum Electron. **2**(12), 774–783 (1966).

[141] D. W. Berreman, “Optics in stratified and anisotropic media: 4 × 4-matrix formulation,” J. Opt. Soc. Am. **62**(4), 502–510 (1972).

[142] P. Yeh, “Electromagnetic propagation in birefringent layered media,” J. Opt. Soc. Am. **69**(5), 742–756 (1979).

[143] S. R. Seshadri, “Beam dynamics of two modes propagating along the optic axis in a uniaxial crystal,” J. Opt. Soc. Am. A **22**(2), 361–369 (2005).

[144] M. V. Berry, M. R. Jeffrey, and J. G. Lunney, “Conical diffraction: observations and theory,” Proc. R. Soc. Lond. A **462**(2070), 1629–1642 (2006).

[145] C. F. Phelan, D. P. O’Dwyer, Y. P. Rakovich, J. F. Donegan, and J. G. Lunney, “Conical diffraction and Bessel beam formation with a high optical quality biaxial crystal,” Opt. Exp. **17**(15), 12891–12899 (2009).

[146] J. J. Stamnes and V. Dhayalan, “Double refraction of a Gaussian beam into a uniaxial crystal,” J. Opt. Soc. Am. A **29**(4), 486–497 (2012).

[147] L. I. Perez, “Nonspecular transverse effects of polarized and unpolarized symmetric beams in isotropicuniaxial interfaces,” J. Opt. Soc. Am. A **20**(4), 741–752 (2003).

[148] A. Ciattoni, B. Crosignani, and P. Di Porto, “Vectorial theory of propagation in uniaxially anisotropic media,” J. Opt. Soc. Am. A **18**(7), 1656–1661 (2001).

[149] A. Ciattoni, G. Cincotti, and C. Palma, “Propagation of cylindrically symmetric fields in uniaxial crystals,” J. Opt. Soc. Am. A **19**(4), 792–796 (2002).

[150] A. Ciattoni, G. Cincotti, and C.Palma, “Nonparaxial description of reflection and transmission at the interface between an isotropic medium and a uniaxial crystal,” J. Opt. Soc. Am. A **19**(7), 1422–1431 (2002).

[151] A. Ciattoni and C. Palma, “Optical propagation in uniaxial crystals orthogonal to the optical axis: paraxial theory and beyond,” J. Opt. Soc. Am. A **20**(11), 2163–2171 (2003).

[152] É. Lalor “The angular spectrum representation of electromagnetic fields in crystals. I. Uniaxial crystals,” J. Math. Phys. **13**(4), 437–443 (1972).

[153] É. Lalor "The angular spectrum representation of electromagnetic fields in crystals. II. Biaxial crystals," J. Math. Phys. **13**(4), 443–449 (1972).

[154] G. D. Landry and T. A. Maldonado, "Complete method to determine transmission and reflection characteristics at a planar interface between arbitrarily oriented biaxial media," J. Opt. Soc. Am. A **12**(9), 2048–2063 (1995).

[155] P. Yeh, "Electromagnetic propagation in birefringent layered media," J. Opt. Soc. Am. **69**(5), 742–756 (1979).

[156] H. C. Chen, "A coordinate-free approach to wave propagation in anisotropic media," J. Appl. Phys. **53**(7), 4606–4609 (1982).

[157] NMath .NET Math Library, http://www.centerspace.net.

[158] S. C. McClain, L. W. Hillman, and R. A. Chipman, "Polarization ray tracing in anisotropic optically active media. II. Theory and physics," J. Opt. Soc. Am. A **10**(11), 2383–2393 (1993).

[159] G. M. Slavcheva, J. M. Arnold, and R. W. Ziolkowski, "FDTD simulation of the nonlinear gain dynamics in active optical waveguides and semiconductor microcavities," IEEE J. Sel. Topics Quantum Electron. **10**(5), 1052-1062 (2004).

[160] G. L. Tan, N. Bewtra, K. Lee, and J. M. Xu, "A two-dimensional nonisothermal finite element simulation of laser diodes," IEEE J. Quantum Electron. **29**(3), 822–835 (1993).

[161] L. W. Casperson and A. Yariv, "The gaussian mode in optical resonators with a radial gain profile," Appl. Phys. Lett. **12**(10), 355–357 (1968).

[162] P. Baues, "Huygens' principle in inhomogeneous, isotropic media and a general integral equation applicable to optical resonators," Opto-electronics **1**(1), 37–44 (1969).

[163] M. Nazarathy, A. Hardy, and J. Shamir, "Generalized mode propagation in first-order optical systems with loss or gain," J. Opt. Soc. Am. **72**(10), 1409–1420 (1982).

[164] D. B. Rensch, "Three-dimensional unstable resonator calculations with laser medium," Appl. Opt. **13**(11), 2546–2561 (1974).

[165] L. Xu, P. Huang, J. Chrostowski, and S. K. Chaudhuri, "Full-vectorial beam propagation method for anisotropic waveguides," J. Lightw. Technol. **12**(11), 1926–1931 (1994).

[166] J. Saijonmaa and D. Yevick, "Beam-propagation analysis of loss in bent optical waveguides and fibers," J. Opt. Soc. Am. **73**(12), 1785–1791 (1983).

[167] R. M. Corless, G. H. Gonnet, D. E. G. Hare, D. J. Jeffrey and D. E. Knuth, “On the LambertW function,” Adv. Comput. Math. **5**(1), 329–359 (1996).

[168] A. Hoorfar and M. Hassani, “Inequalities on the Lambert W function and hyperpower function,” J. Inequal. Pure and Appl. Math **9**(2), 5–9 (2008).

[169] C. Pfistner, R. Weber, H. P. Weber, S . Merazzi, and R. Gruber, “Thermal beam distortions in end-pumped Nd: YAG, Nd: GSGG, and Nd : YLF rods,” IEEE J. Quantum Electron. **30**(7), 1605–1615 (1994).

[170] U. O. Farrukh, A. M. Buoncristiani, and C. E. Byvik, “An analysis of the temperature distribution in finite solid-state laser rods,” IEEE J. Quantum Electron. **24**(11), 2253–2263 (1988).

[171] S. C. Tidwell, J. F. Seamans, M. S. Bowers, and A. K. Cousins, “Scaling cw diode-end-pumped Nd: YAG lasers to high average powers,” IEEE J. Quantum Electron. **28**(4), 997–1009 (1992).

[172] M. Schmid, T. Graf, and H. P. Weber, “Analytical model of the temperature distribution and the thermally induced birefringence in laser rods with cylindrically symmetric heating,” J. Opt. Soc. Am. B **17**(8), 1398–1404 (2000).

[173] S. Chenais, S. Forget, F. Druon, F. Balembois, and P. Georges, ”Direct and absolute temperature mapping and heat transfer measurements in diode-end-pumped Yb:YAG,” Appl. Phys. B **79**(2), 221–224 (2004).

[174] J. Didierjean, S. Forget, S. Chenais, F. Druon, F. Balembois, P. Georges, K. Altmann, and C. Pflaum, “High-resolution absolute temperature mapping of laser crystals in diode-end-pumped configuration,” Proc. SPIE **5707**, 370–379 (2005).

[175] J. D. Foster and L. M. Osterink, “Index of refraction and expansion thermal coefficients of Nd:YAG,” Appl. Opt. **7**(12), 2428–2429 (1968).

[176] J. L. Blows, J. M. Dawes, and T. Omatsu, “Thermal lensing measurements in line-focus end-pumped neodymium yttrium aluminium garnet using holographic lateral shearing interferometry,” Appl. Phys. **83**(6), 2901–2906 (1998).

[177] LightTrans VirtualLab, http://www.lighttrans.com.

[178] R. Weber, B. Neuenschwander, and H. P. Weber, “Thermal effects in solid-state laser materials,” Opt. Mater. **11**(2), 245–254 (1999).

[179] R. W. Dixon, “Photoelastic properties of selected materials and their relevance for applications to acoustic light modulators and scanners,” Appl. Phys. **38**(13), 5149–5153 (1967).

[180] W. R. Cook, D. F. Nelson, and K. Vedam, "High frequency properties of dielectric crystals: piezooptic and electrooptic constants," in *Landolt-Börnstein - Group III Condensed Matter Vol. III/30A*, D. F. Nelson, ed. (Springer, 1996).

[181] A. S. Andrushchak, Y. V. Bobitski, M. V. Kaidan, B. G. Mytsyk, A. V. Kityk, and W. Schranz, "Two-fold interferometric measurements of piezo-optic constants: application to β-BaB$_2$O$_4$ crystals," Opt. Laser Technol. **37**(4), 319–328 (2005).

[182] W. Koechner, "Absorbed pump power, thermal profile and stresses in a cw pumped Nd:YAG crystal," Appl. Opt. **9**(6), 1429–1434 (1970).

[183] Meta Numerics, http://www.meta-numerics.net.

[184] K. Yonezawa, Y. Kozawa, and S. Sato, "Generation of a radially polarized laser beam by use of the birefringence of a c-cut Nd:YVO$_4$ crystal," Opt. Lett. **31**(14), 2151–2153 (2006).

[185] D. Asoubar, M. Kuhn, and F. Wyrowski, "Acceleration of dominant transversal laser resonator eigenmode calculation by vector extrapolation methods," IEEE J. Quantum Electron. **51**(11), 1–10 (2015).

[186] P. A. Bélanger and C. Paré, "Optical resonators using graded-phase mirrors," Opt. Lett. **16**(14), 1057–1059 (1991).

List of Figures

List of Tables

Acknowledgment

First of all I would like to thank my supervisor Prof. Dr. Frank Wyrowski for his great encouragement and precious advice. I really enjoyed the fruitful and active discussions with him. Also I would like to express my considerable thanks to Dr. Michael Kuhn for the helpful mathematical discussions during our daily train trip. Great thanks also to Christian Hellmann, who supported my programming in VirtualLab. Further on I would like to thank my colleague Site Zhang for the scientific exchange and words of encouragement. In the same way I would like to thank my colleague Olga Baladron Zorita for revising the manuscript. Big thanks also to my office mate Dr. Hagen Schweitzer for his excellent advice and comments. Finally I would like to thank my family and Lena for their patience and leniency during the last three years including a lot of busy weekends.

This work was supported by LightTrans International UG and the Thuringian Ministry of Economy, Labor and Technology funded from the European Social Fund.

Ehrenwörtliche Erklärung des Verfassers

Ich erkläre hiermit ehrenwörtlich, dass ich die vorliegende Arbeit selbsständig und ohne unzulässige Hilfe Dritter und ohne Benutzung anderer als der angegebenen Hilfsmittel und Literatur angefertigt habe. Insbesondere habe ich hierfür keine entgeltliche oder unentgeltliche Hilfe von Vermittlungs- bzw. Beratungsdiensten (Promotionsberater oder andere Personen) in Anspruch genommen. Niemand hat von mir unmittelbar oder mittelbar geldwerte Leistungen für Arbeiten erhalten, die im Zusammenhang mit dem Inhalt der vorliegenden Dissertation stehen.

Bei der Erstellung der vorliegenden Dissertation haben mir die nachstehend aufgeführten Personen in der jeweils beschriebenen Weise unentgeltlich geholfen:

1. Herr Prof. Dr. Frank Wyrowski als Betreuer dieser Arbeit.
2. Mein Kollege Herr Site Zhang bei der Formulierung und numerischen Implementierung der in Kapitel 4.1 aufgeführten Algorithmen.
3. Meine Kollegin Frau Olga Baladron Zorita als Korrektorin hinsichtlich Rechtschreibung und Grammatik.

Weitere Personen waren an der inhaltlich-materiellen Erstellung der vorliegenden Arbeit nicht beteiligt. Ich habe für die Erstellung der Arbeit keine anderen als die angegebenen Hilfsmittel verwendet. Alle aus Quellen direkt oder indirekt übernommenen Daten und Konzepte sind unter Angabe der Quelle gekennzeichnet. In die vorliegende Arbeit wurden von mir bereits publizierte Ergebnisse mit eingearbeitet. Eine vollständige Liste dieser Publikationen befindet sich am Ende dieses Dokuments.

Die Arbeit wurde bisher weder im In- noch im Ausland in gleicher oder ähnlicher Form einer anderen Prüfungsbehörde vorgelegt.

Die an der Physikalisch-Astronomischen Fakultät geltende Promotionsordnung ist mir bekannt.

Ich versichere ehrenwörtlich, dass ich nach bestem Wissen die reine Wahrheit gesagt und nichts verschwiegen habe.

Jena, den ____________________

Daniel Christian Asoubar

Lebenslauf

Persönliche Angaben

Name: Daniel Christian Asoubar
Geburtsdaten: 31.10.1987 in Ochsenfurt (Lkr. Würzburg)

Berufserfahrung

Seit 11/2012

Doktorand und Technischer Support bei der LightTrans International UG, Jena. Tätigkeitsschwerpunkte sind:

- Entwicklung von Simulationskonzepten für Laserresonatoren
- Physikalisch- und geometrisch-optische Simulation und Optimierung von Kundensystemen auf den Gebieten: Laserresonatoren, Beugungsgitter, Ultrakurze Pulse, Diffraktive Optische Elemente und Lighting
- Fehleranalyse in Simulationsalgorithmen
- Kundenschulung und technischer Vertrieb

07/2011-10/2012

Wissenschaftlicher Mitarbeiter am Institut für Angewandte Physik (IAP) Jena in der Forschungsgruppe Optical Engineering von Prof. Dr. Frank Wyrowski. Tätigkeitsschwerpunkte waren:

- Modellierung und Design einfacher optischer Systeme
- Entwicklung einer Theorie zur parabasalen Zerlegung elektromagnetischer Felder
- Sampling und Numerik elektromagnetischer Felder

04/2012-06/2012	Gastwissenschaftler an der TU Delft (Niederlande) in der Forschungsgruppe Optica von Prof. Dr. Paul Urbach. Tätigkeitsschwerpunkt war: • Extended Nijboer-Zernike (ENZ) Beugungstheorie
04/2009-02/2011	Wissenschaftlicher Mitarbeiter am Fraunhofer Institut für Angewandte Optik und Feinmechanik (IOF) Jena in der Abteilung Optische Schichten von Prof. Dr. Norbert Kaiser.

Schulbildung, Wehrdienst und Akademischer Werdegang

Seit 10/2012	Studium Master of Arts: General Management an der Hochschule für Technik, Wirtschaft und Kultur (HTWK) Leipzig
10/2010-10/2012	Englischsprachiges Studium Master of Science: Photonics an der Friedrich-Schiller-Universität Jena Titel der Masterarbeit: Free-space propagation in field tracing
10/2007-08/2010	Studium Bachelor of Engineering: Laser- und Optotechnologien an der Fachhochschule Jena Titel der Bachelorarbeit: Replikation von plasmageätzten Antireflexstrukturen mittels Heiprägen
10/2006-06/2007	Wehrdienst in Veitshöchheim (Lkr. Würzburg)
06/2006	Fachgebundene Hochschulreife an der Fachoberschule Kitzingen

Jena, den ____________________

____
Daniel Christian Asoubar

Liste eigener Veröffentlichungen

Peer-Review Artikel

1. Daniel Asoubar, Site Zhang, Frank Wyrowski, and Michael Kuhn, “Parabasal field decomposition and its application to non-paraxial propagation,” Opt. Exp. **20**(21), 23502–23517 (2012).
2. Daniel Asoubar, Site Zhang, Frank Wyrowski, and Michael Kuhn, “Efficient semi-analytical propagation techniques for electromagnetic fields,” J. Opt. Soc. Am. A **31**(3), 591–602 (2014).
3. Site Zhang, Daniel Asoubar, Robert Kammel, Stefan Nolte, and Frank Wyrowski, “Analysis of pulse front tilt in simultaneous spatial and temporal focusing,” J. Opt. Soc. Am. A **31**(11), 2437–2446 (2014).
4. Daniel Asoubar, Site Zhang, Frank Wyrowski, and Michael Kuhn, “Laser resonator modeling by field tracing: a flexible approach for fully vectorial transversal eigenmode calculation, J. Opt. Soc. Am. B **31**(11), 2565–2573 (2014).
5. Daniel Asoubar, Site Zhang, and Frank Wyrowski, “Simulation of birefringence effects on the dominant transversal laser resonator mode caused by anisotropic crystals,” Opt. Exp. **23**(11), 13848–13865 (2015).
6. Daniel Asoubar and Frank Wyrowski, “Fully vectorial laser resonator modeling of continuous-wave solid-state lasers including rate equations, thermal lensing and stress-induced birefringence,” Opt. Exp. **25**(15), 18802–18822 (2015).
7. Daniel Asoubar, Michael Kuhn, and Frank Wyrowski, “Acceleration of dominant transversal laser resonator eigenmode calculation by vector extrapolation methods,” IEEE J. Quantum Electron. **51**(11), 1–10 (2015).
8. Site Zhang, Daniel Asoubar, Christian Hellmann, and Frank Wyrowski “Propagation of electromagnetic fields between non-parallel planes: a fully vectorial formulation and an efficient implementation,” Appl. Opt. (to be published, in peer-review process).

Konferenzbeiträge

1. D. Asoubar, S. Zhang, F. Wyrowski, and M. Kuhn, “Propagation of nonparaxial fields by parabasal field decomposition,” Proc. of SPIE Vol. 8429, 84290I (2012).
2. S. Zhang, D. Asoubar, F. Wyrowski, and M. Kuhn, “Efficient and rigorous propagation of harmonic fields through plane interfaces,” Proc. of SPIE Vol. 8429, 84290J (2012).
3. D. Asoubar, S. Zhang, F. Wyrowski, and M. Kuhn, “Parabasal field decomposition and its application to non-paraxial propagation,” Proc. of DGAO, (2012).
4. S. Zhang, D. Asoubar, F. Wyrowski, and M. Kuhn, “Tilt operator for harmonic fields and its applications to propagation through plane interfaces,” Proc. of DGAO, (2012).
5. S. Zhang, H. Zhong, D. Asoubar, F. Wyrowski, and M. Kuhn, “Tilt operator for electromagnetic fields and its application to propagation through plane interfaces,” Proc. of SPIE Vol. 8550, 85503I (2013).
6. D. Asoubar, S. Zhang, F. Wyrowski, and M. Kuhn, “Semi-analytical techniques for efficient electromagnetic field propagation,” Proc. of SPIE Vol. 8550, 85503F (2013).
7. D. Asoubar, F. Wyrowski, H. Schweitzer, C. Hellmann, and M. Kuhn, “Resonator modeling by field tracing: a flexible approach for fully vectorial laser resonator modeling,” Proc. of SPIE Vol. 9135, 91350B (2014).
8. D. Asoubar, M. Kuhn, and F. Wyrowski, “Fully vectorial laser resonator modeling by vector extrapolation methods,” Proc. of SPIE Vol. 9342, 934214 (2015).
9. S. Zhang, D. Asoubar, F. Wyrowski, “Rigorous modeling of laser light propagation through uniaxial and biaxial crystals,” Proc. of SPIE Vol. 9346, 93460N (2015).
10. D. Asoubar, C. Hellmann, H. Schweitzer, M. Kuhn, and F. Wyrowski, “Customized homogenization and shaping of LED light by micro cells arrays,” Proc. of SPIE Vol. 9383, 93831B (2015).
11. D. Asoubar, S. Zhang, and F. Wyrowski, “Fully vectorial simulation of Laser resonators including anisotropic media,” Proc. of DGAO, (2015).
12. D. Asoubar, H. Schweitzer, C. Hellmann, M. Kuhn, and F. Wyrowski “Fully-vectorial simulation and tolerancing of optical systems for wafer inspection by field tracing,” Proc. of SPIE Vol. 9526, 95260J (2015).

13. D. Asoubar, C. Hellmann, and F. Wyrowski “Flexible analysis of solid-state laser resonators including nonlinear gain saturation, thermal lensing, and stress-induced birefringence effects,” Invited Talk at SPIE Optical Systems Design Symposium, September 2015, Jena.
14. D. Asoubar, H. Schweitzer, M. Kuhn, C. Hellmann, and F. Wyrowski “Design of deterministic diffusers for head-up-display applications,” Talk at SPIE Optical Systems Design Symposium, September 2015, Jena.